

# Modeling of a natural circulation flow reactor for methanol synthesis from renewable sources

Description of an experimental prototype

by

**Guillermo Enrique Gutierrez-Neri**

in partial fulfillment of the requirements for the degree of

**Master of Science**

in Mechanical Engineering

at the Delft University of Technology,

to be defended publicly on Thursday August 30, 2018 at 10:00 AM.

Student number: 4626168  
Project duration: January 1, 2018 – August 30, 2018  
Supervisor: Ir. J. van Kranendonk, ZEF BV  
Thesis committee: Prof. dr. ir. W. de Jong, TU Delft (chair)  
Dr. ir. M. J. B. M. Pourquie, TU Delft  
Prof. dr. D. J. E. M. Roekaerts, TU Delft

*This thesis is confidential and cannot be made public until December 31, 2019.*

# Abstract

In 2015, 30% of the world's energy demand was met through petroleum based sources, whose burning has affected the world's climate. The Paris Climate Agreement, among other policies, has shifted the focus towards usage of renewable energy sources. Currently, the renewable market caters predominantly to meeting the electric demand, which only represents 19% of the world's energy consumption. Zero Emission Fuels (ZEF) aims to create a small-scale chemical plant that uses renewable energy sources to create synthetic methanol. This follows the vision of adapting renewable energy sources for non-electric usage. Methanol is the simplest liquid hydrocarbon at atmospheric condition; it can be used as a fuel or as a base chemical for other products. Presently, the industry reforms syngas obtained from fossil fuels to create methanol, predominantly using large-scale catalytic reactors. For production of methanol from renewable sources, Bos and Brillman developed a small-scale catalytic reactor driven by natural circulation. ZEF adapted the Brillman reactor for their chemical plant, creating a prototype of the modified Brillman reactor (MBR). The present work aims to create a model that describes the steady-state methanol production of the prototype using computational fluid dynamics (CFD) and chemical process models.

The MBR is an innovative design based on a closed loop geometry. The gases are driven by buoyant forces from a temperature difference between the high-temperature catalytic reaction zone and the low-temperature condensation zone. Heat recovery elements are used to exchange heat between the hot and cold streams as they travel in the loop. The CFD model developed on Fluent™ 18.2, uses a RNG  $\kappa$ - $\epsilon$  turbulent model, with multicomponent species transport, convective heat transfer and momentum loss effects from the catalytic zone. The boundary conditions are based on the operating conditions of the prototype. The model calculates flow-rate, and the effect of heat recovery elements inside the natural circulation loop. A chemical process model developed in COCO™ 3.2 is used to calculate a mass and energy balance for the two-phase behavior of the gas mixture inside the MBR.

A study of the effects of a natural circulation loop with a configuration similar to the reactor is performed, observing potential benefits by tilting the system. The combination of effects due to heat recovery and flow blockage in the reactor is studied, and the results are evaluated with experimental measurements. The chemical process model developed closely resembles the experimental characterization of the reactor. The parameters of flow-rate and internal temperatures can not be validated due to limited data available from experimental procedures.

---

# Acknowledgement

To my parents and siblings for raising me to be a hardworking man. Having never being told that I could not do anything is magical; it creates a frame of mind that makes endlessly trying and failing appealing. This research is a clear example of such mindset.

To the few friends at home and the new found friends in this foreign land that have helped me become a wholesome person.

To my girlfriend, who has kept me sane for the duration of my research and has not grown tired of my excessive use of commas.

To the National Science and Technology Council of Mexico (CONACYT) and the National Secretary of Energy (SENER) that have provided me with the financial support to take a mechanical engineering bachelor from a no-name college (much love to my Gatos Negros) into one of the highest ranking universities in the world.

To my boss and supervisors, for steering me into a cohesive research project. I would not have done the kind of work I performed without your guidance.

I owe you all my deepest gratitude.

And to you, the poor soul about to read my work. I hope you find this report useful.

Regards, Guillermo Enrique Gutiérrez Neri

*“Don’t forget. You’re here forever.”*

---

# Contents

<b>1</b>	<b>Introduction</b>	<b>1</b>
1.1	Zero emission fuels . . . . .	2
1.2	Research questions . . . . .	3
1.3	Thesis structure . . . . .	3
1.4	Goal . . . . .	3
<b>2</b>	<b>Theory</b>	<b>5</b>
2.1	Methanol synthesis from renewable sources . . . . .	5
2.1.1	Industrial processes for methanol synthesis . . . . .	5
2.1.2	Catalyst for methanol synthesis . . . . .	10
2.1.3	Reaction kinetics . . . . .	11
2.2	Condensation . . . . .	19
2.2.1	Single stage flash . . . . .	19
2.2.2	Condensation of reaction products . . . . .	20
2.3	Flow in natural circulation loops . . . . .	22
2.3.1	Generalized correlation for single-phase flow . . . . .	23
2.3.2	Stability of the flow . . . . .	26
2.4	CFD modeling . . . . .	28
2.4.1	Fluid properties . . . . .	29
2.4.2	Heat transfer coefficients . . . . .	30
2.4.3	Chemical reactions . . . . .	32
2.4.4	Interpreting results from simulations . . . . .	34
<b>3</b>	<b>Model setup</b>	<b>35</b>
3.1	Model overview . . . . .	35
3.2	Sources of uncertainty . . . . .	37
3.2.1	Case a) . . . . .	37
3.2.2	Case b), c) and d) . . . . .	39
3.2.3	Case b) and d) . . . . .	40
3.2.4	Case e) . . . . .	43

---

<b>4</b>	<b>Modeling results and discussion</b>	<b>45</b>
4.1	Tilting of uniform diameter loop . . . . .	45
4.1.1	Geometry and Mesh . . . . .	45
4.1.2	Boundary conditions . . . . .	45
4.1.3	Results . . . . .	46
4.1.4	Observations . . . . .	48
4.2	Simulations of gas flow and temperature in SMBR . . . . .	50
4.2.1	Geometry and Mesh . . . . .	50
4.2.2	Boundary conditions . . . . .	51
4.2.3	Results . . . . .	52
4.2.4	Observations . . . . .	53
4.3	SMBR chemical process model . . . . .	56
4.3.1	Boundary conditions . . . . .	56
4.3.2	Results . . . . .	57
4.3.3	Observations . . . . .	58
4.4	Simulation of SMBR with mixed gas composition . . . . .	60
4.4.1	Boundary conditions . . . . .	60
4.4.2	Results . . . . .	60
4.5	Implementation of Bussche and Froment GKM into Fluent . . . . .	62
4.5.1	Boundary conditions . . . . .	62
4.5.2	Results . . . . .	63
4.5.3	Observations . . . . .	64
4.6	Summary of results . . . . .	65
4.7	Improving reactor operation . . . . .	66
4.7.1	Reducing energy losses . . . . .	66
4.7.2	Increasing methanol production rate . . . . .	66
<b>5</b>	<b>Conclusions and recommendations</b>	<b>69</b>
5.1	Concluding remarks . . . . .	69
5.2	Recommendations . . . . .	70
	<b>Bibliography</b>	<b>71</b>
	<b>Appendices</b>	<b>75</b>
<b>A</b>	<b>Fluid properties</b>	<b>77</b>
A.1	Basic model . . . . .	77
A.2	Detailed model . . . . .	78

---

---

<b>B Data</b>	<b>81</b>
B.1 Tilting UDL . . . . .	81
B.1.1 Simulation settings . . . . .	81
B.1.2 Results . . . . .	83
B.1.3 Heat transfer coefficients . . . . .	85
<b>C Fluent™ implementation of reactions</b>	<b>87</b>
C.1 Methanol synthesis reactor . . . . .	90
C.1.1 Replicating Bussche and Froment model . . . . .	91
C.1.2 Replicating industrial reactor . . . . .	94
C.2 Natural circulation methanol synthesis reactor . . . . .	96
C.2.1 Simulation of SMBR as a batch process reactor . . . . .	96
<b>D Steady state nitrogen flow-rate for MBR with heat recovery</b>	<b>101</b>





# Nomenclature

## Abbreviations

CPM	Chemical process model
FP	Fluid properties
GKM	Global kinetic model
MBR	Modified Brilman reactor
MEOH	CO <sub>2</sub> hydrogenation reaction
MKM	Micro-kinetic model
NCL	Natural circulation loop
RWGS	Reverse water gas shift reaction
SMBR	Small modified Brilman reactor
UDL	Uniform diameter loop

## Symbol list

$A$	Area	[m <sup>2</sup> ]
$c_p$	Specific heat	[J kg <sup>-1</sup> K <sup>-1</sup> ]
$D$	Diameter	[m]
$f$	Fugacity	[Pa]
$G$	Superficial mass velocity	[kg s <sup>-1</sup> m <sup>-2</sup> ]
$H$	Enthalpy	
$K$	Equilibrium constant	
$k$	Reaction rate constant	
$L_t$	Total length of loop	[m]
$P$	Perimeter	[m]
$p$	Partial pressure of species	[bar]
$Q$	Heat transfer rate	[W]
$q$	Heat flux	[W m <sup>-2</sup> ]
$r$	Rate of reaction	[mol kg <sub>cat</sub> <sup>-1</sup> s <sup>-1</sup> ]
$S$	Volumetric source	
$U$	Heat transfer coefficient	[W m <sup>-2</sup> K <sup>-1</sup> ]
$u$	Velocity	[m s <sup>-1</sup> ]

$V$	Volume	[m <sup>-3</sup> ]
$W$	Mass flow	[kg s <sup>-1</sup> ]
$x$	Liquid mole fraction of mixture	
$y$	Vapor mole fraction of mixture	
$z$	Feed mole fraction	

## Greek symbols

$\beta$	Thermal expansion coefficient	[K <sup>-1</sup> ]
$\gamma$	Grouped parameters for global reaction	
$\lambda$	Heat conductivity	[W m K]
$\mu$	Dynamic viscosity	[Pa s]
$\omega$	Mass fraction	[kg/kg]
$\phi$	Molar flow rate	
$\rho$	Density	[kg m <sup>-3</sup> ]
$\theta$	Surface coverage parameter	
$\varphi$	Tilting angle (default = 90°)	

## Subscripts

$a$	Adsorption equilibrium
$c$	Cooling
$cat$	Catalyst
$e$	Reaction equilibrium
$eq$	Equilibrium composition
$F$	Feed
$f$	Flash (vapor-liquid equilibrium)
$h$	Heating
$i$	Index (species or reaction)
$j$	Index (iterative)
$m$	Modified
$o$	Average / Reference
$p$	Particle
$r$	Reaction
$ss$	Steady state

## Superscripts

$L$	Liquid phase
$V$	Vapor phase



# Chapter 1

## Introduction

The rise of human technology has led us to a better quality of life, beyond any of our ancestors had ever hoped to achieve. Since the 1700s this technology has been powered by burning fossil fuels. These are energy dense hydrocarbons, most of them liquid at ambient conditions, which make them easy to transport and use.

For more than a century, civilization has primarily employed finite fossil energy sources. Their combustion releases gases that pollute our cities and has been found to change our climate through the large emittance of greenhouses into the atmosphere. It is unquestionable that human activity attributed to the increase of the concentration of carbon dioxide in the atmosphere. The trend can only be reversed by changing our culture of energy consumption.

There is some hope at the horizon in the form of global policy. The Paris Climate Agreement is an unprecedented commitment between 180 nations in the world. The ultimate goal is to keep the world's temperature no higher than 1.5°C above pre-industrial levels, as it has been deemed by climate scientists to be the *tipping point* for the stability of the climate of the current world [1].

The world and its industries are about to face massive changes for the next 30 years. The first developments are already underway with the integration of renewable electricity from hydropower, PV solar panels and wind turbines. As of 2015, only 19% of the world's energy consumption is electric [2]. When the changes in our energy usage take place, two cases are likely to occur: an ideal and a conservative scenarios.

- ◇ The ideal scenario is where renewable sources are used to implement massive electrification in the energy market. However, most of these energy sources are fluctuating and their largest pools are often located far away from human population centers. New methods for **energy storage and distribution** that can match the convenience of current hydrocarbons will be developed. Currently, few reliable options exist for long-term seasonal storage of renewables [2].
- ◇ A conservative scenario is where the 30 year window is too small and restrictive for many markets to adapt to. Industries such as aviation, long distance shipping and chemical production are not likely to change their material or energy sources away from fossil fuels. It is fair to say that even after the implementation of renewables, there will still be a need for **combustible energy carriers**, such as hydrocarbons from fossil fuels.

Could it be possible to use renewable power sources to synthesize hydrocarbons? It is indeed possible to make them with current industrial-sized technology. However, it is not yet economically feasible without large subsidies. This makes the prospect economically uncompetitive. It is unreasonable for the world to pay more than €1000 for a barrel of synthetic fuel, when oil companies can offer a barrel of petrol for less than €100.

## 1.1 Zero emission fuels

ZEF B.V. is a technological start-up working in the 3mE Process and Energy Lab at TU Delft since 2017. So far more than 30 students have worked there from various tech schools in the Netherlands and faculties from the university, aspiring to create a small chemical plant that can make synthetic methanol by capturing  $\text{CO}_2$  from the air, using a solar PV panel as energy source. A process diagram representing the installation of the plant is presented in Fig. 1.1.

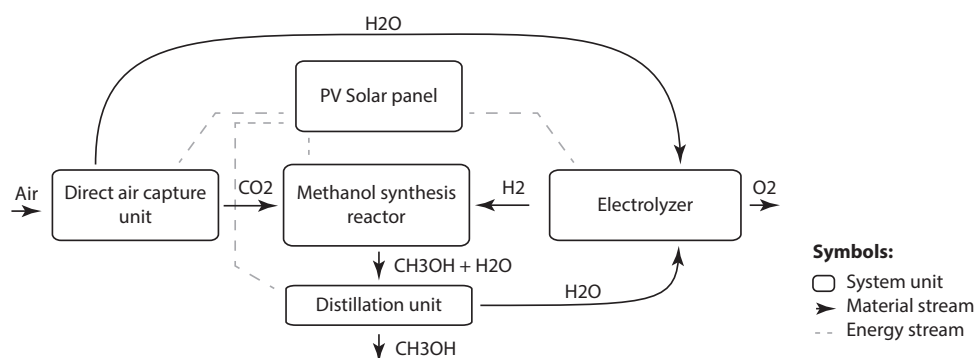


Fig. 1.1. ZEF chemical plant process diagram

With a small chemical plant, increasing production is achieved by **increasing the number of plants**, as opposed to increasing the size of the equipment, which has been the standard from the old chemical industry. The goal is to have a field of solar panels each fitted with a ZEF chemical plant, as shown in Fig. 1.2.

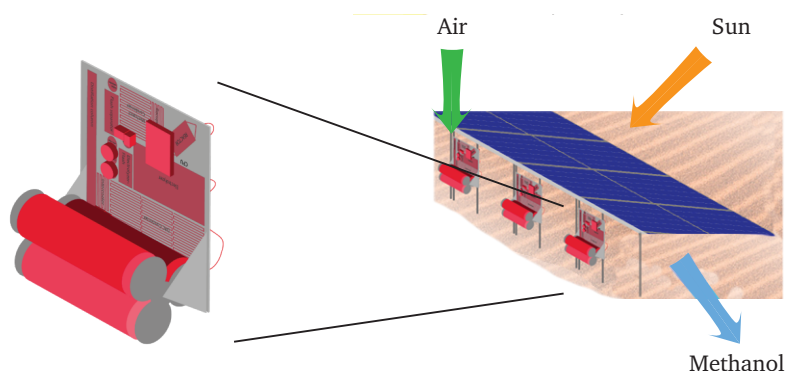


Fig. 1.2. ZEF chemical plant installation concept.

Because of the limited energy and the constant fluctuations that PV solar energy provides, diverse knowledge in engineering is necessary to create the chemical processes required to capture the carbon dioxide and synthesize it into a liquid fuel. One of the components of the chemical plant is the methanol synthesis reactor. Low energy consumption in the reactor is desired to have a functional chemical plant.

The novel reactor proposed uses natural convection as a driving force, with heat recovery elements and in-situ separation. It is a functional, but complex system. Experimental testing and computer simulations are essential to understand its performance and flaws in order to improve the design.

## 1.2 Research questions

There are several phenomena that occur inside ZEF's reactor, such as the buoyancy driven circulating flow, heat recovery, catalytic methanol synthesis reactions and mixture separation through condensation.

This work will shine a light on select individual phenomena and how their behavior links to one another. To do so, the following questions will be addressed:

- ◇ What is the flow-rate on the reactor as a natural circulation loop?
- ◇ What are the effects of heat recovery and the packed bed in the loop?
- ◇ Can a methanol synthesis reaction model be implemented into CFD simulations?
- ◇ Can a model be created to describe the experimental work by [Basarkar](#)?

## 1.3 Thesis structure

To answer the research questions, this research presents a review of the theory behind each phenomenon in Chapter 2, covering the topics of:

- ◇ State of the art on current practices and modeling of catalytic methanol synthesis processes.
- ◇ Condensation of the multi-component mixture inside the reactor.
- ◇ Relating thermally convective driving forces and flow-rate within a closed loop.
- ◇ An overview of the implementation of these phenomena into the commercial CFD software package Fluent™ 18.2 and COCO™ simulator.

Chapter 3 will create a link between the modeling theory, the experimental set-points used as boundary conditions and the simulations performed. This chapter presents an overview of the cases analyzed and their possible sources of error.

In Chapter 4, results for CFD and chemical process models are reported. Validation is obtained by comparing with similar systems reported in literature and experimental measurements done on the prototype by [Basarkar \(2018\)](#). The most relevant observations are extracted and discussed at the end of the chapter. Paths of improvement on the natural circulation reactor operation are also examined.

## 1.4 Goal

This research aims to:

- ◇ Create a set of models that can describe the steady-state methanol production of the natural circulation reactor, in collaboration with the experimental characterization of [Basarkar](#).
- ◇ Identify the coupled effects of the catalyst packing, flow rate from natural circulation to methanol conversion. This will give ZEF BV a guideline of how to improve the performance of the reactor.



# Chapter 2

## Theory

### 2.1 Methanol synthesis from renewable sources

Methanol is an important chemical compound. Most of its current applications in the industries are as a solvent or base material for organic chemicals. With new regulations expected to come as a consequence of the Paris Climate Agreement, a shift in the energy markets is inevitable. Methanol is a stable liquid under atmospheric conditions with an energy density of 22.4 MJ/kg (gasoline has 46.7 MJ/kg) and can be directly used in gasoline combustion engines. It has the potential to be a relevant **dense energy carrier** for industries in the near future [4].

To produce methanol it is necessary to have a source of hydrogen and a source of carbon. Current processes use natural gas through steam reforming and/or catalytic conversion to create synthesis gas (syngas). It is a mixture of CO<sub>2</sub>, CO and H<sub>2</sub> that is used as a feedstock into methanol reactors. A genuine zero emission methanol production system will need to have a source for the feedstock that is **independent from fossil fuels**. ZEF B.V. acquires both hydrogen and carbon from the water and carbon dioxide that are already present in the atmosphere, though at very minute concentrations (>12000 and 400 ppm, respectively).

It goes without saying that the energy sources which drive the operation of the reactor should also be renewable. This poses further challenges to the reactor operation, namely having a limited energy input with fluctuating loads. It creates the need for a reactor that is both energy efficient and of agile operation. Depending on the availability of the energy source, production can wind up or down. These are **atypical design constrains** for the current chemical industry.

#### 2.1.1 Industrial processes for methanol synthesis

The most common route from syngas to methanol is using copper-zinc based catalysts in chemical reactors, operating in temperature ranges of 200 to 300°C and pressures between 50 to 200 bar. A large number of the installed reactors are **isothermal reactors**. These maintain an almost constant temperature profile using external cooling systems. The uniform temperature profile helps the catalyst achieve a long operation life. Thermal energy can also be recovered from the reactor by using coolant liquids, such as steam. A process diagram of such installation is presented in Fig. 2.1.

The most relevant reactions for methanol synthesis are presented in Eqs. 2.1-2.3. The exothermic nature of the reactions is a problem for the production of methanol, as the increase of temperature **shifts the reaction equilibrium away from methanol**, in favor of higher CO concentration. This is discussed in greater detail in Sec. 2.1.3.3.



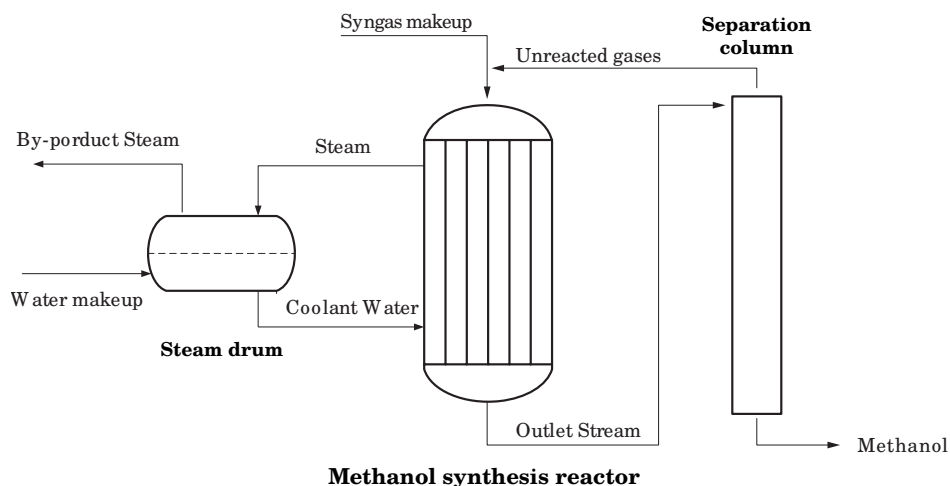


Fig. 2.1. Process diagram of isothermal methanol synthesis reactor installation cooled by (boiling) water [5].



From the stoichiometry of reactions in Eqs. 2.1 and 2.3, a stoichiometric number  $SN$  for the feed composition is derived in Eq. 2.4. For methanol synthesis, the ideal value for  $SN$  should be slightly above 2, as reported by Bozzano and Manenti (2016).

$$SN = \frac{[\text{H}_2] - [\text{CO}_2]}{[\text{CO}] + [\text{CO}_2]} \quad (2.4)$$

In practice, the production of methanol is sensitive to the composition of the feed gas. It can be seen in Fig. 2.2 that the yield of methanol<sup>i</sup> from a feed consisting of only  $\text{H}_2$  and  $\text{CO}_2$  is much smaller than with a feed mixture of  $\text{H}_2/\text{CO}/\text{CO}_2$ . In practice, this means that a **larger recycling of unreacted components** is necessary to achieve higher carbon conversion from  $\text{CO}_2$  into  $\text{CH}_3\text{OH}$ .

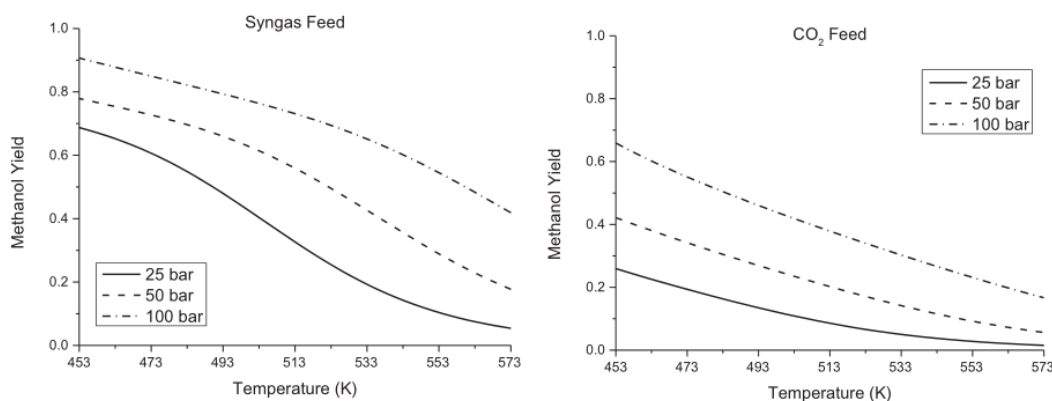


Fig. 2.2. Chemical equilibria in MS from syngas and from a feed with different amount of CO in the feed. a) Feed of  $\text{H}_2/\text{CO}/\text{CO}_2$ : 75.9/16.9/7.2 b) Feed of  $\text{H}_2/\text{CO}/\text{CO}_2$ : 75.0/0.0/0.25.

<sup>i</sup>Methanol yield<sup>i</sup> is defined here as the ratio of methanol to carbon carrying molecules in the equilibrium composition: Yield =  $[\text{CH}_3\text{OH}] / [\text{CO}_2 + \text{CO}]$  [7]

Increasing the operating pressure and/or using a combined feed of CO and CO<sub>2</sub> can shift the equilibrium favorably towards methanol; both options have their own nuances. Raising the pressure will increase operation and maintenance cost of the equipment, not just for the reactor but also ZEF's chemical plant. Creating CO from the captured CO<sub>2</sub> is an inefficient process with current state-of-the-art equipment [8]. This makes the approach of using the feed of H<sub>2</sub> and CO<sub>2</sub> at a ratio of 0.75/0.25 (from Eq. 2.4), the most viable one for methanol production from renewable sources [7].

### 2.1.1.1 Brillman reactor

In 2015, [Bos and Brillman](#) presented an alternative to the conventional catalytic methanol synthesis reactor. It integrates a separation system into the reactor by condensing products (water and methanol) in situ, thus ensuring that **unreacted components remain in the gas phase** and will not be able to leave the reactor. It operates with a feed of H<sub>2</sub>/CO<sub>2</sub> at a ratio of 0.75/0.25.

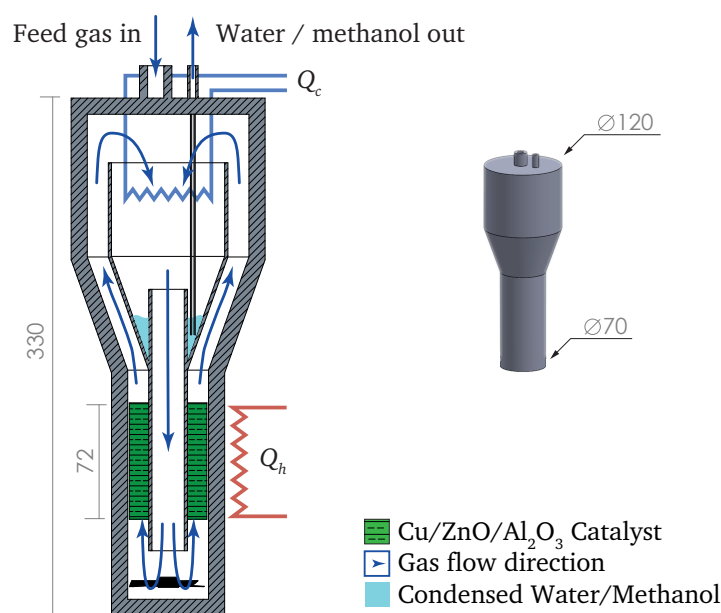


**Fig. 2.3.** Cross-section of the Brillman reactor. Cooling  $Q_c$  achieved from water passing through a copper spiral inside the reactor. Heating  $Q_h$  achieved from an electrical resistance jacket surrounding the catalyst zone (green). Units: mm. Approximate dimensions [7].

Fig. 2.3 presents a cross-section of the Brillman reactor. A fan and heater are placed at the bottom of the system to drive a gas stream upwards to pass through the catalyst zone on the outer perimeter. At the top-center of the reactor there is a water based cooling system that condenses the reacted products into a liquid trap, leaving the unreacted gases to circulate back into the bottom.

Finding a functional operating pressure for the reactor was based on getting the **reaction temperature higher than the condensation temperature**. This is necessary to ensure buoyant driving forces in the reactor. It is determined from phase equilibria calculations<sup>ii</sup> that at pressures higher than 100 bar with low reaction temperatures (473 K), the condensation temperature of the product mixture can happen at the same temperature of the reaction<sup>iii</sup>. At lower pressures (50 bar) the reaction temperature would be higher than the dew temperature of the product mixture (413-403 K), thus ensuring a thermal driving force that could provide a driving force for the fluid<sup>iv</sup>.

<sup>ii</sup>Chemical equilibria are discussed in Sec. 2.1.3.3

<sup>iii</sup>Condensation of multicomponent mixture is discussed in Sec. 2.2

<sup>iv</sup>Buoyant driving forces are discussed in Sec. 2.3.

Despite the reactor being fitted with an electric fan, **Bos and Brilman** determined from their experiments that the **improvements on the productivity were limited to small fan speeds**. This is attributed to the gas passing through the catalyst zone at a flow rate higher than it could transfer heat to. Essentially, the gases were coming in contact with the catalyst at temperatures lower than the optimal reaction temperature.

This natural circulation catalytic reactor has its performance measured in terms of:

- ◇ Productivity of methanol per gram of catalyst per unit time. Units of  $\text{mol}_{\text{CH}_3\text{OH}} \text{g}_{\text{cat}}^{-1} \cdot \text{hr}^{-1}$
- ◇ The specific energy demand of thermal energy  $Q_h$  in MJ per kg of methanol converted.

At peak productivity, the reactor by **Bos and Brilman** reports an output of  $7.8 \text{ mol} \cdot \text{kg}_{\text{cat}}^{-1} \cdot \text{hr}^{-1}$  with a specific energy demand of  $70 \text{ MJ} \cdot \text{kg}_{\text{CH}_3\text{OH}}^{-1}$  [7]. With the fan disabled, the productivity and specific energy demand of Brilman's reactor are  $6.4 \text{ mol} \cdot \text{kg}_{\text{cat}}^{-1} \cdot \text{hr}^{-1}$  and  $74 \text{ MJ} \cdot \text{kg}_{\text{CH}_3\text{OH}}^{-1}$ , respectively. The difference with the peak performance is comparatively small, which hints at the possibility of **designing a reactor driven only by natural convection**. For reference, an industrial (Lurgi) isothermal reactor with additional external stream recycling and cooling systems can produce  $19.39 \text{ mol} \cdot \text{kg}_{\text{cat}}^{-1} \cdot \text{hr}^{-1}$  [9].

### 2.1.1.2 ZEF's modified Brilman reactor

ZEF took Brilman's concept of a low energy demand reactor and re-designed it to the particular size and production constrains of approximately  $100 \text{ g}_{\text{CH}_3\text{OH}}/\text{day}$ . It also addresses the original's shortcomings in thermal energy efficiency by having elements specifically made to recover heat. The MBR design is showcased in Fig. 2.4b.

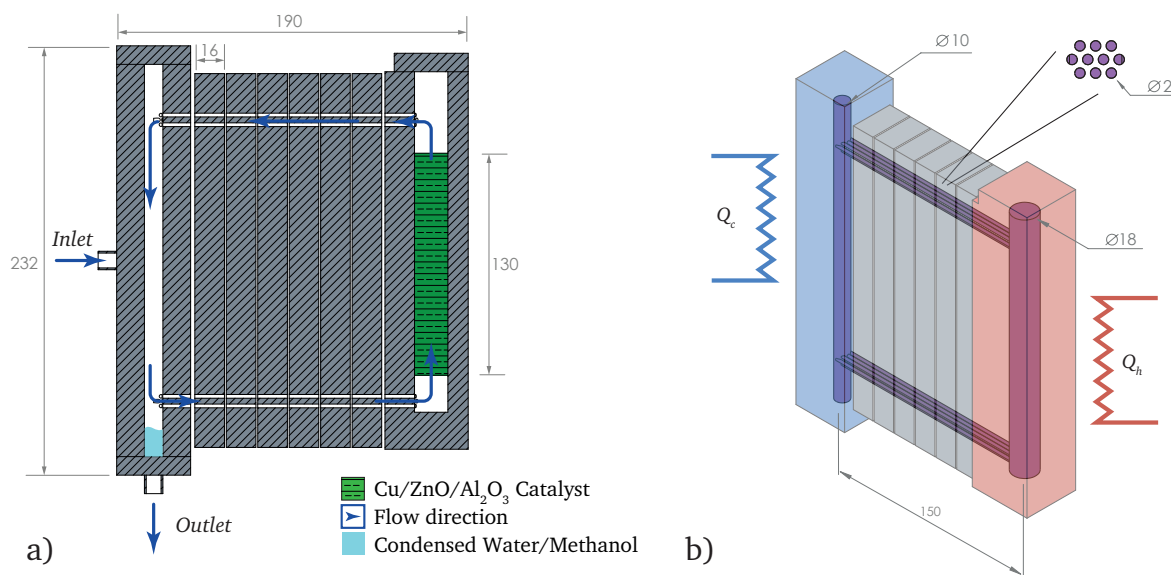


**Fig. 2.4.** Overview of MBR a) Cross-section of reactor body. Units: mm. b) Color-coded view of reactor sections. Fluid domain: purple, reactor: red, condenser: blue, heat recovery blocs: gray.

The heating is provided by an electrical resistance jacket placed on the outside walls of the reactor section block. The condenser block is cooled by free convection from ambient temperature air.

## 2.1.1.3 ZEF's small MBR

Problems arose during the experimental characterization of the MBR (reviewed in Sec. 4.2), which required the development of an **alternate design** of the methanol synthesis reactor.

The small MBR (SMBR) is showcased in Fig. 2.5. Both the reactor and condensing zones remain untouched, but the shape of the heat recovery blocks and the horizontal flow channels has been modified. It now uses three heat recovery blocks, and the multiple horizontal channel design has been replaced with a single 6.5 mm channel.

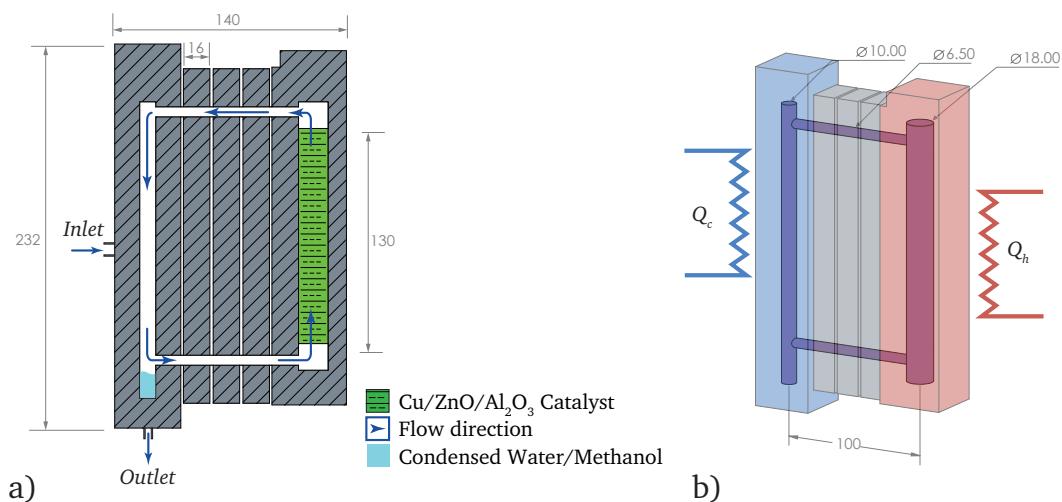


**Fig. 2.5.** Overview of SMBR. a) Cross-section of reactor body. Units: mm. b) Color-coded view of reactor sections. Fluid domain: purple, reactor: red, condenser: blue, heat recovery blocs: gray.

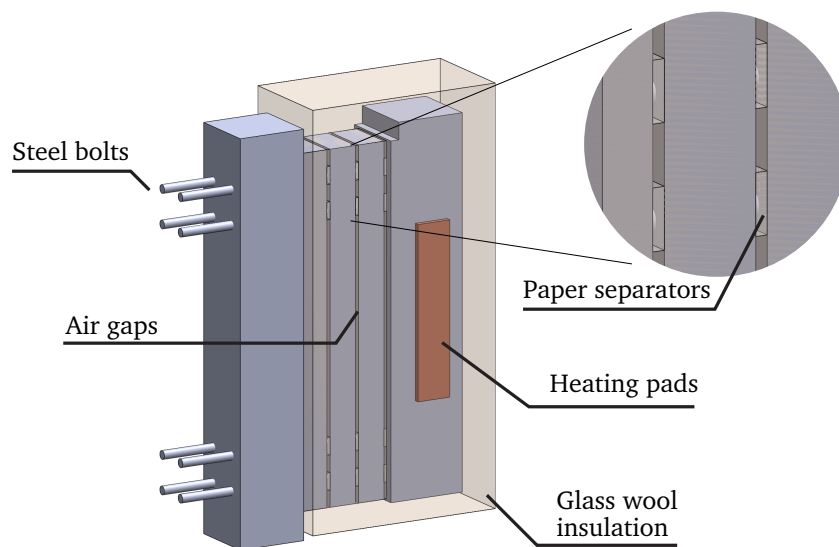


**Fig. 2.6.** Render of installation of SMBR.

Time constraints in experimental testing lead to not replicating flow-rate experiments concerning the SMBR geometry that were made for the MBR geometry. Only SMBR geometry has been used to model the reactor, while the MBR was used for an experimental flow validation presented in Appendix D.

### 2.1.2 Catalyst for methanol synthesis

Catalysts are essential materials for the industrial production of chemical compounds. These are a media on which surface compounds can adsorb and react to form new species that later get released from the outer layers. Under ideal conditions, the catalyst material is not depleted in the process.

Active sites are available on the surface of the catalyst. These are points where intermediate chemical bonds can be formed with the gas molecules surrounding it. In Fig. 2.7 shows a simple example of how molecules are adsorbed and their composition split on the active site of a solid catalyst to form new species.



Fig. 2.7. Example process steps in catalytic reactions through adsorption with a single active site. a) Binding of molecules into surface layers. b) Splitting of molecules on the surface. c) Formation of new compounds. d) New formed species have weak bondings with the surface and are released leaving the catalyst “intact”.

To characterize the behavior of catalysts, experiments are performed under specific conditions (pressure, temperature and feed composition). Models are developed which determine their influence on the catalyst’s performance.

#### 2.1.2.1 Catalysts for methanol synthesis

Before the 1920s, methanol was produced by distilling wood [10]. It all changed with the development of ZnO/CrO catalysts. These made it possible to produce methanol from syngas (derived from coal), operating at 250-300 bar and 300-450°C [11]. By 1950s the syngas feed was derived from natural gas, increasing its purity; the sulfur and chlorine byproducts that damaged the catalysts were now not present. This contributed to the development of new catalysts which could operate at lower pressures and temperatures, reducing the equipment cost.

In 1966 ICI pioneered a production method for copper based catalysts; a mixture of copper oxide with zinc oxide and alumina for thermal stability. It quickly became the standard to convert syngas into methanol [10]. Currently, most commercial industrial catalysts for low temperature methanol synthesis are still copper based composites [11].

The current research uses commercial cylindrical catalyst pellets composed of CuO/ZnO/Al<sub>2</sub>O<sub>3</sub> at an undisclosed ratio by RIOGEN™. These pellets are selected due to extensive industrial applications and reaction models available for this catalyst in literature [7, 9, 12].

#### 2.1.2.2 Catalyst packed bed

The commercial catalyst that is used has the form of porous cylindrical pellets of 5mm diameter and 5mm in length. These pellets fill the tubular portion of the vertical reactor section (Fig. 2.4). A low gas velocity is expected in the bed, with no solid particle motion. This interaction of the fluid passing through this section is assumed to be similar to that of a packed bed.

From a fluid mechanical perspective, the packed bed will generate a pressure drop across the length of the bed. Estimating this value based on the characteristics of the packing is essential to determine the flow-rate. If the flow regime of the unblocked stream is within the range of  $0 \leq Re \leq 3000$  [13]. The pressure drop along the bed can be determined with Ergun’s equation, presented in Eq. 2.5.

$$\frac{\Delta p}{L_{\text{bed}}} = \frac{150\mu}{\psi^2 D_p^2} \frac{(1-\varepsilon)^2}{\varepsilon^3} u_\infty + \frac{1.75\rho}{\psi D_p} \frac{(1-\varepsilon)}{\varepsilon^3} u_\infty^2 \quad (2.5)$$

Where:

$\mu$  is the fluid viscosity in Pa·s.

$\rho$  is the fluid density in kg/m<sup>3</sup>.

$D_p$  is the mean particle diameter in m.

$\psi$  is the correction factor for particle sphericity as a function of the particle volume  $V_p$ , mean diameter  $D_p$  and surface area  $A_p$ , determined for the pellets in Eq. 2.6<sup>v</sup>.

$$\psi = \frac{6V_p}{D_p A_p} = \frac{6(9.8174\text{E-}8)}{(0.005)(1.178\text{E-}8)} = 1.00007 \quad (2.6)$$

$L_{\text{bed}}$  is the bed depth of the bed in m.

$\varepsilon$  is void fraction, as volume of void (fluid) over volume of packed bed (fluid + solid).

$u_\infty$  is the free stream velocity.

For the pellet size used, the global kinetic model (GKM) applied in the present work considers the influence of the catalyst to be described only by the density of the catalyst present in the reactor bed. This is reviewed in Secs. 2.1.3.1 and 2.1.3.2.

Ergun's equation can also be written in terms of a friction factor, following Eq. 2.7.

$$\frac{\Delta p}{L_{\text{bed}}} = f \frac{W^2}{\rho A^2} \left( \frac{1-\varepsilon}{D_p \varepsilon^3} \right) \quad (2.7)$$

Where:

$W$  is mass flow in kg/s.

$A$  is the bed's cross-sectional area in m<sup>2</sup>.

$f$  is a friction factor, defined in Eq. 2.8

$$f = \frac{150}{\text{Re}_{\text{bed}}} + 1.75 \quad (2.8)$$

$\text{Re}_{\text{bed}}$  is the packed bed Reynolds number, described in Eq. 2.9.

$$\text{Re}_{\text{bed}} = \frac{W}{A\mu} \left( \frac{D_p}{1-\varepsilon} \right) \quad (2.9)$$

### 2.1.3 Reaction kinetics

Reaction models for catalytic reactions can take the form of micro-kinetic models (MKM), which describe a large number of sequential reactions that occur on the surface layers of the catalyst. Through experimental lab work, prominent paths are derived for the formation of products, which can simplify the MKM into a global kinetic model (GKM). This has the advantage of reducing computation power.

A prominent example of a MKM for methanol synthesis over a copper-based catalyst would be the work by Ovesen et al. (1997) establishing a set of 13 elementary steps. From this work, many GKMs were developed since then. It has been reported by Mäyrä and Leiviskä (2017) that for methanol synthesis at industrial working conditions, GKMs can describe the behavior of the reactor more

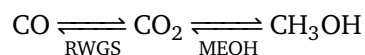
<sup>v</sup>The value obtained of  $\psi = 1$  means that in this equation the cylindrical pellets have a similar behavior to that of spherical pellets of the same diameter.

accurately than MKM. For dynamic models where the conditions of the catalyst vary over time, detailed MKMs are preferred.

For global kinetic models, the production of methanol from a feed of syngas using a Cu / ZnO / Al<sub>2</sub>O<sub>3</sub> catalyst is composed of three main reactions: CO<sub>2</sub> hydrogenation (MEOH), reverse water-gas shift (RWGS) and CO hydrogenation, as presented in Eqs. 2.1, 2.2, 2.3, respectively.

In the 1980s the predominant model by Graaf et al. (1986) considered CO hydrogenation to be the dominant path for the formation of methanol. The consensus has since shifted and CO<sub>2</sub> hydrogenation is the prominent precursor to methanol production for the operating conditions of the modern chemical industry. Hence, it has been determined that the reaction in Eq. 2.3 is less prominent for methanol synthesis [12, 17].

According to experimental results by Bussche and Froment (1996), the primary reactions (Eq. 2.1 and Eq. 2.2) are competing to transform the carbon from the feed, in the following sequence:



For a tubular reactor such as the MBR, the evolution of the reactions will behave as presented in Fig. 2.8. Near the inlet, CO<sub>2</sub> will react to produce both CO and CH<sub>3</sub>OH (*green*). However, as the CO<sub>2</sub> concentration decreases, coupled with the endothermic nature of the RWGS reaction, it will slow down the hydrogenation of CO<sub>2</sub>. Once the RWGS reaches equilibrium and switches direction (visible in the CO peak) both methanol and water will be produced simultaneously (*blue*). The temperature of the reactor bed will increase due to the exothermic nature of the MEOH reaction until an equilibrium is reached (*white*).

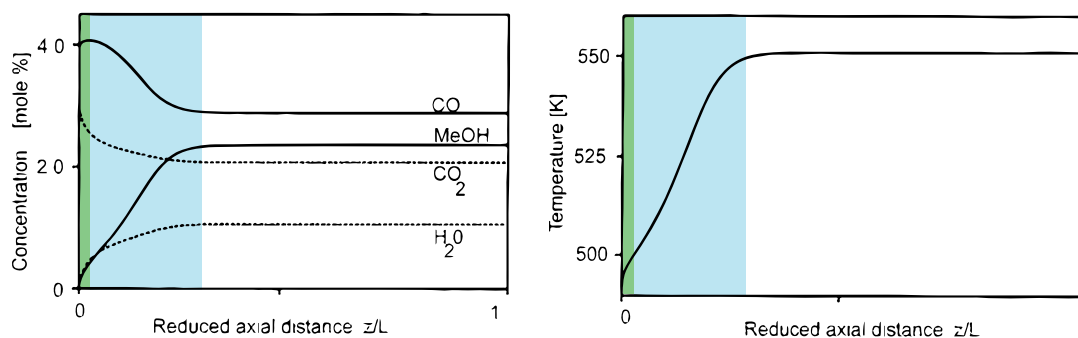


Fig. 2.8. Concentration and temperature profiles in an adiabatic methanol synthesis reactor [12].

### 2.1.3.1 Global kinetic model of Bussche and Froment

Bussche and Froment took the micro-kinetic model from Ovesen et al. and used it as a backbone to create a Langmuir-Hinshelwood GKM. It groups parameters of intermediate surface products into adsorption constants for species  $K_{ai}$  and uses a single type of surface center for the reactions represented by the surface coverage  $\theta$ . This model considers no changes to occur at the surface of the catalyst over time.

$$r_1 = k_1 p_{\text{CO}_2} p_{\text{H}_2} \left( 1 - \frac{1}{K_{e1}} \frac{p_{\text{H}_2\text{O}} p_{\text{CH}_3\text{OH}}}{p_{\text{H}_2}^3 p_{\text{CO}_2}} \right) \theta^3 \quad (2.10)$$

$$r_2 = k_2 p_{\text{CO}_2} \left( 1 - \frac{1}{K_{e2}} \frac{p_{\text{H}_2\text{O}} p_{\text{CO}}}{p_{\text{H}_2} p_{\text{CO}_2}} \right) \theta \quad (2.11)$$

$$\theta = \left( \frac{1}{1 + K_{a1} \sqrt{p_{\text{H}_2}} + K_{a2} p_{\text{H}_2\text{O}} + K_{a3} \frac{p_{\text{H}_2\text{O}}}{p_{\text{H}_2}}} \right) \quad (2.12)$$

Where:

$r$  are reaction rates in units of  $\text{mol} \cdot \text{kg}_{\text{cat}}^{-1} \cdot \text{s}^{-1}$ .

$p_i$  is the partial pressure of species  $i$  in bar.

$k_i, K_{ai}$  are values for rate constant and adsorption constant, presented in Tab. 2.1.

$K_{ei}$  are equilibrium constants obtained from Graaf et al. (1986) (See Eq. 2.24)

**Tab. 2.1.** Parameters from Bussche and Froment (1996) for reaction ( $k$ ) and adsorption ( $K_a$ ) constants.

$$\gamma_i = A_i \exp\left(\frac{B_i}{RT}\right)$$

$\gamma$	$A$	$B$
$k_1$	1.07	36696
$k_2$	1.22E+10	-94765
$K_{a1}$	0.499	17197
$K_{a2}$	6.62E-11	124119
$K_{a3}$	3453.38	0.0

This model has been thoroughly tested for industrial processes at the pressure and temperature ranges on which the MBR will operate [9, 18].

Some limitations on the model lie in the experimental data used to derive it. The highest pressure used for sampling by Bussche and Froment was 50 bar. Methanol conversion also diverges from experimental values for feed compositions containing CO between 4-15 mole%, as evidenced by Klier et al. (1982).

### 2.1.3.2 Global kinetic model of Seidel

A new global reaction model has been developed by Seidel et al. (2018) as an improvement of the work by Bussche and Froment (1996). There three major differences:

1. It uses all three major reactions for methanol production (Eqs. 2.1, 2.2, 2.3).
2. It adds a dynamic morphology parameter which considers the changes on the catalyst surface due to the varying degrees of oxidation and reduction on the outermost copper layer.
3. It considers three active centers for the surface coverage  $\theta$  (see Fig. 2.9):
  - ⊙: Oxidized (active for CO hydrogenation).
  - \*: Reduced (active for CO<sub>2</sub> hydrogenation).
  - ⊗: Active for heterolytic H<sub>2</sub> decomposition.



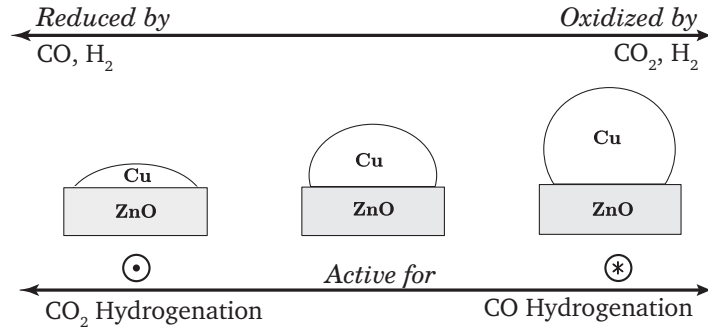


**Fig. 2.9.** Diagram for morphology changes on the catalyst surface. A gas with reduction potential ( $\text{CO}, \text{H}_2$ ) forms a Cu-ZnO alloy on the surface, which makes catalyst more active for the CO hydrogenation. Meanwhile, a gas with oxidizing potential ( $\text{CO}_2, \text{H}_2\text{O}$ ) will make the Cu particle more spherical and active for the  $\text{CO}_2$  hydrogenation [20].

As shown in Fig. 2.9, the changes in the concentration of  $\text{CO} / \text{CO}_2$  in the feed affect the morphology of the catalyst. This effect becomes significant when considering a **variable composition over time**. The model is specifically designed to evaluate applications where varying ratios of  $\text{CO}$  and  $\text{CO}_2$  are present in the reactor; such is the case of the MBR.

The research by [Seidel et al.](#) establishes a Langmuir-Hinshelwood kinetic model, consisting of the following rate equations:

$$r_1 = k_1 p_{\text{CO}_2} p_{\text{H}_2}^2 \left( 1 - \frac{1}{K_{e1}} \frac{p_{\text{CH}_3\text{OH}} p_{\text{H}_2\text{O}}}{p_{\text{CO}_2} p_{\text{H}_2}^3} \right) \theta^{*2} \theta^{\otimes 4} \quad (2.13)$$

$$r_2 = k_2 p_{\text{CO}_2} \left( 1 - \frac{1}{K_{e2}} \frac{p_{\text{CO}} p_{\text{H}_2\text{O}}}{p_{\text{CO}_2} p_{\text{H}_2}} \right) \theta^* \theta^{\circ} \quad (2.14)$$

$$r_3 = k_3 p_{\text{CO}} p_{\text{H}_2}^2 \left( 1 - \frac{1}{K_{e3}} \frac{p_{\text{CH}_3\text{OH}}}{p_{\text{CO}} p_{\text{H}_2}^2} \right) \theta^{\circ} \theta^{\otimes 4} \quad (2.15)$$

With their respective surface coverages:

$$\theta^{\circ} = \left( 1 + \gamma_{11} p_{\text{CO}} + \gamma_{12} p_{\text{CH}_3\text{OH}} + \gamma_{14} p_{\text{CO}_2} \right)^{-1} \quad (2.16)$$

$$\theta^{\otimes} = \left( 1 + \gamma_{12} \sqrt{p_{\text{H}_2}} \right)^{-1} \quad (2.17)$$

$$\theta^* = \left( 1 + (\gamma_{10} \gamma_9 \gamma_7^{-2}) \frac{p_{\text{H}_2\text{O}}}{p_{\text{H}_2}} + \gamma_{13} p_{\text{CO}_2} + \gamma_8 p_{\text{CH}_3\text{OH}} + \gamma_9 p_{\text{H}_2\text{O}} \right)^{-1} \quad (2.18)$$

Where:

$k_i$  are reaction rate constants from Eq. 2.19<sup>vi</sup>.

$K_{ei}$  are equilibrium constants from [Graaf and Winkelman \(2016\)](#) (See Eq. 2.25).

$\gamma$  are grouped parameters used to arrange complex sequential reactions into single terms. Values presented in Tab. 2.2.

$T_{\text{ref}}$  is 523.15 K.

$$k_i = \exp \left( \underbrace{A}_{\gamma_1, \gamma_3, \gamma_5} - \underbrace{B}_{\gamma_2, \gamma_4, \gamma_6} \left( \frac{T_{\text{ref}}}{T} - 1 \right) \right) \quad (2.19)$$

<sup>vi</sup> $k_1$  uses  $\gamma_1$  and  $\gamma_2$ .  $k_2$  uses  $\gamma_3$  and  $\gamma_4$ .  $k_3$  uses  $\gamma_5$  and  $\gamma_6$

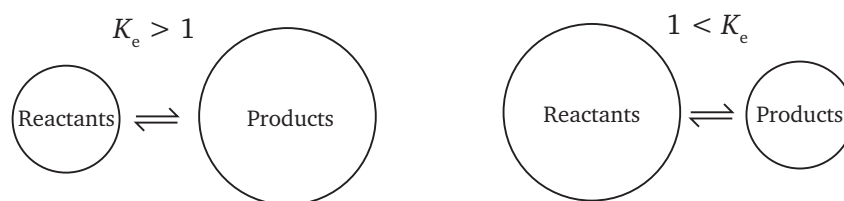
**Tab. 2.2.** Grouped parameters for the Langmuir-Hinshelwood reaction model by Seidel et al. (2018)

$i$	$\gamma$	units
1	-3.4112	-
2	3.447	-
3	-5.7239	-
4	23.4744	-
5	-4.7636	-
6	26.1883	-
7	1.1665	bar <sup>-0.5</sup>
8	0	bar <sup>-1</sup>
9	0.0297	bar <sup>-1</sup>
10	1.60E+03	-
11	0.147	bar <sup>-1</sup>
12	0	bar <sup>-1</sup>
13	0.04712	bar <sup>-1</sup>
14	0	bar <sup>-1</sup>

While the current research does not use the Seidel et al. model, it is **strongly recommended** to implement it for future modeling of the MBR if higher operating pressures or higher CO concentrations are observed in the reactor operation. According to on-going research from Bos and Brilman, this model has proven to be more accurate to their convective flow reactor at operating pressures higher than 50 bar.

### 2.1.3.3 Equilibrium constants

The equilibrium constant  $K_e$  is the ratio of concentration of products to reactants in a reversible reaction. A value larger than unity means that reaction favors the products. If the constant is smaller than one, the equilibrium will favor the reactants. This concept is represented in Fig. 2.10.

**Fig. 2.10.** Visual representation of equilibrium constants

$$K_e = \frac{\prod_i [\text{products}]_i}{\prod_i [\text{reactants}]_i}$$

For the reversible chemical reactions presented in this work (Eqs. 2.1, 2.2 and 2.3), the equilibrium constants expressed in terms of species' concentration are presented in Eqs. 2.20, 2.21 and 2.22, respectively.

$$K_{e1} = \frac{[\text{CH}_3\text{OH}][\text{H}_2\text{O}]}{[\text{CO}_2][\text{H}_2^3]} \quad (2.20)$$

$$K_{e2} = \frac{[\text{CO}][\text{H}_2\text{O}]}{[\text{CO}_2][\text{H}_2]} \quad (2.21)$$

$$K_{e3} = \frac{[\text{CH}_3\text{OH}]}{[\text{CO}_2][\text{H}_2^2]} \quad (2.22)$$

For a fixed temperature, a chemical equilibrium is reached when the change of Gibb's free energy of the components has reached zero. In practice, it means that the mixture composition ceases to vary.

$$\Delta G = -RT \ln(K_e)$$

For an ideal gas, equilibrium constants can be determined with Eq. 2.23. Once these are calculated, correction factors are applied for non-ideal gas behavior at higher pressures. Graaf et al. (1986) showed that the Soave-Redlich-Kwong equation of state (SRK EOS) is suitable for said correction in the reaction conditions present for methanol synthesis. For pressures higher than 100 bar, a modified version of the SRK EOS should be used to account for the non-ideality of the gas, as evidenced in the work of Bennekom et al. (2012), though that is outside the scope of the current research.

$$\ln(K_e^\circ(T)) = \frac{1}{R} \left( \frac{-\Delta G^\circ(T_{\text{ref}})}{T_{\text{ref}}} + \int_{T_{\text{ref}}}^T \frac{\Delta H^\circ(T)}{T^2} dT \right) \quad (2.23)$$

Where:

$$\Delta H^\circ(T) = \Delta H^\circ(T_{\text{ref}}) + \int_{T_{\text{ref}}}^T \frac{\Delta c_p^\circ(T)}{T^2} dT$$

It was evidenced by Graaf and Winkelman (2016) that inaccuracies in experimentally determining values for  $\Delta H^\circ(T_{\text{ref}})$  and  $\Delta G^\circ(T_{\text{ref}})$  have lead to historical discrepancies for temperature fitting correlations for  $K_e$ . A large compendium of experimentally measured equilibrium constants are presented in Fig. 2.11, and their temperature fitting functions in Eqs. 2.24 and 2.25.

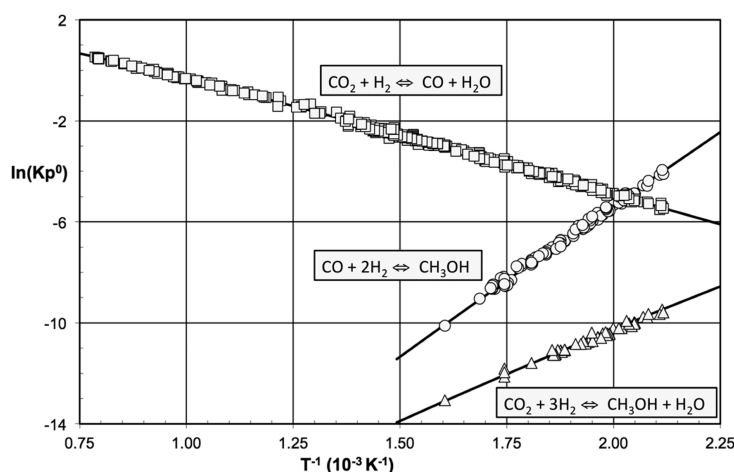


Fig. 2.11. Compendium of experimentally obtained equilibrium constants for methanol synthesis reactions by Graaf and Winkelman (2016).

The reaction rates by [Bussche and Froment](#) used the original equilibrium constants by [Graaf et al. \(1986\)](#) and are used in the current research, as these have a faster computation time. Meanwhile, the rates of [Graaf and Winkelman \(2016\)](#) are used for the more recent [Seidel et al.](#) model.

**Graaf et al. (1986)**

$$\log_{10}(K_{e1}) = \frac{3066}{T} - 10.592; \quad \log_{10}(K_{e2}) = -\frac{2073}{T} + 2.029; \quad K_{e3} = K_{e1}/K_{e2} \quad (2.24)$$

**Graaf and Winkelman (2016)**

$$K_{e1} = K_{e2}K_{e3}; \quad \ln(K_{e2}) = \frac{1}{RT} \left( \sum_{j=0}^5 a_j T^j + a_6 T \ln(T) \right); \quad \ln(K_{e3}) = \frac{1}{RT} \left( \sum_{j=0}^5 b_j T^j + b_6 T \ln(T) \right) \quad (2.25)$$

Where:

- ◇ Reaction Eq. 2.1 is the stoichiometric sum of reactions Eq. 2.2 and Eq. 2.3, thus if two reactions are in equilibrium with each other, the third will also be in equilibrium.
- ◇ Values for  $a_j$  and  $b_j$  are presented in Tab. 2.3

**Tab. 2.3.** Parameters for equilibrium constants from [Graaf and Winkelman \(2016\)](#)

$j$	$a$	$b$
0	-3.9412E4	7.4414E4
1	-5.4152E1	1.8926E2
2	-5.5642E-2	3.2443E-2
3	2.5760E-5	7.0432E-6
4	-7.6594E-9	-5.6053E-9
5	1.0161E-12	1.0344E-12
6	1.8429E1	-6.4364E1

**2.1.3.4 Equilibrium product composition**

Considering the equilibrium constants by from [Graaf et al.](#) in Eq. 2.24, the reaction product composition at equilibrium can be obtained as a function of the feed composition, pressure and temperature. A composition in equilibrium must follow the conditions of Eqs. 2.26 and 2.27.

$$10^{\frac{3066}{T}-10.592} = \frac{f_{\text{CH}_3\text{OH}}f_{\text{H}_2\text{O}}}{f_{\text{CO}_2}f_{\text{H}_2}^3} \quad (2.26)$$

$$10^{-\frac{2073}{T}+2.029} = \frac{f_{\text{CO}}f_{\text{H}_2\text{O}}}{f_{\text{CO}_2}f_{\text{H}_2}} \quad (2.27)$$

The feed composition going into the reactor is comprised of  $\text{H}_2/\text{CO}_2$  at a ratio of 0.75/0.25. The carbon provided by the  $\text{CO}_2$  converts into  $\text{CO}$  and  $\text{CH}_3\text{OH}$ . Their respective molar fractions for an equilibrium product composition at a pressure range of 10-100 bar and select temperatures is presented in Fig. 2.12. As the goal is to produce methanol, a higher fraction of  $\text{CH}_3\text{OH}$  acts as a selection criteria for operational set points of pressure and temperature in the MBR.

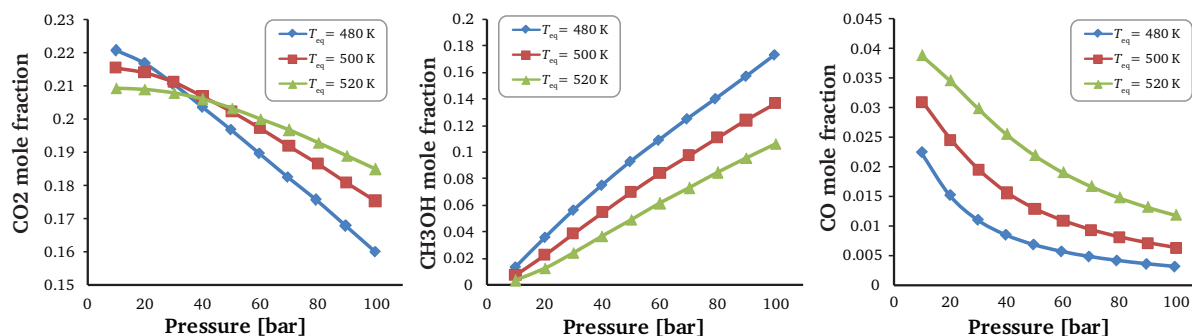


Fig. 2.12. Mole fraction of reaction products at equilibrium from a feed of  $H_2/CO_2$  at a 0.75/0.25 ratio. Values obtained from flashing composition in COCO™ using SRK EOS.

The following can be observed from Fig. 2.12:

- ◇ At lower temperature and higher pressure, the products at equilibrium will favor methanol over carbon monoxide.
- ◇ Equilibrium temperature has a higher influence on the composition of the products than pressure; ie. from Fig. 2.12b, reducing the reactor temperature will shift the equilibrium for methanol as if the pressure were raised 15 bar.
- ◇ Based on the information from Fig. 2.2, a higher content of CO in the feed will lead to a much higher content of methanol in the products at equilibrium. This is the reason why **industrial reactors require separation and recirculation**, as the equilibrium does not favor methanol.

If the MBR were a conventional single pass (equilibrium) methanol synthesis reactor, choosing any combination of temperature and pressure from Fig. 2.12 would be the maximum composition of methanol obtainable by passing through the catalyst bed. The separation of the unreacted gases ( $CO_2$  and  $CO$ ) through in-situ condensation of methanol and water will vary the feed composition inside the reactor over time, shifting the product equilibrium in favor of methanol. This is the principle that lead the system by [Bos and Brillman](#) to have a “carbon conversion to methanol above 99.0%”[7].

#### Experimental equilibrium composition

In the work reported by [Basarkar](#), the operational values for temperature and pressure of the SMBR are of 501.15 K and 50 bar. The equilibrium product composition from the feed used is presented in Tab. 2.4. The process of obtaining the dew point temperature for the gas mixture is reported in Sec. 2.2.2.

Tab. 2.4. Equilibrium composition for products at MBR working conditions from a feed of 0.75/0.25 of  $H_2/CO_2$  at 501.15 K and 50 bar.

	Value	Unit
$H_2$	0.6338	mol/mol
$CO$	0.0133	mol/mol
$CO_2$	0.2024	mol/mol
$H_2O$	0.0819	mol/mol
$CH_3OH$	0.0686	mol/mol
$T_{dew}$	415.74	K

It should be noted that this gas composition is **never reached in the SMBR operation**, it only serves as a reference for dew temperature.

## 2.2 Condensation

One of the most innovative components of the methanol synthesis reactor from [Bos and Brilman](#) is the inclusion of an in-situ separation component that also serves the function of driving the flow. To properly set the reactor working conditions, it is important to understand the temperature difference due to the reaction temperature (from to chemical equilibrium) and the condensation temperature (from phase equilibrium).

The gases inside the SMBR are a mixture of five unique species:  $H_2$ ,  $CO_2$ ,  $CO$ ,  $H_2O$  and  $CH_3OH$ . In the current section, the condensation of a multicomponent mixture is studied as a single stage flash. A brief overview of the dew point temperature for reactant products at multiple equilibrium conditions is presented afterwards. The goal is to present the **nuances of selecting an operating pressure and temperature** for a convective loop reactor.

The mechanisms for droplet formation in the condenser portion of the reactor are not discussed in the present research. These are multiphase heat and mass transfer studies beyond the scope of this project.

### 2.2.1 Single stage flash

The single-stage flash is the simplest vapor-liquid equilibrium model available for any calculation of a multicomponent mixture. Consider the schematic drawing of [Fig. 2.13](#). If all information of the feed is known (composition  $z_i$ , molar flow-rate  $F$  and enthalpy  $H$ ), it is possible to find the rest of the values by (iteratively) solving the balance equations [2.28-2.32](#) and the equations of state.

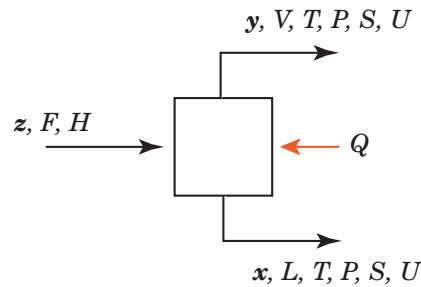


**Fig. 2.13.** Schematic diagram of single-stage flash

- ◇ Phase equilibrium:

$$y_i = \frac{\left(\frac{f_i}{p_i}\right)^L}{\left(\frac{f_i}{p_i}\right)^V} x_i \quad (2.28)$$

- ◇ Species mass balance:

$$x_i \phi^L + y_i \phi^V = z_i \phi \quad (2.29)$$

- ◇ Total mass balance:

$$\phi^L + \phi^V = \phi \quad (2.30)$$

- ◇ Constitutive:

$$\sum_i^N x_i = \sum_i^N y_i = 1 \quad (2.31)$$

- ◇ Enthalpy balance

$$H_L \phi^L + H_V \phi^V + H_F \phi = Q \quad (2.32)$$

Where:

$x_i, y_i$  are the liquid and vapor fractions of each species, respectively.

$f_i$  is the fugacity of each species in the specific phase.

$p_i$  is the partial pressure each species in the specific phase.

$L, V, F$  are the liquid, vapor and feed molar rates.

$N$  is the number of species

$H$  is the enthalpy of the stream.

The most important values to determine from a flash are the vapor and liquid composition  $x_i$  and  $y_i$ . That leaves  $T, p, Q, U, S$  and  $\phi^L$  (or  $\phi^V$ , as they're interdependent) unknown. By setting at least two of these to specified values the rest can be obtained. Chemical engineering practices have established typical pairings of independent variables which can be used to determine the state of the system. These are known as **flashes** and the most common ones are defined as follows:

1. Pressure-enthalpy ( $p-H$ )
2. Pressure-temperature ( $p-T$ )
3. Pressure-vapor fraction ( $p-\frac{V}{F}$ )
4. Temperature-vapor fraction ( $T-\frac{V}{F}$ )
5. Pressure-entropy ( $S-H$ )
6. Pressure-internal energy ( $p-U$ )

Throughout history, computational methods have been developed to solve for the equilibrium composition of a multicomponent mixture. The most optimized algorithms use a combination of constitutive relations, equations of state and thermophysical property models to determine the equilibrium composition in the least amount of iterations possible.

The flash algorithm deployed in the COCO™ simulator was developed by Parekh and Mathias (1998) as an improvement to the approach by Boston and Britt (1978). The original method by Boston and Britt only permitted a flash to arrive into a two-phase. If the composition was to remain as single-phase it would converge into the phase boundary (dew or bubble point) with significant error in the energy balance [23]. The work from Parekh and Mathias was aimed at fixing this issue by simply adding a complementary flash to any method, ie. if performing a  $p-H$  flash, execute a secondary  $p-T$  flash to ensure energy balance is achieved.

The analysis of multiple component mixture condensation in this current research will be limited to the implementation of the aforementioned algorithms in the COCO™ simulator [25], as it provides an efficient solver for relating both chemical and phase equilibrium.

### 2.2.2 Condensation of reaction products

Knowing the temperature at which the mixture becomes a two-phase fluid is an operational set point for the condenser in the MBR. To achieve the condensation of reactant products, its working temperature should be below the dew point temperature of the gas mixture.

The dew point temperature is defined in terms of fugacity as the highest temperature for which the phase equilibrium Eq. 2.28 is valid for a fixed composition and pressure.

Using COCO™ simulator's implementation of phase equilibrium and extending the analysis of reaction products at chemical equilibrium done in Sec. 2.1.3.4, a set of dew point temperatures is obtained for a range of temperatures and pressures from the H<sub>2</sub>/CO<sub>2</sub> feed at 0.75/0.25 ratio. The information is presented in Fig. 2.14 and compared with the data reported by Bos and Brilman (2015)<sup>vii</sup>.

---

<sup>vii</sup>Bos and Brilman used a modified SRK EOS from Bennekom et al. (2012), but the differences to the normal SRK EOS are not present for the reported values in the pressure range of 10-100 bar

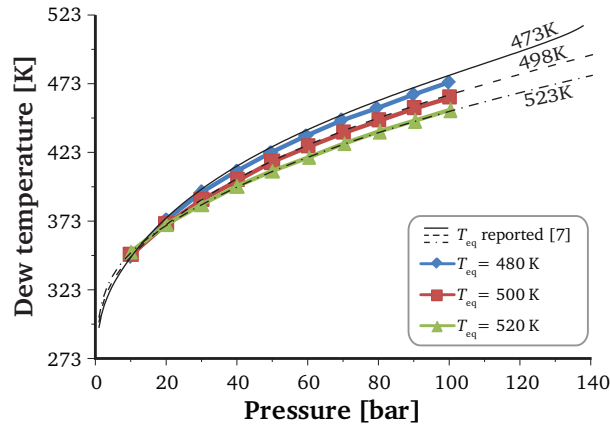


Fig. 2.14. Dew temperature for reaction product at chemical equilibrium for select temperatures and a pressure range. Comparison of values obtained in current research with those reported by [Bos and Brilman \(2015\)](#).

As it was mentioned in Sec. 2.1.3, a temperature difference between the hot reactor temperature (chemical equilibrium temperature  $T_{eq}$ ) and the cold condenser temperature ( $<T_{dew}$ ) is required to create a buoyant force that will drive the fluid through the circulation loop. The size of this temperature difference for the previously selected temperature and pressures is presented in Fig. 2.15.

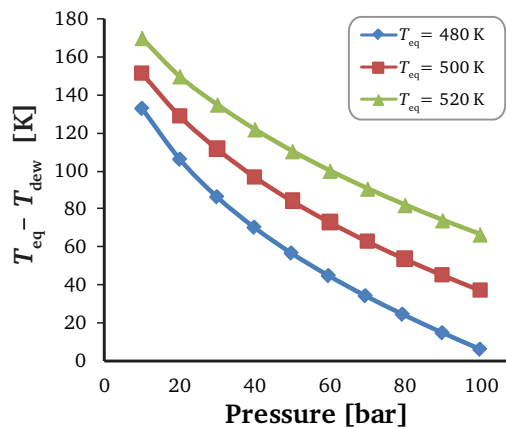


Fig. 2.15. Temperature difference for product equilibrium and dew point temperature.

In summary, higher pressures and lower reactor temperatures will shift the equilibrium in favor of methanol (as seen in Fig. 2.12), but the product will have a higher condensation temperature, thus a smaller temperature difference between reactor and condenser (as seen in Fig. 2.15).

A greater temperature difference between the hot and cold section will increase the available driving force, but is **not the only defining term for the buoyant force**. Density  $\rho$  and the positioning of the heating and cooling elements in the vertical axis also influence the buoyant force. A discussion of the forces driving the flow is done in Sec. 2.3, though it is limited to the positioning of the heating / cooling elements. An analysis of the influence of pressure as a means to maximize buoyant forces through increasing density is out of the scope of the current research.



## 2.3 Flow in natural circulation loops

Natural circulation loops (NCL) are flow systems that use buoyancy forces to drive a fluid inside a closed loop. The fluid circulates due to a thermally induced density difference in a body-force field (gravity).

These systems are traditionally used in applications to **remove heat** from processes that require the least amount of equipment possible, either for lack of space (electronic cooling), low energy availability (solar thermo-siphons) or high reliability for continuous operation (cooling of nuclear reactor core).

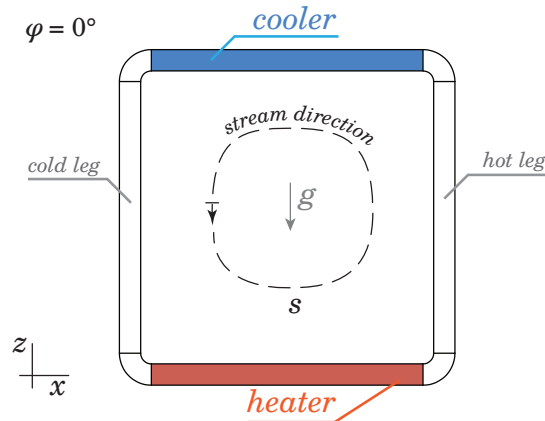


Fig. 2.16. Diagram of UDL in a horizontal heater and cooler configuration. Tilting angle  $\varphi = 0$ .

In its most basic form, a NCL can be represented by Fig. 2.16; note that the loop is of uniform diameter (UDL). The equations for continuity, momentum and energy are presented in Eqs. 2.33-2.35 for a one-dimensional incompressible flow with negligible viscous dissipation and axial conduction effects. Boundary conditions set the heater with a uniform heat flux  $q_h$ , the cooler with a fixed temperature  $T_c$  and heat transfer coefficient  $U$ . Both vertical legs have no heat losses.

◇ Continuity:

$$\frac{\partial W}{\partial s} = 0 \quad (2.33)$$

◇ Momentum:

$$\frac{L_t}{A} \frac{dW}{dt} = g\rho_o\beta \oint T dz - \frac{W^2}{\rho_o A^2} \left( \frac{f L_t}{D} \right) \quad (2.34)$$

◇ Energy:

$$\frac{\partial T}{\partial t} + \frac{W}{\rho_o A} \frac{\partial T}{\partial s} = \begin{cases} \frac{q_h P}{\rho_o c_p A} & \text{heater} \\ 0 & \text{vertical legs} \\ -\frac{UP(T-T_c)}{\rho_o c_p A} & \text{cooler} \end{cases} \quad (2.35)$$

Where:

$A$  is the cross-section area of the loop in  $\text{m}^2$ .

$W$  is mass flow in  $\text{kg/s}$ .

$L_T$  is the total length of the loop in  $\text{m}$ .

$\beta$  is the thermal expansion coefficient in  $\text{K}^{-1}$ . Following Boussinesq approximation [26]:

$$\rho(T) = \rho_o(1 - (T - T_o)\beta); \quad \beta = -\frac{1}{\rho} \left( \frac{\partial \rho}{\partial T} \right)_p$$

$f$  is a friction term for the loop.

$P$  is the perimeter of the loop in m.

From these equations, a correlation that links the flow-rate to the heat input into a NCL has been derived by Vijayan (2002) for both laminar and turbulent regimes. It was further improved by Swapnalee and Vijayan (2011) for the transient regime and also for **non-uniform diameter loops**.

The current research uses these values as a first suggestion of the behavior for the flow-rate in the MBR, and then proceeds to create their own correlations for the particular orientation of the reactor ( $0 > \varphi \geq 90$ ); see Sec. 4.1.

There are some notable studies for NCLs with different configurations than of a horizontally positioned heater and cooler (tilting angle  $\varphi = 0$ ), though these have a heavier focus on the instabilities inside the fluid, rather than the resulting mass flow [29–32]. While the current research does not focus on flow stability, some of these works do **provide a suggestion of how the flow-rate will be affected** by tilting the loop.

### 2.3.1 Generalized correlation for single-phase flow

Consider the following changes to Eqs. 2.33-2.35 for a loop of length  $s = 1$  at steady-state:

- ◇ All transient parameters tend to zero.

$$\frac{\partial}{\partial t} = 0$$

- ◇ Integrating the energy equation from the boundary condition that at  $s = 0$ ,  $T = T_{\text{cold leg}}$  to obtain the steady-state temperature of the heater as it passes through the heater:

$$T = \frac{q_h P}{W c_p} s + T_{\text{cold leg}}$$

- ◇ The energy equation can also be integrated at the cooler location, considering that at  $s = 0.5$  (at the hot leg),  $T = T_{\text{hot leg}}$

$$T = T_c + (T_{\text{hot leg}} - T_c) \exp\left(\frac{UP(0.5 - s)}{W_{ss} c_p}\right)$$

- ◇ Knowing these temperatures, the closed integral with the temperature term in Eq. 2.35 is solved for steady-state:

$$\oint T dz = (T_{\text{hot leg}} - T_{\text{cold leg}})H = \left(\frac{Q_h}{W_{ss} c_p}\right)H$$

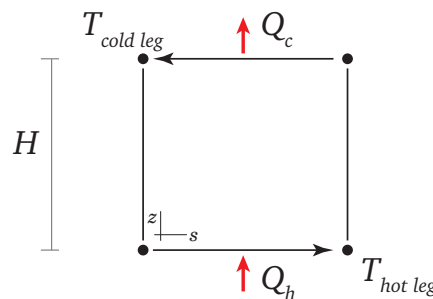


Fig. 2.17. Visual representation of  $\oint T dz$ . For steady-state  $Q_h = -Q_c = W_{ss} c_p (T_{\text{hot leg}} - T_{\text{cold leg}})$

- ◇ Darcy friction factor  $f$  for the fluid inside a tube [33] follows a general form of:

$$f = p \text{Re}^{-b}$$

- ◇ The momentum equation 2.34 for steady-state now becomes:

$$g\rho_o\beta\left(\frac{Q_h H}{W_{ss}c_p}\right) = \frac{W_{ss}^2}{2D_o\rho_oA_o^2}\left(\frac{pL_t}{\text{Re}_{ss}^b}\right) \quad (2.36)$$

- ◇ Remaining terms of the momentum equation are replaced for dimensionless parameters, as:

$$\text{Gr}_m = \frac{D_o^3\rho_o^2\beta g}{A_o\mu^3}\left(\frac{Q_h H}{c_p}\right) \quad (2.37)$$

$$\text{Re}_{ss} = \frac{D_o W_{ss}}{A_o\mu} \quad (2.38)$$

$$N_g = \frac{L_t}{D_o} \quad (2.39)$$

From the steady-state momentum equation Eq. 2.36, a relation between the steady-state Reynolds number and the modified Grashoff number can be established. The general form is presented in Eq. 2.40, where  $r = 1/(3 - b)$  and  $C = (2/p)^r$ <sup>viii</sup>.

$$\text{Re}_{ss} = C\left(\frac{\text{Gr}_m}{N_g}\right)^r \quad (2.40)$$

Three sets of values for  $C$  and  $r$  constants have been evaluated experimentally by Vijayan for rectangular loops with a fully laminar, turbulent regime. A correlation was later made for a fully transient regime loop by Swapnalee and Vijayan. These values are presented in Tab. 2.5. Notice the transition from **laminar to turbulent occurs at much lower Re values** than for fluid traveling inside straight pipes.

Tab. 2.5. Experimental values for coefficients of Eq. 2.40 [28].

Condition	$C$	$r$	$p$	$b$
Laminar (Re < 898)	0.1768	0.5	64	1
Transition (898 < Re < 3196)	1.2160	0.3870	1.2063	0.416
Turbulent (Re > 3196)	1.9560	0.3640	0.316	0.25

The dimensionless numbers of Re and  $\text{Gr}_m$  are used to describe the behavior of a loop, as **these scale with flow-rate and power input**, respectively. The geometric parameter  $N_g$  represents the geometry of the loop. Plotting the correlations in Fig. 2.18 act as a visual representation of the relation between these dimensionless numbers.

---

<sup>viii</sup>Recall Darcy-Weisbach's friction factors for fully developed regimes are  $b = 1$ ,  $p = 64$  for laminar flows and  $b = 0.25$ ,  $p = 0.316$  for turbulent flows following blasius correlation [28].

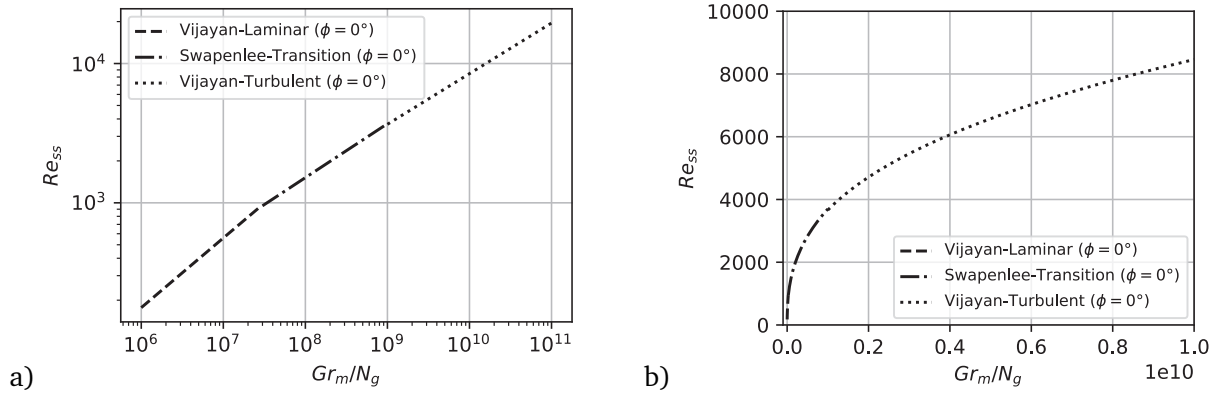


Fig. 2.18.  $Re$  vs  $Gr_m/N_g$  plots for a horizontal single-phase NCL [28]. a) Log-log plot. b) Cartesian plot.

It is possible for Eq. 2.40 to describe a non-uniform natural circulation loop by adjusting the geometric parameter to account for the ratio of each fluid regime present in the loop [28].

$$N_g = \frac{L_t}{D} \left( \frac{p_1}{p_3} L_1 \frac{Re_3^{b_3}}{Re_1^{b_1}} + \frac{p_2}{p_3} L_2 \frac{Re_3^{b_3}}{Re_2^{b_2}} + L_3 \right) \quad (2.41)$$

### 2.3.1.1 Limitations on generalized correlation

The correlations by Vijayan are not directly applicable to the MBR configuration. There are still two major differences:

- ◇ The orientation of the heating and cooling sections are vertical.
- ◇ Fluid properties have larger changes that make Boussinesq approximation invalid.

#### Changes in orientation

Other authors have generated their own correlations based on experimental data for differently configured NCLs [34, 35]; none of these are directly applicable to the MBR configuration either.

There have been limited reports of the flow-rate for a vertical orientation NCL. The work of both Basu et al. (2013) and Krishnani and Basu (2017), have been based on **numerical simulations with a focus on flow stability**, not on establishing a relation between flow-rate and heat input.

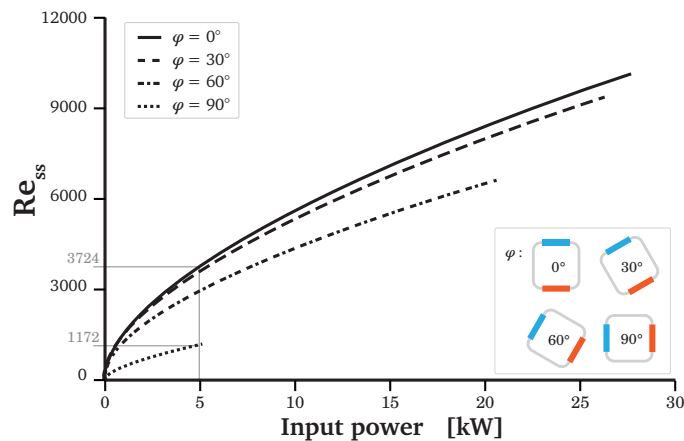


Fig. 2.19. Effect of tilt angle  $\varphi$  to  $Re_{ss}$ . Plots cut off at the point of maximum stable power dissipation [32].

In Fig. 2.23, Krishnani and Basu make the comparison between tilting of  $15^\circ$ ,  $30^\circ$  and  $45^\circ$ . It shows that flow-rate is compromised in favor of stability. Similar observations are seen in Fig. 2.19, where Basu et al. reports that with the increasing of  $\varphi$ , the maximum stable flow-rate reduces. A logarithmic behavior is visible for all lines between Re for  $\varphi = 0$  and  $\varphi = 90$ , which suggests that new values of  $C$  and  $r$  can be obtained for Eq. 2.40 for different tilting angles.

### Variation of fluid properties

In the work by Swapnalee and Vijayan, experiments have been conducted using liquid water at 30 bar with temperature differences no higher than  $30^\circ\text{C}$ . In the reactor operation the gas feed is exposed to a temperature difference between the cold and hot walls 340 and 501K, respectively. The relative variation of the fluid properties on the temperature ranges is much larger, as evidenced in the plots presented in Fig. 2.20.

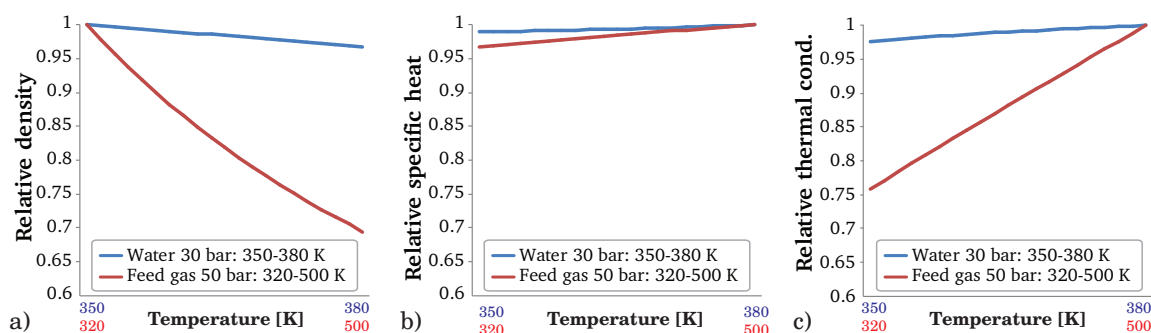


Fig. 2.20. Variation of fluid properties between the water NCL experiments by Swapnalee and Vijayan (2011) and the experimental conditions of the gas feed into the MBR. Values obtained from COCO™ simulator using SRK EOS [25].

The Boussinesq approximation is not accurate for the description of large temperature differences in NCLs, as reported by Krishnani and Basu (2016). It was found that the estimated mass flow is reduced, as presented in Fig. 2.21. The fluid properties in this thesis are calculated at run-time; the specifics of each implementation are explained in Sec. 2.4.1.

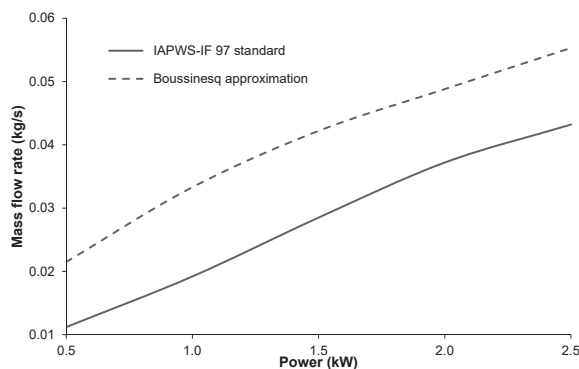


Fig. 2.21. Difference between varying fluid properties (IAPWS standard for simulations of water/steam), and using Boussinesq approximation for  $\rho$  with constant  $c_p$ ,  $\mu$ ,  $\lambda$  [30]. Flow rate is overestimated by a factor of 2 higher [32].

### 2.3.2 Stability of the flow

A NCL is said to be stable when the flow-rate has minimal fluctuations over-time. Perturbations arise when the rate at which the fluid gains heat is larger than the convective flow can remove said heat. These perturbations can take the form of transient spikes in the flow-rate, or in the most extreme cases, **full reversal of the direction** of the flow. This predominantly affects horizontally heated and

cooled NCLs ( $\varphi = 0$ ).

A first comprehensive study for instabilities in NCLs was made by Vijayan et al. (2007) with different locations for the heating and cooling elements. They established a set of stability maps presented in Fig. 2.22. These use a  $Gr_m$  to  $St_m$  to correlate the power that goes into the NCL vs the heat that can be carried by its mass flow. In the areas of the map where the configuration is deemed *unstable*, a chaotic flow with reversals occurs inside the loop. Similar zones with chaotic reversals have been reported by Louisos et al. (2013) in circular NCLs.

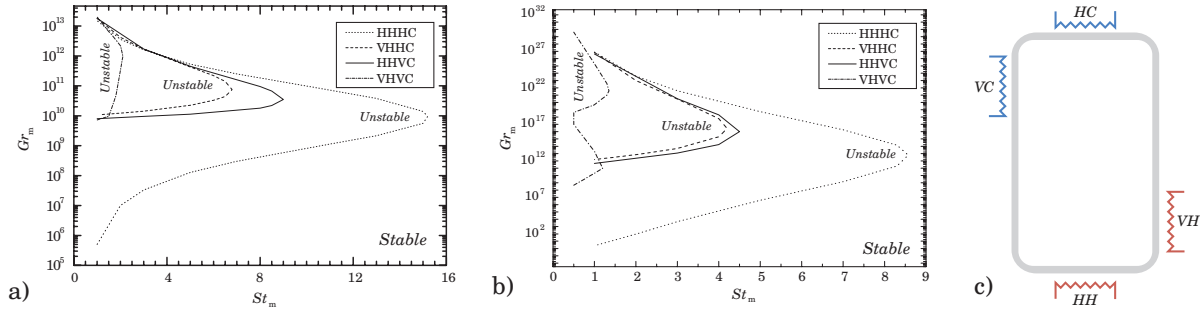


**Fig. 2.22.** Stability maps for NCL with different heating / cooling locations.  $St_m = 4UL_t / Re_{ss}c_p\mu$ . a) Map for fully laminar flow. b) Map for fully turbulent flow. c) Schematic of experimental setup by Vijayan et al.

Because of the overestimation of  $Re$  caused by using the Boussinesq approximation [30], the stability maps from Fig. 2.22 would be **over-sized by a factor of 2** in the  $X$  axis. Nevertheless, they provide some first estimate to possible behavior that may arise in the MBR. So far, neither the computer simulations presented in the current work, nor the experimental characterization of the reactor by Basarkar have shown signs of unstable flow-rates for the MBR geometries.

The work by Krishnani and Basu is essential to summarize the effects of tilting a NCL. This study found that for boundary conditions that would lead to a chaotic flow in a horizontally heated and cooled NCL, a stable convective flow is achieved by tilting the loop only  $15^\circ$ , and further tilting will reduce the steady-state flow rate by a factor approximate to  $\cos \varphi$ . This is presented in Fig. 2.23.

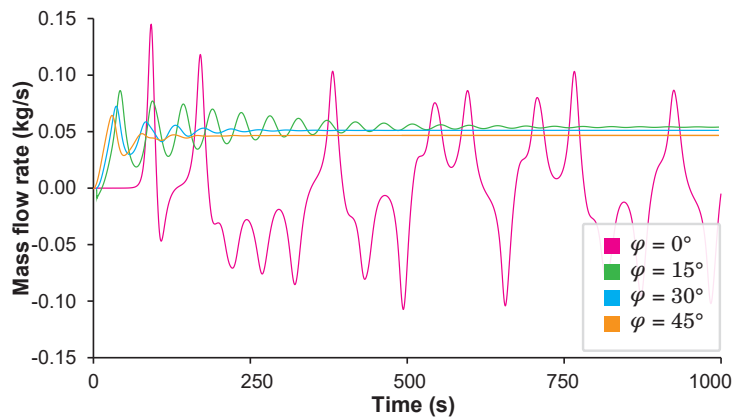


**Fig. 2.23.** Temporal development of flow rate for a NCL. Though it has chaotic behavior for  $\varphi = 0$ , by tilting it, a stable convective flow is achieved. Positive values for flow rate mean circulation in CW direction, negative for CCW direction.

It can be concluded that having a vertically heated and cooled NCL will **limit the maximum flow rate** achieved by the MBR. This was not known before the design process of the reactor, and because initial experiments showed that the reactor produced methanol in its vertical orientation, the objective of the current work is to characterize it as is and suggest possible improvements to its design.

## 2.4 CFD modeling

To describe the behavior of the MBR it is necessary to solve a system of PDEs. Following the work of Pikhwal et al. (2007) and Krishnani and Basu (2016), the CFD package Fluent™ 18.2 was used to solve the governing equations for continuity, momentum and energy presented in Eqs. 2.42-2.44. A RNG  $\kappa$ - $\epsilon$  turbulence model with standard model coefficients are used and presented in Tab. 2.6.

◇ Continuity

$$\frac{\partial \rho}{\partial t} + \frac{\partial}{\partial x_j} (\rho u_j) = 0 \quad (2.42)$$

◇ Momentum

$$\frac{\partial}{\partial t} (\rho u_i) + \frac{\partial}{\partial x_j} (\rho u_j u_i) = -\frac{\partial p}{\partial x_i} + \frac{\partial \tau_{ji}}{\partial x_j} + \rho g_i + S_m \quad (2.43)$$

◇ Energy

$$\frac{\partial}{\partial t} (\rho h) + \frac{\partial}{\partial x_j} (\rho h u_j) = \frac{\partial}{\partial x_j} \left( \lambda^* \frac{\partial T}{\partial x_j} + u_j \tau_{ji} \right) + S_h \quad (2.44)$$

Where:

$\tau$  is the stress tensor given by:

$$\tau_{ji} = (\mu + \mu_t) \frac{\partial u_j}{\partial x_i} = \left( \mu + \rho C_\mu \frac{k^2}{\epsilon} \right) \frac{\partial u_j}{\partial x_i}$$

$h$  is sensible enthalpy defined as:

$$h = \int_{T_{\text{ref}}}^T c_p dT$$

$\lambda^*$  is the thermal conductivity at the boundary layer, defined as:

$$\lambda^* = \lambda + \frac{c_p \mu_t}{\text{Pr}_t}$$

$S_m$  are volumetric momentum sources/sinks, such as a homogeneously packed bed.

$S_h$  are volumetric heat sources/sinks, such as reaction energy.

The equations 2.42-2.44 are solved iteratively using second order upwind schemes for spacial discretization. The pressure-velocity coupling is solved with the SIMPLE algorithm with a PRESTO scheme for the pressure discretization [38]. Default relaxation factors have been observed to be suitable to reach the convergence criteria described in Chapter 3.

Tab. 2.6. Constants for standard  $\kappa$ - $\epsilon$  turbulence model [38]

Constant	Value
$C_\mu$	0.0845
$C_{\epsilon 1}$	1.42
$C_{\epsilon 2}$	1.68
$\text{Pr}_t$	0.85

By considering the fluid as a multicomponent mixture, it is necessary to solve the transport equation for every specie, as presented in Eq. 2.45.

$$\frac{\partial}{\partial t}(\rho\omega_i) + \nabla \cdot (\rho\mathbf{u}\omega_i) = -\nabla \cdot \mathbf{j}_i + S_i \quad (2.45)$$

Where:

- $i$  represents each species. MBR solves for 5 species: H<sub>2</sub>, CO<sub>2</sub>, CO, CH<sub>3</sub>OH, H<sub>2</sub>O.
- $\omega_i$  is each species' mass fraction
- $\mathbf{j}_i$  is each species' diffusion flux, as:

$$\mathbf{j}_i = -\rho D_{i,m} \nabla \omega_i$$

$D_{i,m}$  is the specie's diffusion coefficient into mixture.

$S_i$  are species sources/sinks, which may come from reactions.

The chemical reactions described in Eqs. 2.1 and 2.2 are implemented within Fluent™ as *user-defined functions*. These will have effects in the volumetric sources/sinks of energy  $S_h$  and species  $S_i$ . To account for the changes due to the reactions, the chemistry solver package Chemkin™ is used to solve the species transport equations and determine new fluid properties at run-time based on the fluid mixture composition.

### 2.4.1 Fluid properties

Fluid properties are crucial to achieve physical accuracy of simulations. For single component fluids, most data can be fitted into tables and interpolated for each condition. With multi-component mixtures, it can become more complex. Depending on the application, determining properties can be achieved through different methods, including but not limited to: look-up tables, linear fitting, polynomial fitting or calculation from thermodynamic laws. The method chosen usually comes down to a trade-off between the physical accuracy, computation time and code stability.

Fluent™ and Chemkin provide tools to implement fast and stable fluid properties for the molecules used in the current simulations. For the current research, two sets of approaches are established, as presented in Tab. 2.7.

**Tab. 2.7.** Methods used for calculating fluid properties. Basic used for simulations with a uniform mixture. Detailed used for simulations with multicomponent mixture. Data for basic FP model obtained from COCO™ simulator [25]. Values from Detailed FP model calculated by Chemkin™ at runtime from thermodynamic and transport properties databases [39].

	Basic FP	Detailed FP
Density	3rd order polynomial fit to $T$	Real gas SRK EOS
Specific heat	2nd order polynomial fit to $T$	Ideal gas mixing
Thermal conductivity	Linear fit to $T$	Ideal gas mixing
Viscosity	Linear fit to $T$	Ideal gas mixing
Species diffusivity	-	Chapman-Enskog formula

Each of the formulas used for the models are described in Appendix A.

#### *Basic model*

This model was used for simulations involving flow and heat exchange, such as the ones presented in section 4.2. Its assumptions are the following:

- ◇ The fluid composition is homogeneous (no species diffusion).



- ◇ The changes in pressure due to hydrostatic pressure no larger than 10 Pa.
- ◇ Highest Mach number calculated was 10E-4, thus flow could be assumed as incompressible.
- ◇ Specific heat, thermal conductivity and viscosity values obtained from the CapeOpen database for the working temperature range and fitted to functions of temperature [25].

### Detailed model

This model was used for all simulations that had chemical reactions present, such as the ones presented in Sec. C.1 and onwards. The thermodynamic and transport properties of each species was obtained from the latest San Diego University’s Chemical-Kinetic Mechanisms for Combustion Applications (2016) [39].

Its assumptions are the following:

- ◇ Fluid is a single phase mixture of 5 molecules:  $H_2$ ,  $CO_2$ ,  $CO$ ,  $CH_3OH$ ,  $H_2O$ .
- ◇ Density can be determined from Soave-Redlich-Kwong equation of state for mixtures. Pressure and temperature dependent.
- ◇ Specific heat, thermal conductivity and viscosity for mixture are mass-averaged values for each of the species’ properties. Temperature dependent.
- ◇ Species transport diffusivity is set as a matrix of specie-to-specie binary diffusivities  $D_{ij}$ , using Chapman-Enskog formula.

A note on the Chapman-Enskog formula is that it only holds true for ideal gases. A higher accuracy could be achieved using  $D_{ij}$  coefficients following the work by Fuller et al. (1966), however it has been reported by Lommerts et al. (2000) that “for the modeling of methanol synthesis at current working pressure, they account for only *slight improvements* in the accuracy”.

## 2.4.2 Heat transfer coefficients

### 2.4.2.1 At walls

At the boundary between the fluid and solid domains, the heat transfer coefficient would be calculated by Fluent™ through **standard wall functions** following *law of the wall* correlations [38]. These set the exchange of heat between two cell volumes as a function of physical properties of the materials at a dimensionless boundary layer.

The values calculated and stored by Fluent™ for near-wall heat transfer **does not represent overall heat transfer coefficient**  $U$ . To find the equivalent values, these have to be back-calculated from the simulation results using the wall temperature, inlet and outlet stream temperatures, mass flow, area and surface heat flux.



Fig. 2.24. Diagram for calculating  $U$  for a fixed temperature wall.

Using Fig. 2.24 for reference, the overall heat transfer determined by Fluent™ is calculated through Eq. 2.46

$$U = \frac{q}{\Delta T_{LM}} \quad (2.46)$$

Where:

$q$  is the surface heat flux in units of  $W/m^2$ . A directly reportable value from Fluent.

$\Delta T_{LM}$  is the logarithmic mean temperature difference in K. Determined by sampling area average inlet and outlet temperatures of each zone from Fluent.

$$\Delta T_{LM} = \frac{(T_{in} - T_{hot}) - (T_{out} - T_{hot})}{\ln\left(\frac{T_{in} - T_{hot}}{T_{out} - T_{hot}}\right)}$$

### 2.4.2.2 Inside a packed bed

As the gas enters the catalyst bed, the fluid will exchange heat with the external surface of the pellets. The simplest model to implement would setting both catalyst pellets and the gas at the same temperature. This is called a bed in thermal equilibrium.

In reality, both gas and solid will be exchanging heat, creating a temperature gradient. This is a bed in non-thermal equilibrium. For a catalytic reactor with a short bed length, this approach is needed to find the ineffective length of reactor bed. This is the length of the bed that is at a temperature lower than required to trigger the reactions. Both cases are visualized in Fig. 2.25.

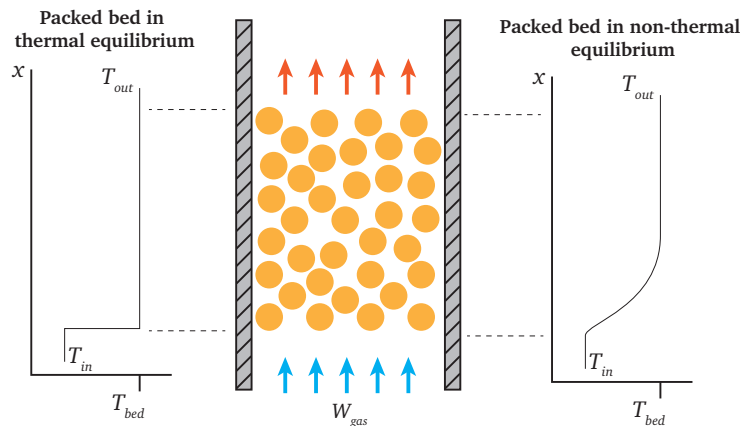


Fig. 2.25. Diagram comparing gas temperature profiles for packed bed in thermal equilibrium vs non-thermal equilibrium.

The work of Li and Finlayson (1977) reviews correlations between the packing of a solid particle bed and the gas flow moving through it. A generalized relation is described between an overall heat transfer coefficient  $U_p$  for a cylindrical packed bed with cylindrical solid particles. This is presented in Eq. 2.47.

$$\frac{U_p d_t}{\lambda} \exp\left(\frac{6d_p}{d_t}\right) = 1.26 \text{Re}_p^{0.95} \quad (2.47)$$

Where:

$d_t$  is the empty bed diameter in m.

$d_p$  is the catalyst particle diameter in m.

$\lambda$  is the fluid thermal conductivity in  $W/mK$ .

$\text{Re}_p$  is the Reynolds number of the gas flow around the particle, as:

$$\text{Re}_p = \frac{4Wd_p}{\pi D_o^2 \mu} \quad (2.48)$$

The correlation from Eq. 2.47 holds true for the conditions of:

$$\begin{aligned} 20 &\leq \text{Re}_p \leq 800 \\ 0.003 &\leq d_p/d_t \leq 0.3 \end{aligned}$$

In this research, the flow-rate  $W$  is not known before the calculation. Its value is approximated from the flow-rate on a similar packed bed in thermal equilibrium. This approximate  $W$  is used to determine the value of  $U_p$  used to solve the case for the bed in non-thermal equilibrium.

The area for the heat exchange of the gases and the packed bed is set as the ratio of pellet surface to volume of the packed bed, known as specific surface. Traditionally, this value is either measured or provided by the manufacturer. Neither of these methods were available for the research, instead the value used for this research was assumed to be  $300 \text{ m}^{-1}$ , based on similarly reported catalyst sized specific surfaces from [Sinnott and Towler \(2013\)](#).

### 2.4.3 Chemical reactions

Chemkin™, a chemistry and kinetics package to solve for species' transport and reactions can be implemented into Fluent™ 18.2. By default, Fluent's interface allows for the implementation of chemical reactions with form of an Arrhenius equation:  $\kappa = A \exp(B/RT)$ .

This work uses a GKM with rates in the form of a Langmuir-Hinshelwood model. These are not compatible with the user interface which requires a different approach to implement.

#### *Describing reaction rates through UDFs*

Chemkin™ as a stand-alone software can be used for solving GKM such as the one proposed in this research. Documentation for the software is scattered, and debugging tools are not available; this makes any software implementation process problematic. The approach taken was to use Fluent's back-end in the form of UDFs to pass reaction rate values to Chemkin™, so that the transport equation and fluid properties could be solved for the methanol synthesis.

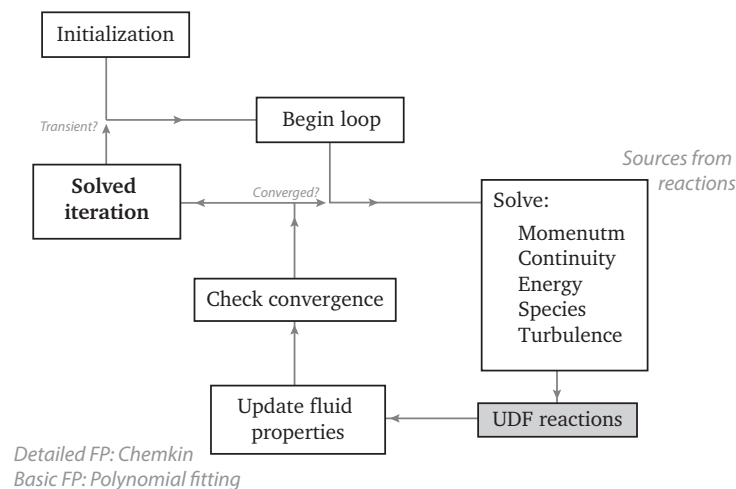


Fig. 2.26. Fluent™ solver diagram. Implementation of UDF reaction rates in the solver algorithm [38].

The calculation procedure taken in the present work is as follows:

1. Describe the components, reaction directions and arbitrary Arrhenius rates for Chemkin™ as .inp input files.
2. Import the San Diego thermodynamic and transport properties databases [39].
3. Create a user-defined function (UDF) for Fluent, so that the arbitrary rates are overwritten at every iteration for every cell volume by the lumped reaction rates (Eqs. 2.1 and 2.2). The UDF used is a DEFINE\_VR\_RATE, which does the following calculations:
  - Set the catalyst presence density in the cell volume.
  - Calculate adsorption  $K_{ai}$ , equilibrium  $K_{ei}$  and rate constants  $k_i$ .
  - Find partial pressures  $p_i$  from mass fractions  $\omega_i$ .
  - Determine surface activity  $\theta$  and reaction rates  $r_i$  from Eq. 2.10 and 2.11.
4. The reactions are defined to occur in a single volumetric zone of the simulations.
5. Chemkin™ is used to provide fluid properties  $\rho$ ,  $\lambda$ ,  $c_p$ ,  $\mu$ , species sources  $S_i$ , transport  $j_i$  and energy sources  $S_h$ .

The process of overwriting rates forces Fluent™ and Chemkin™ to **solve the chemistry explicitly**, meaning that at every cell, only the current composition of the cell will be used to determine the next composition at the following iteration. This is not an optimal solution, as it can lead to overshooting in the calculation of the reaction rates. This can only be compensated by having smaller time-steps which also mean higher computation time.

### Catalytic packed bed

A catalyst bed also creates a disturbance to the fluid, which needs to be accounted for, preferably without having to create complex meshing structures, as these demand additional computational time.

The reactions are defined to be occurring in a fixed volume zone, with no accountable changes to the catalyst activity or morphology. One parameter that has not been defined from Eq. 2.43 is the momentum source  $S_m$ , which takes the form of:

$$S_m = -\left(\mu \mathbb{D} \cdot \mathbf{u} + \frac{1}{2} \rho |\mathbf{u}| \mathbb{C} \cdot \mathbf{u}\right)$$

Fluent™ can account for such a momentum sink by implementing viscous  $\mathbb{D}$  and inertial  $\mathbb{C}$  resistance matrices. For a homogeneous packed bed, which could be described through Ergun's equation, only the values of the principal axes are needed to be set, in accordance to Eqs. 2.49 and 2.50 [38].

$$\mathbb{D}_{ii} = \left(\frac{D_p^2}{150} \frac{\varepsilon^3}{(1-\varepsilon)^2}\right)^{-1} \quad (2.49)$$

$$\mathbb{C}_{ii} = \frac{3.5(1-\varepsilon)}{D_p \varepsilon^3} \quad (2.50)$$

Where:

- $D_p$  is the mean particle diameter in m.<sup>ix</sup>
- $\varepsilon$  is the void fraction.

<sup>ix</sup>From Eq. 2.6, it is determined that the cylindrical pellets used have an sphericity of 1.0, meaning that their packing effect is equal to that of spherical pellets.

#### 2.4.4 Interpreting results from simulations

No single standard method to evaluate the certainty of numerical results exists in the academic CFD communities. There are various standards imposed by academic journals regarding the control of the reporting quality of CFD results.

The editorial policy of the Journal of Fluids Engineering establish a set of minimal criteria that any report should contain to address the numerical certainty of the simulation results [44]. The criteria considered in this research are the following:

1. Methods should be at least second order accurate in space.
2. Iterative convergence conditions have to be explicitly described.
3. Grid independence should be described.
4. Results should be compared to benchmark solutions reported in published literature or reliable experimental results.

From the previous list, first and second conditions are simulation settings used in every simulation performed in Fluent™. The third condition is addressed in Sec. 3.2 using the Richardson's extrapolation method to obtain a grid convergence index [44]. The source of data for the fourth condition is from the experimental characterization done by Basarkar on the reactor.

## Chapter 3

# Model setup

The goal of computer aided numerical simulations is to approximate natural systems through mathematical models based on the same system. The validity of results obtained from such calculations can represent real phenomena with satisfiable degree of accuracy. If direct experimental measurements verify the results of the simulations, then it can be said that the model is correct. If experimental measurements disprove the simulations (as is often the case) then it must mean that the model is incomplete and should be improved.

The SMBR is a small disassembleable pressurized vessel. Its size limits the space available to safely install measurement sensors. This leads to some parameters inside the reactor going unmeasured during operation, which reduces the certainty of accurately describing its performance. The most important values which are not directly measured are:

- ◇ Gas flow-rate
- ◇ Internal fluid temperature
- ◇ Condenser duty
- ◇ Pressure drop across the packed bed.

Multiple models were developed to account for all of these effects. The combination of all of the results provide insight of the combination of all effects in the reactor.

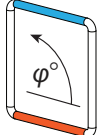
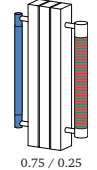
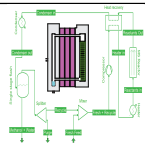
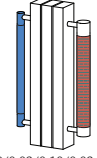
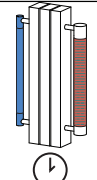
### 3.1 Model overview

- a) The first model of the current research aimed at bridging the literature gap regarding the flow-rate of a NCL with heating and cooling elements in vertical position at the same vertical centerline. This represents a loop with a tilt angle of  $\varphi = 90^\circ$  in the anti-clockwise direction, as this is the configuration of the SMBR. This was set up using a 3D CFD calculation for Fluent™ 18.2 [38].
- b) The second model represents the SMBR geometry with the effects of a packed bed as a porous medium and heat recovery by the aluminum blocks. Boundary conditions are set from the experimental working conditions gathered by Basarkar, using the initial gas composition of the reactor. This calculation is performed as a 3D CFD case using Fluent™ 18.2 [38].
- c) The third model is a 1D chemical process model developed in COCO™ simulator [25]. It is a mass and energy balance that accounts for the effects of condensation and feed replenishing within in the SMBR. Values of inlet, outlet streams, as well as working conditions from experimental work are fed into the process model.

- d) A fourth model is the replication of the second case, with a gas composition that differs from the feed-gas. This is performed to account for the change of the average composition from the initial feed gas.
- e) A final model implements the [Bussche and Froment GKM](#) into Fluent™ 18.2. The operating conditions of the simulation deviate from the experimental case. Without a multicomponent condensation model to separate the methanol and water from the system, the calculation represents a batch process reactor, and not a semi-continuous process. As no experiments were performed for the batch operation of the SMBR, no validation of the simulation results can be presented. The process of validating the CFD reaction model and the case developed for a natural circulation geometry are presented in [Appendix C](#).

The cases presented in this report follow the sequence from [Tab. 3.1](#). These will be addressed by their respective letters. The individual models implemented into each case are summarized in [Tab. 3.2](#).

**Tab. 3.1.** Chart for cases presented in current report

Diagram	Simulation	Boundary conditions	Results	Limitations
	a) Tilting uniform diameter NCL (3D CFD)	Nitrogen at 50 bar Wall temperature Gravity direction	Impact of $\varphi$ Mass flow Heat input	No experimental validation Limited literature
 0.75 / 0.25 H2 / CO2	b) SMBR with feed gas (3D CFD)	Feed gas at 50 bar Wall temperature Solid-fluid interface Packed bed	Mass flow Heat input Heat recovery	No condensation No heat of reaction No direct measurement of flow-rate for validation
	c) Chemical process model (1D)	Mass inlet Equipment Temperature Heat recovered	Condensed outlet Mass flow required	No effect of buoyancy No effect of packed bed
 0.80/0.03/0.10/0.03/0.04 H2 / CO / CO2 / H2O / CH3OH	d) SMBR with mixed gas (3D CFD)	Mixed gas at 50 bar Wall temperature Solid-fluid interface Packed bed	Mass flow Energy Heat recovery	No condensation No heat of reaction No direct measurement of flow-rate for validation
	e) SMBR with reactions (Transient 3D CFD)	Initial feed gas at 50 bar Wall temperature Solid-fluid interface Packed bed	Mass flow Energy Heat recovery Change of species Heat of reaction	No condensation No experimental validation

Tab. 3.2. Models used for each case

	a)	b)	c)	d)	e)
Simulation	3D CFD	3D CFD	1D	3D CFD	3D CFD + UDFs
Solution	Steady state	Steady state	Steady state	Steady state	Transient
Momentum	Buoyancy	Buoyancy	-	Buoyancy	Buoyancy
	-	Ergun	-	Ergun	Ergun
Turbulence	RNG $\kappa$ - $\epsilon$	RNG $\kappa$ - $\epsilon$	-	RNG $\kappa$ - $\epsilon$	RNG $\kappa$ - $\epsilon$
Energy	Std. wall functions	Std. wall functions	-	Std. wall functions	Std. wall functions
	-	Li and Finlayson [42]	-	-	-
Fluid properties	Poly-fit to $T$	Poly-fit to $T$	CapeOpen [25]	San Diego U. [39]	San Diego U. [39]
Species transport	Homogeneous	Homogeneous	Homogeneous	Chapman-Enskog	Chapman-Enskog
Reaction	-	-	Bussche & Froment	-	Bussche & Froment
Multiphase	-	-	Single-stage flash	-	-
EOS	-	-	Peng-Robinson	-	SRK

## 3.2 Sources of uncertainty

From information presented in Sec. 2.4.4, there are uncertainties associated to the usage of numerical simulations to represent a specific case. In the current section, an overview of the sources of error that may arise from the usage of the models presented is discussed.

Any of the aforementioned cases may contain any of the following sources of error:

- ◇ Meshing and grid convergence index.
- ◇ Boundary conditions and their methods for obtaining them.
- ◇ Special considerations, such as initialization methods or fluid properties.

### 3.2.1 Case a)

#### Meshing

For case (a), a large number of simulations were executed in a limited period of time. A compromise between grid refinement and accuracy was made, keeping in mind the errors that could arise from grid definition. Following the guidelines of Murphy et al. (2003), a procedure for estimation of discretization error was performed on a sample case with 3 different levels of grid refinement. Mesh information is presented in Fig. 3.1 and the results from testing the discretization error of a sample simulation error of heat input and flow-rate is summarized in Tab. 3.3.

Tab. 3.3. Data for sample simulation on NCL to obtain value for errors due to grid refinement. Data presented in Appendix B.1.2

	Number of cells	133000	245000	432000
	Solution iterations	1716	2445	2272
Mesh	Orthogonal Quality	0.977	0.983	0.986
	Representative cell size	2.71E-7	1.47E-7	8.36E-8
	Skewness	0.110	0.0969	0.097
Report	Heat input [W]	5.3387	5.2750	5.2471
	Flow-rate [kg/s]	1.400E-4	1.394E-4	1.388E-4

Tab. 3.4. Error and grid Independence for heat input and flow-rate from using a 245k mesh over the 432k

	Heat input	Flow-rate
Relative error	0.53%	0.42%
Approximation order	1.55	1.41
Grid Convergence Index	1.13%	0.96%



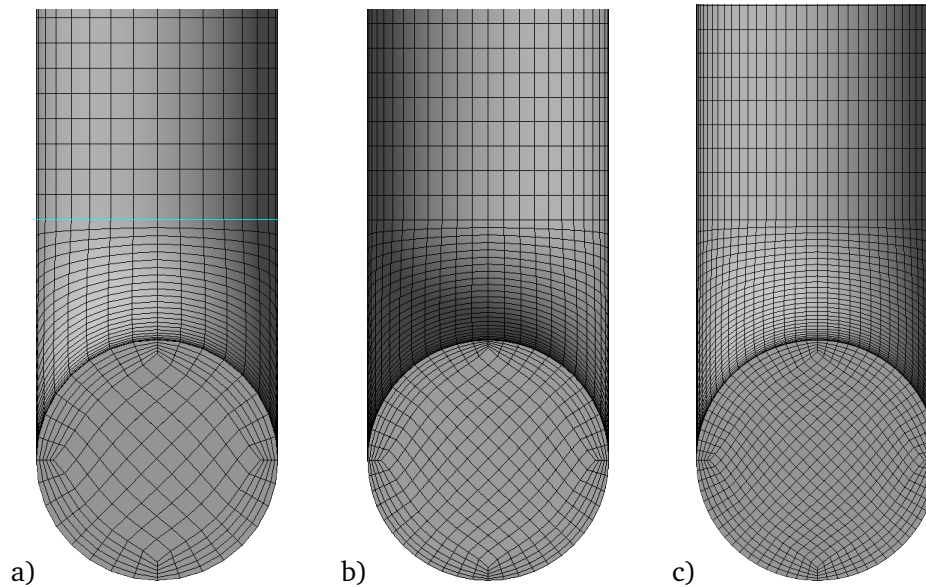


**Fig. 3.1.** Meshes of different refinement used for sample simulation to determine grid independence.

This error estimate reported in Tab. 3.4 is representative of the simulations reported in Sec. 4.1. This case study performs 30 simulations using the same geometry and temperature boundary conditions. Only this example is used for reference to establish the grid error, as all simulations are performed for a similar grid convergence index as in Sec. 4.1.

### 3.2.2 Case b), c) and d)

#### Boundary conditions

The temperatures used as boundary conditions in the hot and cold walls of the CFD models are based on the average temperature measured on by the thermocouples installed in the SMBR. In Fig. 3.2 a schematic drawing of the **positioning of the thermocouples** embedded into the aluminum blocks of the experimental setup.

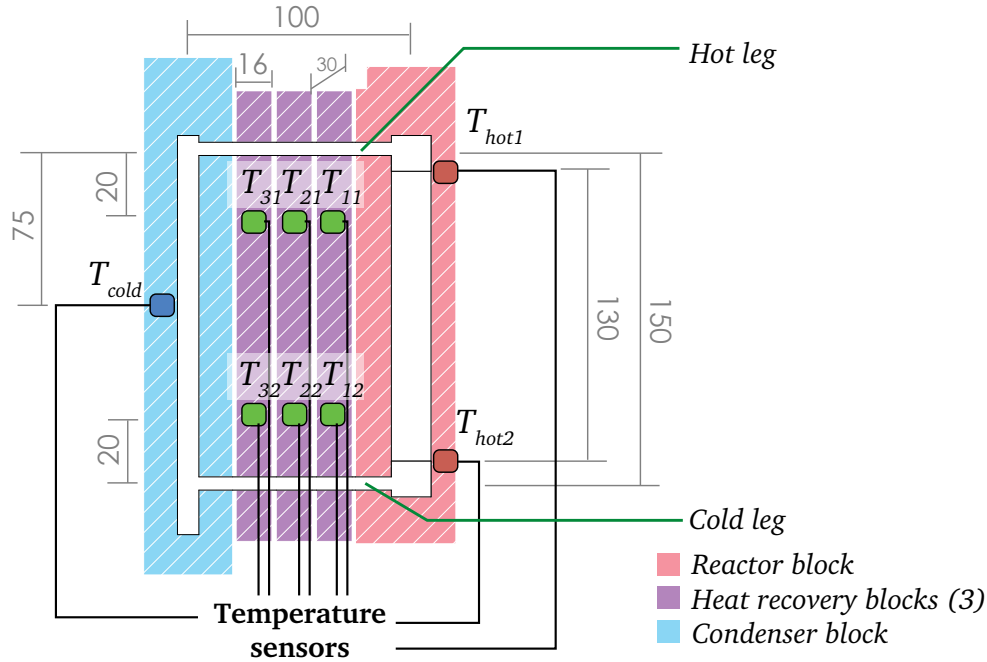


Fig. 3.2. Location of thermocouples in SMBR experimental setup. Units: mm.

The boundary conditions used for the hot and cold wall are determined as follows:

$$T_{\text{hot}} = \frac{T_{\text{hot1}} + T_{\text{hot2}}}{2} \quad (3.1)$$

$$T_{\text{cold}} = T_{\text{cold}} \quad (3.2)$$

The measured heat recovery from the aluminum blocks is determined from the thermal conduction between the top and temperatures of the blocks, as follows:

$$Q_{\text{blocks}} = \sum_{i=1}^3 \frac{230 \text{ W/mK} (0.016 \times 0.30) \text{ m}^2 (T_{i1} - T_{i2})}{0.09 \text{ m}} \quad (3.3)$$

No measurement tool for flow-rate was installed in the experimental setup; the value was estimated from the heat recovered. The temperature difference of the fluid along the length of the cold leg is assumed to be equal to the temperature difference between the bottom of the blocks. This **major assumption** makes the experimental value for flow-rate a **reference value**, and not used as a boundary condition.

$$W \approx \frac{Q_{\text{blocks}}}{c_p (T_{32} - T_{12})} \quad (3.4)$$

### 3.2.3 Case b) and d)

#### *Boundary conditions*

The issues with establishing the temperature boundary conditions for the equipment presented in Sec. 3.2.2 apply to the 3D CFD simulations.

Additionally, the numerical simulations **ignore all heat losses to the environment**. In the experimental characterization of the SMBR, heat losses have been estimated to be 50.27 W. These were calculated by measuring the temperatures of select elements of the reactor. The summary of the values is presented in Fig. 3.3.

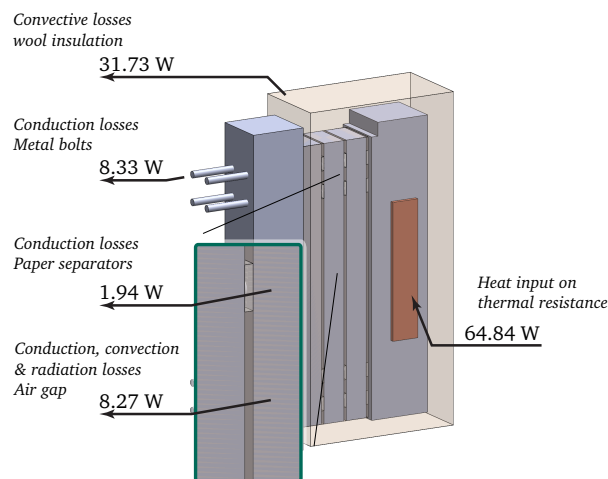


Fig. 3.3. Approximate estimation of heat losses in system, as reported by Basarkar (2018).

#### *Meshing*

Just like in Sec. 3.2.1, a grid independence analysis was made for a sample case from Sec. 4.2. The desired values to analyze are heat input, heat recovered and mass flow inside the loop. In Fig. 3.5 a comparison between a mesh of three levels of refinement is presented for the cases reported in Sec. 4.2.

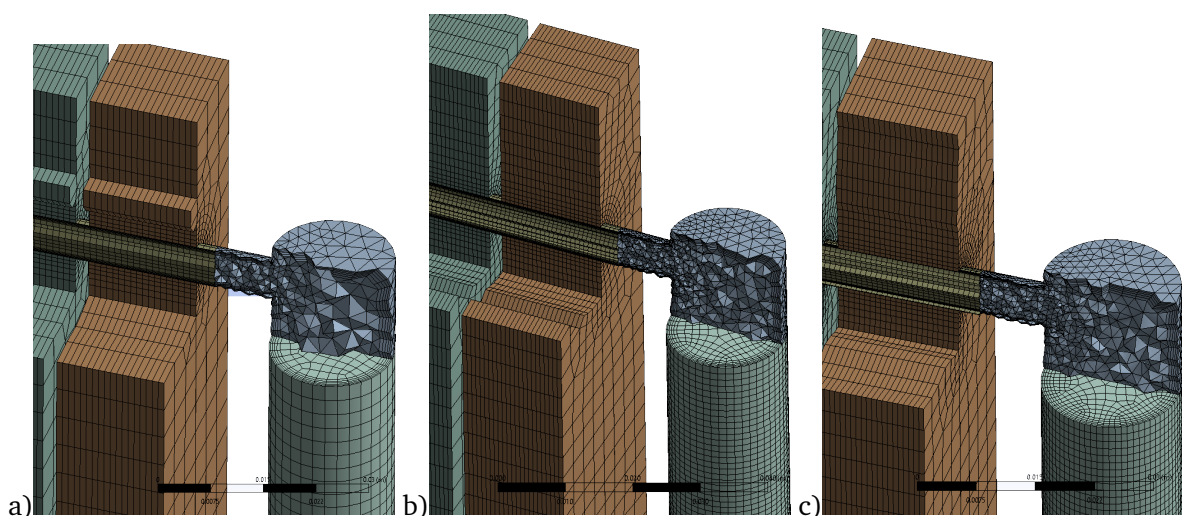


Fig. 3.4. Meshes of different refinement used for sample simulation to determine grid independence. a) 133k cells b) 343k cells c) 422k cells

**Tab. 3.5.** Data for sample simulation on SMBR to obtain value for errors due to grid refinement.

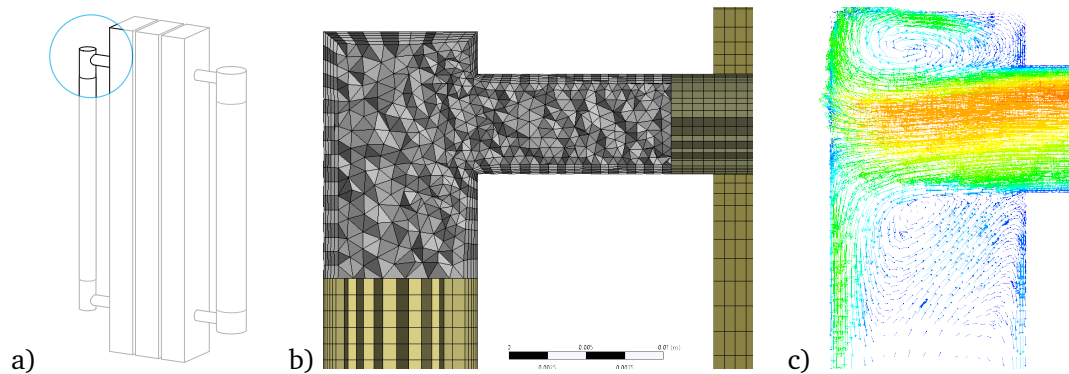
Mesh	Number of fluid cells	113901	291400	358700
	Representative cell size	3.41E-7	1.34E-7	1.09E-7
	Orthogonal Quality	0.9357	0.9371	0.9418
	Skewness	0.1635	0.1591	0.1452
Report	Heat input [W]	13.080	13.192	13.296
	Heat recovered [W]	9.927	9.875	9.798
	Flow-rate [kg/s]	5.388E-5	5.405E-5	5.411E-5

**Tab. 3.6.** Error and grid Independence for heat input and flow-rate from using a 245k mesh over the 432k

	Heat input	Heat recovered	Flow-rate
Relative error	0.78%	0.78%	0.10%
Approximation order	6.96	2.73	7.36
Grid Convergence Index	1.28%	2.25%	0.16%

### Special considerations

The SMBR mesh utilized uses a mixture of structured hexahedral volumes with unstructured tetrahedral volumes and inflation layers along the walls. The combination of cell structures is done on the channel expansions and contractions found on the corners of the loop. By applying a **local mesh refining** the effects of eddies occurring the loop are contained to reach a converged solution. Fig. 3.5 displays the mixed meshing on corners of the mesh.

**Fig. 3.5.** Unstructured meshing used for mesh refinement on corner expansion. Velocity vectors displaying two eddies on the corner. Obtained from simulation in Sec. 4.2

Approximating an **initial solution** reduces computation time. Good initialization is specially important for reaching convergence on natural convection systems, as they require low residuals in the energy equation ( $<1E-10$ ).

Two approaches were performed to generate an initial solution to aid calculation:

- ◇ Adding a small vertical initial velocity at the hot wall boundary no larger than 10% of steady-state velocity.
- ◇ Solving the flow for a reduced gravity field, and progressively increase it until reaching the desired  $g = 9.81 \text{ m/s}^2$ . This is an approach suggested in the Fluent™ manual [38] for solving convective flows with a Rayleigh number above  $10^{10}$ , as is the case in the MBR.

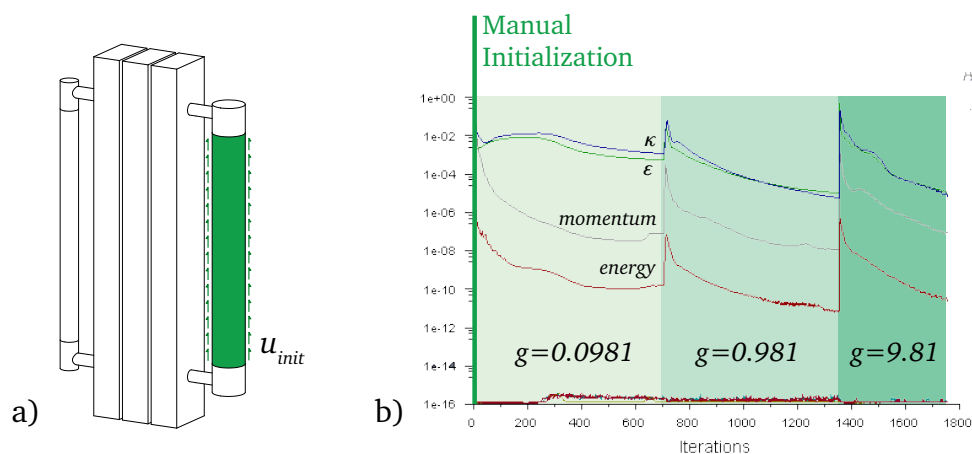


**Fig. 3.6.** Diagram of initialization conditions and process of reaching convergence for a steady-state natural circulation flow simulation with heat exchange. a) Manual initialization from the heating wall boundary condition; initial vertical velocity. b) Plotted residuals of momentum, energy and turbulence for reduced gravity fields to reach a converged solution.

In Sec. 4.2 an uncommon **visual representation of results** for temperature profiles is used.  $T$ - $x$  plots are employed to represent the temperature of the fluid inside the reactor at different locations. This depiction allows to convey the following information in a single image:

- ◇ Temperature of the fluid cells.
- ◇ Temperature of the first layer between the fluid and the solid cells.
- ◇ Temperature gradient in the  $x$  direction of the fluid cells in different locations of the loop.
- ◇ Inlet and outlet temperature of cooling and heating sections (hot and cold legs)

An example of this visualization is presented in Fig. 3.7. It compares colored temperature contours with a  $T$ - $x$  plot to show the information that can be packed within this data representation method.

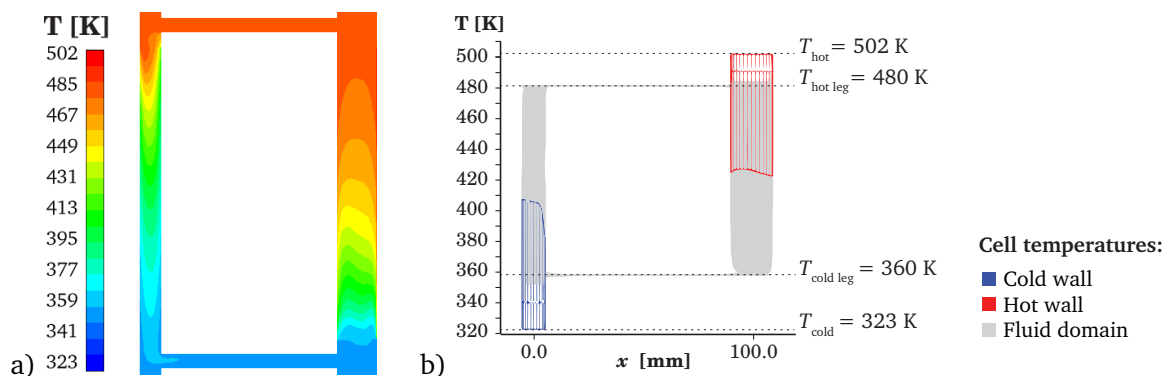


**Fig. 3.7.** Comparison of data representation for temperature of fluid inside of SMBR with feed gas at 50 bar;  $T_{\text{hot}} = 502\text{K}$ ,  $T_{\text{cold}} = 493\text{K}$ . a) Temperature contours. b)  $T$ - $x$  plot.

### 3.2.4 Case e)

The [Bussche and Froment](#) GKM for methanol synthesis was implemented into Fluent™. It was validated by comparing with other single pass reactor models reported in literature [9, 12]. It was implemented for the SMBR geometry with the goal of accounting for the effects of heat of reaction and change in gas composition in a transient behavior of the natural circulation reactor.

Without a condensation or separation model in the numerical model, the gas composition only changes according to the gas composition profile that reaches the equilibrium composition mentioned in Sec. 2.1.3.4. This is **not representative of the SMBR operation**, as the fresh feed that replenishes the reactor changes the conversion profile.

This simulation serves as a **showcase of an incomplete model** that could be expanded to describe the SMBR performance by implementing a condensation / species separation model.

#### *Boundary conditions*

The values selected for boundary conditions were based on a combination of data sources which were thought at the time to be representative of the SMBR.

Temperatures were selected based on the experimental conditions that were being tested by [Basarkar](#) during the characterization of the reactor. These are not the optimal operation values. The values for catalyst packing and void fraction were based on the values from the model by [Bussche and Froment](#),

#### *Special considerations*

To analyze the results from this transient simulation, an average flow-rate of the circulating flow-rate was considered and input into a 1D plug flow reactor with a length equivalent  $L_{eq}$  to the residence time of gases inside the loop  $t_{loop}$ . A simple diagram of this concept is presented in Fig. 3.8.

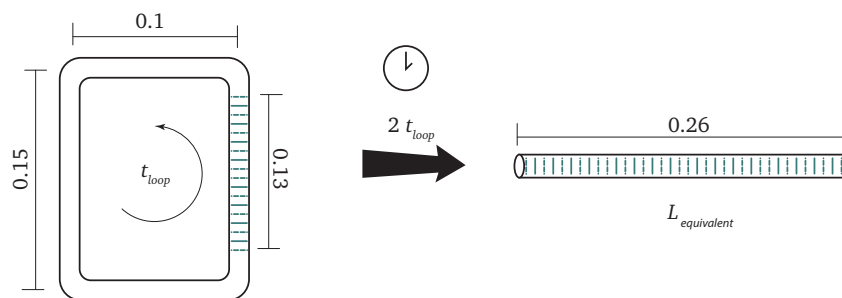


**Fig. 3.8.** Conceptual drawing. Equivalent length plug flow reactor for a residence time twice that of the time the gases take to flow around the circulation loop.

For example, if the mass of the gases in the loop reactor were 1.02 g, and the flow-rate 0.118 g/s,  $t_{loop}$  would be equal to 8.47 s. A transient simulation that lasts 17 seconds would represent a plug flow reactor of equivalent length to **twice the reactor length of the SMBR**, not the length of the loop.



## Chapter 4

# Modeling results and discussion

Each section of this chapter presents the simulation cases summarized in Tab. 3.1. At the beginning of each section, a list of general configurations for each case is presented.

From Section 4.1 to 4.5, a set of cases are presented. Their general format is as follows:

- ◇ Geometry and Mesh: A 3D CAD drawing and a showcase of the mesh used to simulate each case.
- ◇ Boundary conditions: A set of values imposed on the simulation(s) for each case.
- ◇ Results: Summaries of the outcome of the calculations.
- ◇ Observations: A highlight of notable details observed from results.

In Sec. 4.6, a summary of the most descriptive results from every model is presented to represent the measurements from the experimental characterization of the SMBR.

In Sec. 4.7 an analysis that summarizes the combination of the effects of each phenomena in the SMBR is presented. A path to improving the operation of the natural circulation reactor is highlighted.

### 4.1 Tilting of uniform diameter loop

The CFD simulation presented in this section uses a geometry that represents the length, height and average hydraulic diameter of the **fluid domain of the original MBR** (See Fig. 2.4). It uses Nitrogen at 50 bar as a working fluid, as this inert gas was used for other flow experiments during the characterization of the reactor [3].

#### 4.1.1 Geometry and Mesh

The circulation loop is of uniform diameter (UDL). A structured mesh with inflation layers along the walls is used to represent the geometry of the UDL. This is presented in Fig. 4.1.

#### 4.1.2 Boundary conditions

In Fig. 4.2, a visual representation of the boundary conditions used in this case is presented. A range of six values for  $\Delta T$  between the hot and cold wall boundaries are set, for five angles of inclination  $\varphi$  in the anti-clockwise direction.



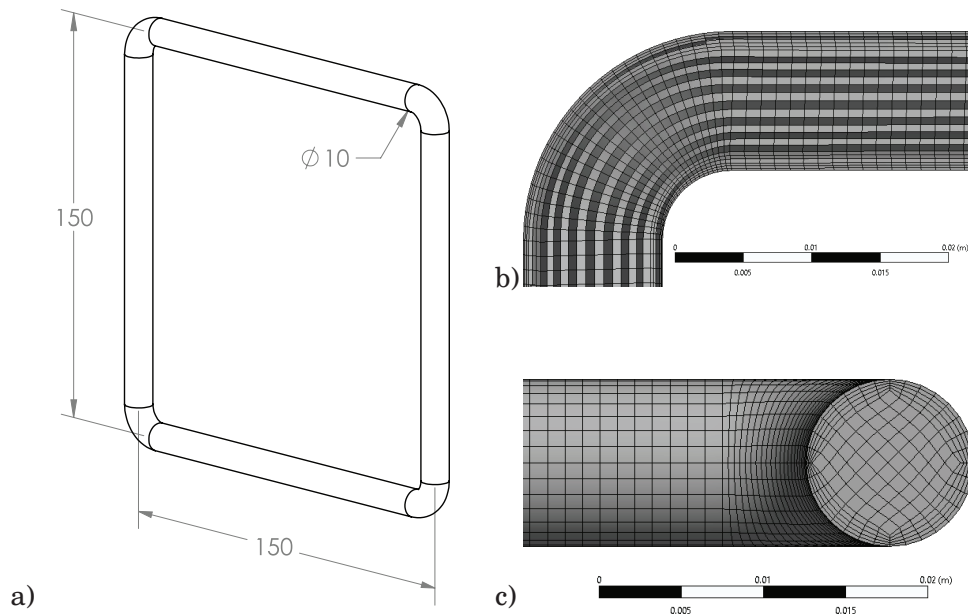
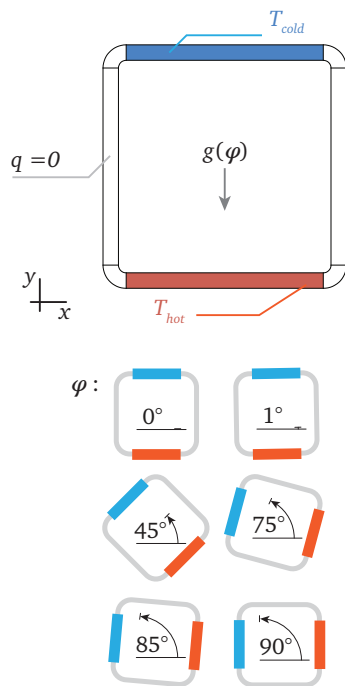


**Fig. 4.1.** UDL used for first case. **a)** 3D CAD diagram. Units:mm **b)** Cross-section of 230k cell structured mesh around the corner. **c)** Cross-section of mesh on straight circular portion. Average mesh skewness: 0.0969 . Average mesh orthogonal quality: 0.983



◇ Fluid domain: Nitrogen at 50 bar  
Basic FP

◇ No heat flux through legs.

◇ Temperature boundary conditions:

$\Delta T$	$T_{hot}$	$T_{cold}$
5	415 K	410 K
10	420 K	410 K
20	425 K	405 K
50	450 K	400 K
100	465 K	365 K
200	515 K	315 K

◇ Gravity vector components:

$\varphi$	$g_x$	$g_y$
1°	9.8085059	-0.1712081
45°	6.936718	-6.936718
75°	2.5390148	-9.4757324
85°	0.8549998	-9.77267
90°	0.0	-9.81

**Fig. 4.2.** Boundary conditions diagram for tilting of UDL

### 4.1.3 Results

A comparison is made between selected cases in Tab. 4.1. From two  $\Delta T$  and five tilting angles, results are presented for the steady-state flow-rate, Reynolds number, energy input and average fluid temperature along the legs of the loop. Data for these simulations is reported in Appendix B.1.

**Tab. 4.1.** Values for flow-rate, heat input and average temperature of hot and cold legs of NCL for selected tilting angles. Two temperature difference ranges are presented:  $\Delta T = 10$  and 100.

Case	Value	1°	45°	75°	85°	90°	Unit
$T_{\text{hot}}=420$ K $T_{\text{cold}}=410$ K	Flow-rate	2.07	1.83	1.31	1.01	0.68	$\times 10^{-4}$ kg/s
	Reynolds N.	1614	1427	1022	790	529	
	Energy input	0.418	0.358	0.259	0.208	0.171	W
	Hot leg temperature	416	416	416	416	416	K
	Cold leg temperature	414	414	414	414	414	K
$T_{\text{hot}}=465$ K $T_{\text{cold}}=365$ K	Flow-rate	6.47	5.44	3.29	2.10	1.39	$\times 10^{-4}$ kg/s
	Reynolds N.	5031	4326	2563	1635	1455	
	Energy input	11.8	9.7	6.8	5.7	5.27	W
	Hot leg temperature	422	422	423	426	431	K
	Cold leg temperature	406	405	404	401	397	K

For both  $\Delta T$  cases, flow-rate and energy input reduce by increasing of the tilting angle. Both of these values reduce at a similar rate, as  $\varphi$  increases. For the case of  $\Delta T = 100$  K, the temperature difference between the hot and cold legs increases, as  $\varphi$  increases. If heat were to be recovered between gas traveling in the legs, a larger temperature difference between them favors heat conduction [45].

Another notable result, is that all the Reynolds number on the case of  $\Delta T = 10$  lie in the laminar to transition regime for NCL reported by [Swapnalee and Vijayan \(2011\)](#)<sup>i</sup>. This does not apply to the cases of  $\Delta T = 100$ , as the values range between the transition and turbulent regime. This behavior can be observed in the temperature contours presented in Fig. 4.3.

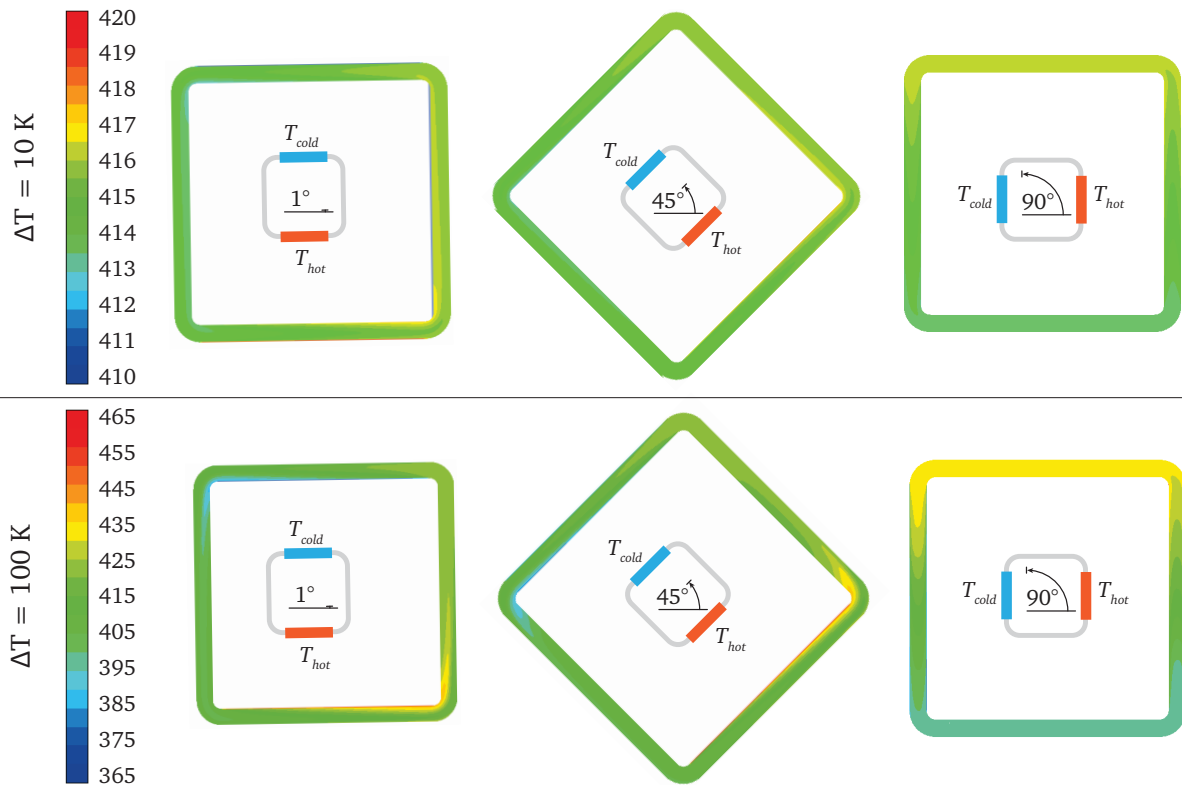


**Fig. 4.3.** Temperature contours for selected tilting angles, and  $\Delta T$  between wall temperature boundary conditions. **Flow direction in counter-clockwise direction.**

<sup>i</sup>The flow regimes for natural circulation loops: Laminar ( $Re_D < 898$ ), transition ( $898 < Re_D < 3196$ ), turbulent ( $Re_D > 3196$ )

In Fig. 4.3, the temperature contours of the gas are presented for three tilting angles. In the case for  $\varphi = 1^\circ$ , a stratification of fluid is visible in along the heating and cooling portions of the loop. As the fluid reaches the corners, a sharper temperature gradient is visible for the case of the larger  $\Delta T$ . This is representative of the fluid regime difference based on Reynolds number presented in Tab. 4.1. These cases vary between a transition and turbulent regime for the  $\Delta T = 10$  and  $\Delta T = 100$ , respectively.

For the cases of  $\varphi = 90^\circ$ , the temperature contours in Fig. 4.3 show a parabolic temperature gradient along the length of the heating and cooling portions of the loop. No sharp temperature gradients are visible in this angled configuration, representative of the lower Reynolds numbers presented in Tab. 4.1. These cases vary between a laminar and transition regime for the  $\Delta T = 10$  and  $\Delta T = 100$ , respectively.

Furthermore, the results are summarized in both log-log and Cartesian plots correlating the Reynolds number and the modified Grashoff number, following the work from Vijayan. This is presented in Fig. 4.4.

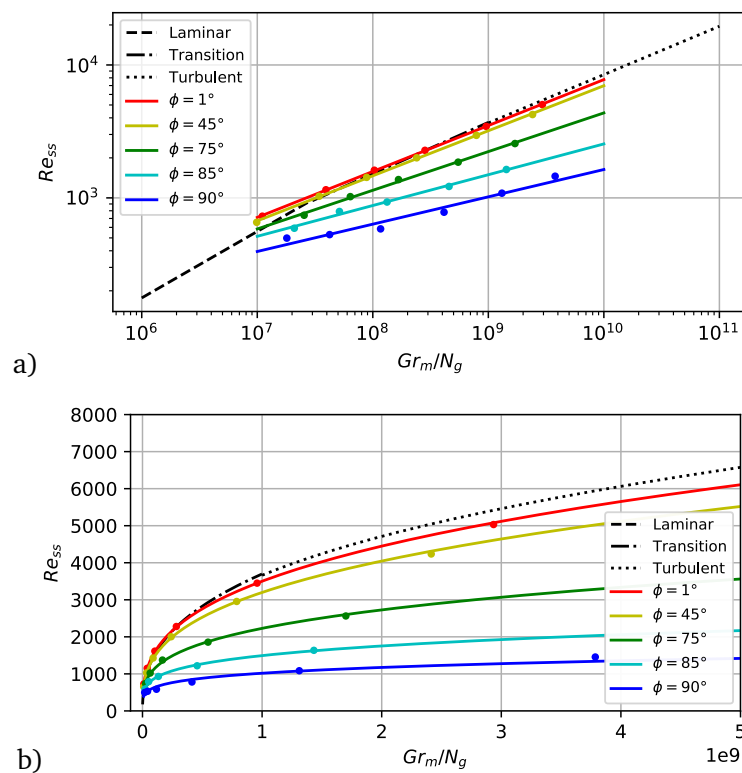


Fig. 4.4. Comparison between numerical simulations and correlations by Swapnalee and Vijayan. a) Log-log plot, b) Linear plot.

The log-log plot is used to compare with the original reported values by Swapnalee and Vijayan (Fig. 2.18a), while the Cartesian representation is comparable with the only study available that links flow-rate and energy input into a tilted NCL, reported by Basu et al. (2013) (Fig. 2.19). Note that for a fixed loop geometry and fluid composition, the X axis scales with energy input, and the Y axis with flow-rate.

#### 4.1.4 Observations

- ◇ Regressions were performed to fit the data into an equation with the form of Eq. 2.40 for each tilting angle. The values obtained for  $C$  and  $r$  coefficients for

each angle are presented in Tab. 4.2. These are an extension to the correlation by Vijayan for a rectangular uniform diameter loop, following the methodology of other simulation work [30, 35].

Tab. 4.2. Fitted coefficients of  $C$  and  $r$  for Eq. 2.40 for different tilting angles.

$\varphi$	$C$	$r$
1°	2.71715	0.34556
45°	2.85379	0.33884
75°	5.35937	0.29101
85°	12.2804	0.23167
90°	14.3814	0.20556

- ◇ The results qualitatively resemble the information reported by Basu et al. (2013). The observation made from Fig. 2.19 that a logarithmic behavior would be observed by tilting into a vertical position has been confirmed in the results presented in Fig. 4.4b.
- ◇ The observations reported by Krishnani and Basu (2017) stated that for their tilting angles between 15-45° the flow-rate reduced by a factor approximate to  $\cos \varphi$ , this is attributed to a reduction of the buoyant force. An increase in the temperature difference between the legs was also reported as  $\varphi$  increased.
- ◇ Based on the temperatures of the legs presented in Tab. 4.1 a **vertical orientation of the loop is more suitable for recovering heat** between the legs, as opposed to the horizontal heater and cooler configuration.
- ◇ In practical terms, Fig. 4.4 shows that **flow-rate and energy transferred through the loop are correlated** for vertical natural circulation loops; this was only established for horizontal natural circulation loops. The reduction of the slope of  $Re$  vs  $Gr_m$  observed indicates that the the ratio at which these values scale is affected by the tilting angle of the circulation loop.
- ◇ Experimental studies are required to confirm the information presented from this case. The SMBR is unable to make comparable experiments, as **the cold and hot leg channels are integrated into the heat recovery blocks**, and no flow-rate measuring tool was installed in the system.

## 4.2 Simulations of gas flow and temperature in SMBR

CFD simulations for a single-phase gas composition are performed using the information provided from experiments as boundary conditions, namely the wall temperatures of heating and cooling blocks and the solid catalyst packing information.

This case combines the effects of heat recovery blocks and a packed bed inside the SMBR. The feed gas composition of  $H_2$  and  $CO_2$  at a 0.75/0.25 mole ratio is used.

### 4.2.1 Geometry and Mesh

The geometry utilized to model the SMBR is limited to represent the fluid domain and the heat recovery aluminum blocks of the experimental setup (See dimensions in Fig. 2.5). Removing the metal blocks of the reactor and condenser blocks was done to reduce computation time and to set the temperatures measured in the experimental setup as boundary conditions on the external surface of the fluid.

The mesh utilized is a combination of structured cells on the cylindrical portions of the fluid domain, and unstructured cells for the corner portions of the loop. Inflation layers along all external wall boundaries are placed for the fluid cells in contact to a stationary boundary, ie. along the external surface of the fluid domain, and the internal contact area of the solid blocks.

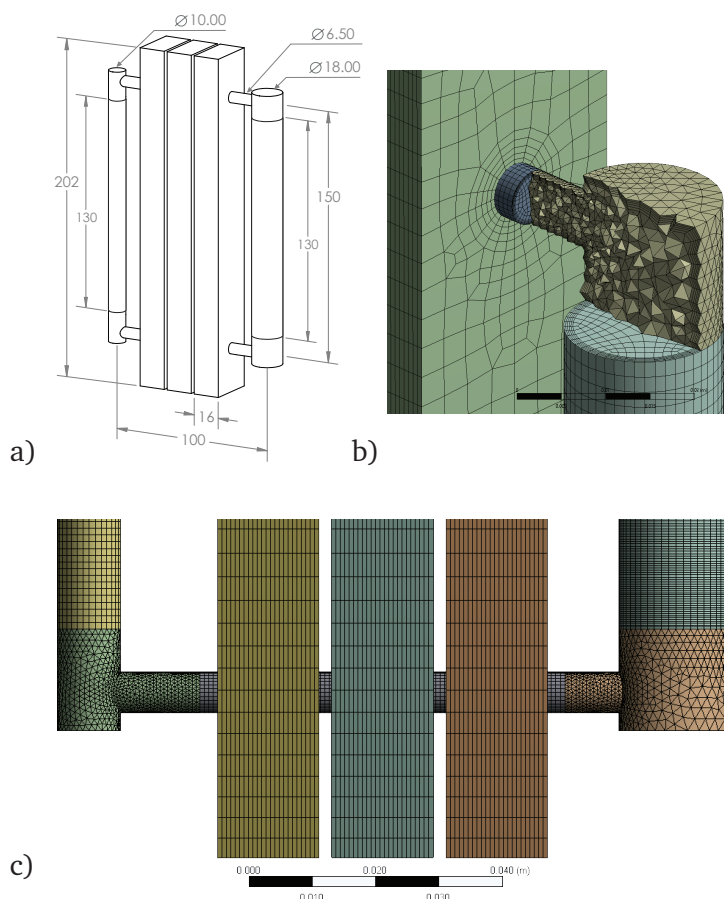


**Fig. 4.5.** Geometry and 343k cell mesh of SMBR reactor. a) Diagram with dimensions. b) Cross-section of mesh at the heater outlet. c) View of mesh on bottom portion. Average mesh skewness: 0.1635. Average mesh orthogonality: 0.9357

### 4.2.2 Boundary conditions

The boundary conditions selected were based on the information provided from the temperature sensors of the SMBR (see Fig. 3.2). As the cold block is exposed to the ambient temperature, it was assumed that the entire external cylindrical surface will be at the same temperature as the temperature measured in the center of the condenser block.

The porous media representing the catalyst packed bed is assumed to have the physical properties of thermal conductivity and specific heat as copper ( $\rho = 8978 \text{ kg/m}^3$ ,  $c_p = 381 \text{ J/kgK}$ ,  $\lambda = 387.6 \text{ W/mK}$ ). This was selected, as the exact composition of the copper-zinc oxide-alumina catalyst is undisclosed by the manufacturer. The outermost layer of the pellets is primarily composed of copper, hence the physical properties of copper were selected.

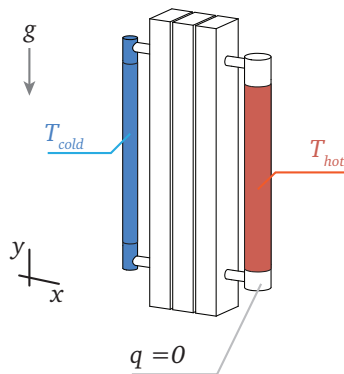


Fig. 4.6. Diagram of boundary conditions for reactor.

- ◇ Temperature boundary conditions:
  - $T_{\text{hot}} = 501.15 \text{ K}$
  - $T_{\text{cold}} = 338.15 \text{ K}$
- ◇ Fluid: Feed gas at 50 bar
  - $\text{H}_2/\text{CO}_2$  as 0.75/0.25 ratio
  - Basic FP
- ◇ Solid domain: Aluminum
- ◇ Porous media: Copper
  - Particle diameter  $D_p = 0.005 \text{ m}$
  - $\varepsilon = [0.288, 0.3, 0.4, 0.5]$ .
  - $D_{ii}$  from Eq. 2.49
  - $C_{ii}$  from Eq. 2.50
  - $Re_p$  from Eq. 2.48<sup>ii</sup>.
  - $U_p$  from Eq. 2.47.
  - Specific area of  $300 \text{ m}^{-1}$ .

A range of different void fractions  $\varepsilon$  were selected to represent the catalyst packed bed. The range of 0.5 to 0.288 is selected, as this value is the reported range between the experimental measurements by Bussche and Froment (1996) and Chen et al. (2011). Both of which also used the Bussche and Froment GKM to describe a catalytic methanol synthesis reactor. Coincidentally, the reported value for the void fraction of the experimental setup was also 0.288.

The specific area for heat exchange of the catalyst packed was assumed to be  $300 \text{ m}^{-1}$  based on similarly reported catalyst sized specific surfaces from Sinnott and Towler (2013). The influence of the catalyst on the SMBR is summarized in Tab. 4.3.

Tab. 4.3. Influence of catalyst as a porous medium on momentum and energy equations for different void fraction values for particle diameter of 5 mm.

$\varepsilon$	$D_{ii}$ [ $\text{m}^{-2}$ ]	$C_{ii}$ [ $\text{m}^{-1}$ ]	$Re_p$ [-]	$U_{\text{int}}$ [ $\text{W m}^{-2}\text{K}$ ]
0.5	1.2E7	2.8E3	132.86	182.81
0.4	3.375E7	6.562E3	97.23	135.89
0.3	1.089E8	1.815E4	57.76	82.85
0.288	1.273E8	2.086E4	55.44	79.69

<sup>ii</sup>Calculated from a first approximation of flow-rate for a packed bed in thermal equilibrium

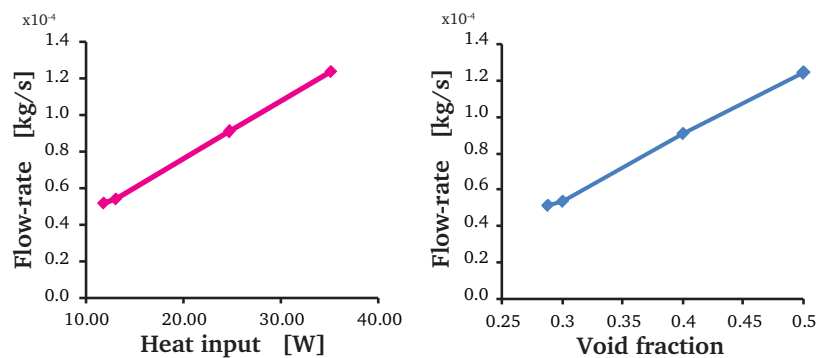
### 4.2.3 Results

In Tab. 4.4, a comparison of the values for steady-state mass flow, heat input and heat recovered by the aluminum blocks is presented. It is observed that with the reduction of the catalyst packing (ie. the increment of  $\varepsilon$ ) the flow-rate in the loop increases.

**Tab. 4.4.** Comparing results of void fraction, flow-rate, energy input and energy recovered in heat recovery blocks.

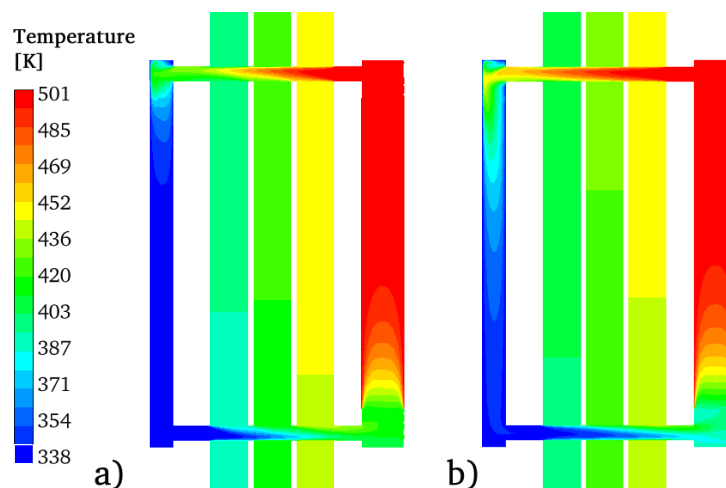
Void fraction $\varepsilon$	0.288	0.3	0.4	0.5	Unit
Flow-rate	5.17E-5	5.39E-5	9.07E-5	1.24E-4	kg/s
Heat input	11.78	13.08	24.74	35.07	W
Heat recovered	10.49	10.93	13.30	15.64	W

The observation from Sec. 4.1 that heat input and flow-rate are correlated still holds true for a natural circulation loop with flow blockage. In Fig. 4.7, these relations are plotted against each-other, displaying a quasi-linear behavior.



**Fig. 4.7.** Relation between void fraction and mass flow for the information presented in Tab. 4.4.

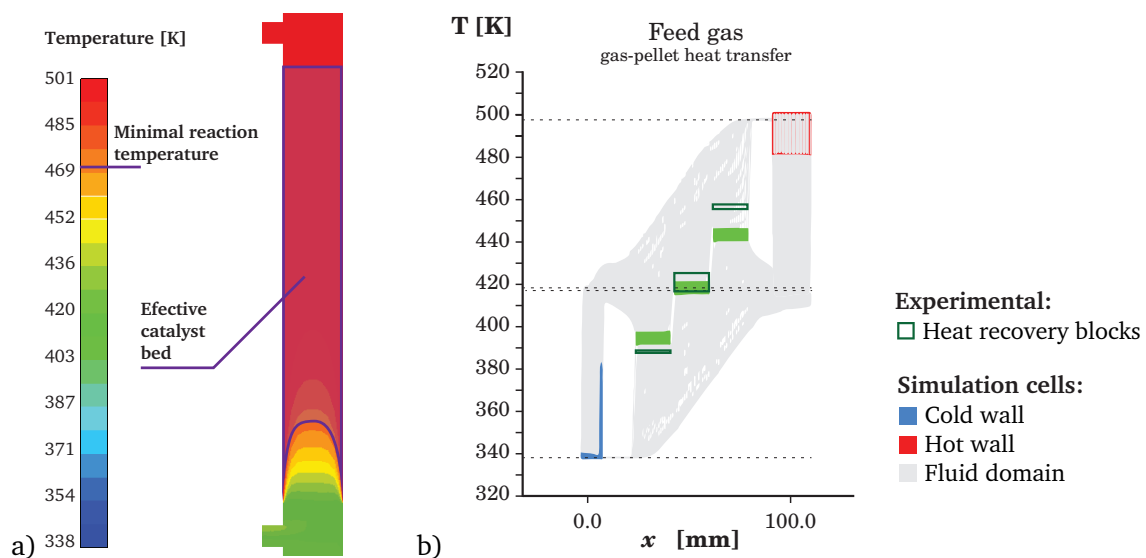
To explain the increase of the heat recovered with the reduction in catalyst packing, Fig. 4.8 displays a comparison of the temperature contours between the void fraction of 0.288 and 0.5. It is visible that the fluid temperature at the hot legs (horizontal channels at the top of the loop) is higher for the case of  $\varepsilon = 0.5$ , than for  $\varepsilon = 0.288$ . In the cold legs, a lower temperature is distinguished for the case of  $\varepsilon = 0.5$  compared with the case of  $\varepsilon = 0.288$ . This larger temperature difference between the legs is attributed to the higher heat recovered through the aluminum blocks.



**Fig. 4.8.** Temperature contours for simulations. a)  $\varepsilon = 0.288$  b)  $\varepsilon = 0.5$ .

The relation of catalyst packing and heat recovery does increase, but relation is not directly linked. The ratio of heat recovered to heat input decreases with the reduction of catalyst packing, based on the values presented in Tab. 4.4.

For the experimental operation conditions of the SMBR ( $\varepsilon = 0.288$ ), Fig. 4.9 provides crucial information for the **reactor performance**. In Fig. 4.9a it is observed that a portion of the bed near the inlet is at a temperature lower than 470 K, the minimal temperature observed to trigger reactions [7]. This represents **15% of the volume of the catalytic bed that is ineffective** for methanol synthesis (2 centimeters of the packed bed). Fig. 4.9b displays the estimated temperature inlets and of the gases into the condenser and reactor blocks; for the feed gas composition, these are determined to be 417 and 420 K, respectively.



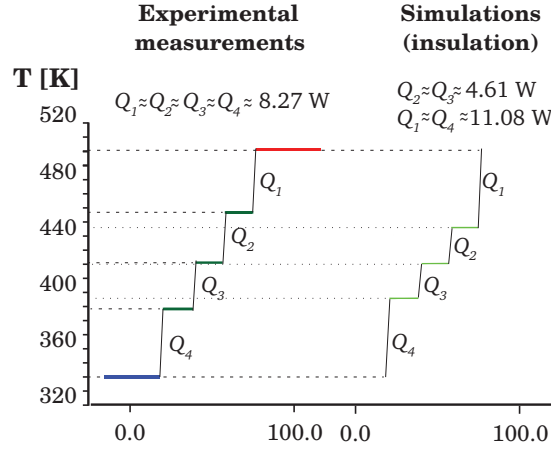
**Fig. 4.9.** Heat transfer with packing surface for operating conditions of SMBR. a) Internal temperature contours in packed bed. b)  $T$ - $x$  plot for SMBR reactor. Comparison between numerical simulation and experimental measurements in heat recovery blocks.

Fig. 4.9b also provides a comparison between the temperature measurements of the heat recovery blocks (*dark green*) and the values for temperature calculated of the aluminum cells (*light green*) is displayed in a  $T$ - $X$  plot. The deviation between these values is attributed to the no heat-flux boundary condition set between the metal blocks (See Fig. 4.10)

#### 4.2.4 Observations

- ◇ The ineffective bed length observed in Fig. 4.9a lead the experimental setup from Basarkar to move the location of the heating pads (observed in Fig. 2.6b) to a location closer to the inlet of the catalyst bed. The measured temperature difference between the top and bottom sensor reduced from 9 K before the change to 3 K [3].
- ◇ All external surfaces of the solid volumes were set to have no heat flux; this represents a perfect insulation between each block. This neglects any heat transfer that can occur from radiation and convection in the air gap formed between each metal block. The deviation caused by this idealization is addressed in Figs. 3.3 and 4.10.





**Fig. 4.10.** Approximate heat exchange in the **air gap** for the measured temperatures of the metal blocks. Compared with the 3D CFD simulations with perfect insulation between each block; a less uniform temperature gradient on the axial direction is observed.

- ◇ Flow-rate appears to scale linearly with the void fraction. This can be explained by scaling the steady-state momentum equation from Eq. 2.34 adding Ergun's equation as a function of friction factors from Eq. 2.7, as Eq. 4.1.

$$g\rho\beta \oint T dz = \frac{W^2}{\rho A^2} \left( \frac{f_{loop} L_{loop}}{D} + \frac{f_{bed} L_{bed} (1-\varepsilon)}{D_p \varepsilon^3} \right) \quad (4.1)$$

$$f_{loop} = \frac{64A\mu}{WD}; \quad f_{bed} = \frac{150A\mu(1-\varepsilon)}{WD_p} + 1.75$$

As the geometric configuration and temperatures of the loop remains the same, the buoyant forces should stay equal for all cases (left hand term). This can be used to scale flow-rate  $W$  from Eq. 4.1.

$$\frac{\rho A^2}{W^2} \sim \left( \frac{64A\mu L_{loop}}{WD^2} + \frac{150A\mu L_{bed}(1-\varepsilon)^2}{WD_p^2 \varepsilon^3} + \frac{1.75 L_{bed}(1-\varepsilon)}{D_p \varepsilon^3} \right) \quad (4.2)$$

With the values of the **highest void fraction**:

$D = 0.011 \text{ m}$	$A = 9.50\text{E-}5 \text{ m}^2$
$D_p = 0.005 \text{ m}$	$\mu = 1.8\text{E-}5 \text{ m}^2$
$\varepsilon = 0.5 \text{ m}$	$L_{loop} = 0.50 \text{ m}$
$W = 1.24\text{E-}4 \text{ kg/s}$	$L_{bed} = 0.14 \text{ m}$

The significance of each term can be evaluated, as:

$$\frac{\rho A^2}{W^2} \sim \left( \underbrace{\frac{64A\mu L_{loop}}{WD_{loop}^2}}_{3.6} + \underbrace{\frac{150A\mu L_{bed}(1-\varepsilon)^2}{WD_p^2 \varepsilon^3}}_{23.1} + \underbrace{\frac{1.75 L_{bed}(1-\varepsilon)}{D_p \varepsilon^3}}_{196.7} \right)$$

Considering only the third term of the right hand side of Eq. 4.2, we find that flow-rate should scale as Eq. 4.3.

$$W \sim \sqrt{\frac{D_p \varepsilon^3}{L_{bed}(1-\varepsilon)}} \quad (4.3)$$

For **smaller values of void fraction**  $\varepsilon$ , the second term from Eq. 4.2 becomes more significant. By only considering it, flow-rate should scale as Eq. 4.4.

$$W \sim \frac{D_p \varepsilon^3}{L_{bed}(1-\varepsilon)^2} \quad (4.4)$$

- ◇ The scaling of flow-rate with void fraction should follow a trend of  $y = \frac{x^3}{(1-x)^2}$  for low values of  $\varepsilon$  and  $y = \sqrt{\frac{x^3}{1-x}}$  for values close to  $\varepsilon = 0.5$ . These functions are plotted in Fig. 4.11; A combination of both behaviors is observed for the void fraction range of 0.25 to 0.5

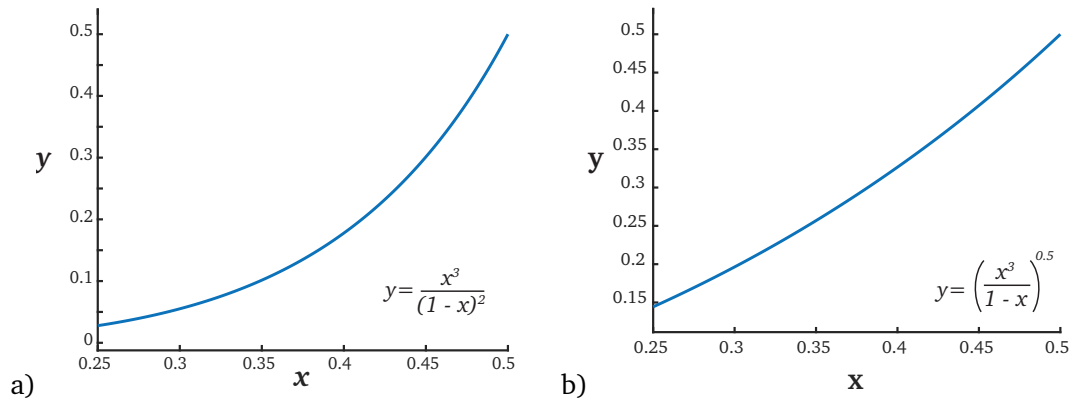


Fig. 4.11. Function representing the scaling of  $W$  to  $\varepsilon$

- ◇ In practice, void fraction is not a value commonly modified from the packed bed. This makes **reducing the length of the bed or increasing the particle diameter** the options to increase the flow-rate inside the loop, proportional to Eq. 4.5, maintaining the same geometry and temperature boundary conditions.

$$\underbrace{W \sim \frac{D_p}{L_{bed}}}_{\text{low } \varepsilon} ; \quad \underbrace{W \sim \sqrt{\frac{D_p}{L_{bed}}}}_{\text{high } \varepsilon} \quad (4.5)$$

### 4.3 SMBR chemical process model

Using the COCO™ simulator, a 1D steady-state chemical process model was developed, that would integrate every element of the SMBR as *operation units*. The developed chemical process model and a color coded diagram for each unit is presented in Fig. 4.12.

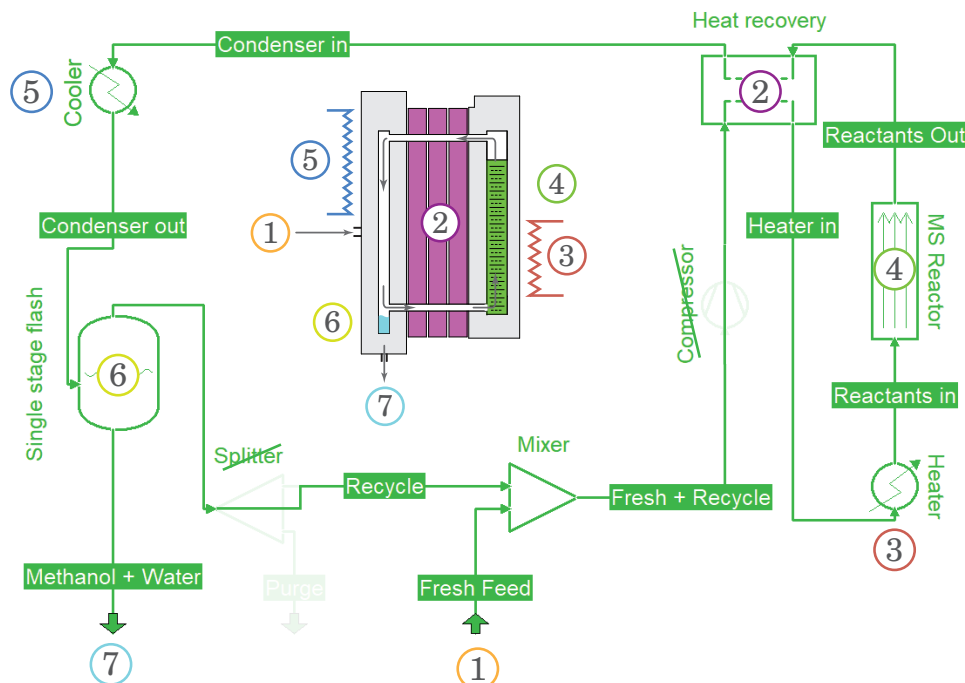


Fig. 4.12. Steady state chemical process model for SMBR. COCO™ process units display each equivalent element of the SMBR system. The influence of *compressor* and *splitter* units is negligible.

#### 4.3.1 Boundary conditions

The functionality of each stream and operational unit is as follows:

- ◇ Fresh feed: Is the feed gas composition ( $H_2/CO_2$  at 0.75/0.25 mol%) required to maintain the reactor pressure at 50 bar. Value set from experimental mass balance from Basarkar.
- ◇ Mixer: An adiabatic mixing unit that combines the unreacted gas and fresh feed.
- ◇ Compressor: This unit ensures that a pressure of 50 bar is maintained in the system. Its power consumption is five orders of magnitude lower than any other energy stream in the system, making its effect negligible.
- ◇ Heat recovery: These are the heat recovery blocks from SMBR. Value of the heat recovered from experimental measurements [3].
- ◇ Heater: A unit that adds heat to the gas stream. Boundary condition set to reach the reactor inlet temperature of 501.15 K (228°C) from experimental set point.
- ◇ Reactor: An isothermal packed bed reactor with the Bussche and Froment GKM validated in Appendix C.1.1.1. Temperature set from experimental conditions. Length of 0.12 m<sup>iii</sup>, diameter of 0.018 m, working temperature of 501.15 K, catalyst loading: 1263.775 kg/m<sup>3</sup>.
- ◇ Cooler: A unit that removes heat from the gas stream. Outlet is a two-phase

<sup>iii</sup>Based on the ineffective length of the reactor bed observed in Sec. 4.2

stream. Boundary condition set to gas stream temperature outlet from Sec. 4.2. of 340 K.

- ◇ Single stage flash: An isobaric flash unit that separates the two-phase stream into gas and liquid streams.
- ◇ Methanol + water: The liquid stream outlet of the single stage flash. Contains the methanol extracted from the SMBR.
- ◇ Recycled gas: The gas stream outlet from the single stage flash. Contains the unreacted components that will circulate back into the catalytic reactor.
- ◇ Splitter and Purge: A unit and stream added to reach a converged solution on a closed loop chemical process. Effects are negligible, as purged gas stream is three orders of magnitude lower than recycled gas.

There are eight values of interest in this chemical process model. By **setting the first four with values reported from experimental measurements**, with the only exception being the cooler outlet temperature, obtained from numerical simulations of Sec. 4.2. The final four (e-h) are determined from the chemical process model.

- a) Fresh feed mass flow in kg/s (1)
- b) Heat recovered from blocks in W (2)
- c) Heater outlet / inlet temperature in K (3).
- d) Cooler outlet / inlet temperature in K (5).
- e) Heater energy demand in W (3).
- f) Cooler energy demand in W (5).
- g) Production rate of (liquid) methanol in  $\text{g}_{\text{CH}_3\text{OH}}/\text{hr}$  (7).
- h) Flow-rate passing through system in kg/s (1+6, 2, 3, 4, 5).

### 4.3.2 Results

The values obtained from the 1D COCO™ model are compared with the result from the 3D CFD model presented in Sec. 4.2 for the case of  $\varepsilon = 0.288$  (single phase, no reactions) and with the information provided from experimental measurements in Tab. 4.5.

**Tab. 4.5.** Comparison of values from COCO™ process model, experimental measurements from Basarkar and the single phase gas flow simulations from Sec. 4.2. \*:Estimation from indirect measurement; not used for fitting.

	Value	Experiment	COCO™ (1D two-phase)	Fluent™ (3D single-phase)	Unit
Set points	a) Fresh feed flow	4.34E-06	4.34E-06		kg/s
	b) Heat recovered	11.1	11.1	10.49	W
	c) Heater outlet temperature	501	501	501	K
	d) Cooler outlet temperature	335 <sup>iv</sup>	340.0	341	K
Results	c) Heater inlet temperature		428	420	K
	d) Cooler inlet temperature		409	417	K
	e) Heater input heat		9.06	11.78	W
	f) Cooler heat released	14.57	14.66	11.78	W
	g) Methanol production	9.74	9.74		g/hr
	h) Flow-rate through loop	4.61E-5 <sup>v</sup>	3.06E-05	5.17E-05	kg/s

From the resulting values presented in Tab. 4.5, flow-rate has the highest amount of uncertainty between all reported values. By looking at the gas composition inside the loop, presented in Tab. 4.6,

<sup>iv</sup>Indirect measurement

<sup>v</sup>Estimation based on indirect measurements

the mixture observed has a higher molar fraction of H<sub>2</sub> and smaller of CO<sub>2</sub> than the feed gas used in Sec. 4.2. The fluid properties from these gas compositions vary drastically, as presented in Tab. 4.7.

**Tab. 4.6.** Gas composition on the hot and cold legs of SMBR. compared to equilibrium composition from current reactor inlet at  $p=50$  bar and  $T_{eq}=501.15$  K.

	Reactor inlet	Reactor outlet	Unit
H <sub>2</sub>	0.83414	0.80457	mol/mol
CO	0.02416	0.02528	mol/mol
CO <sub>2</sub>	0.11585	0.09877	mol/mol
H <sub>2</sub> O	0.00544	0.02789	mol/mol
CH <sub>3</sub> OH	0.02041	0.04347	mol/mol
$T_{dew}$	346.69	383.95	K

**Tab. 4.7.** Fluid properties for diverse gas compositions at 50 bar and 415 K. Data obtained from COCO™ simulator [25]

	Reactor inlet	Reactor outlet	Feed gas	Unit
MW	7.91	8.26	12.5	g/mol
$\rho$	11.36	11.95	18.12	kg/m <sup>3</sup>
$c_p$	3995	3900	2652	J/kgK
$\lambda$	0.201	0.195	0.181	W/mK
$\mu$	1.63E-5	1.64E-5	1.81E-5	Pa·s

From Tab. 4.7, it is observed that the simulations reported from Sec. 4.2 do not represent a gas composition that is going to be circling the SMBR during steady-state operation. Due to the higher H<sub>2</sub> concentration in these mixed gas compositions, its density is 1.5 times smaller and its specific heat 1.4 times higher than the feed gas composition previously considered in Sec. 4.2.

### 4.3.3 Observations

- ◇ The 1D two-phase chemical process model has much closer resemblance to the experimental setup from Basarkar than the 3D CFD single-phase flow model.
- ◇ Biggest discrepancies between experimental and COCO™ model **are mass flow and cooler outlet temperature**. These are values which are not directly measured.
- ◇ According to the gas composition from Tab. 4.6:
  - Based on the inlet composition, and following the calculation process described in Sec. 2.1.3.4, the equilibrium composition from the ‘Reactor inlet’ gas composition at the pressure of 50 bar and 501.15 K is presented in Tab. 4.8. It is clear that the ‘Reactor outlet’ gas composition has not reached equilibrium.

**Tab. 4.8.** Gas composition on the hot and cold legs of SMBR. compared to equilibrium composition from current reactor inlet at  $p=50$  bar and  $T_{eq}=501.15$  K.

	Equilibrium from inlet	Unit
H <sub>2</sub>	0.77075	mol/mol
CO	0.01112	mol/mol
CO <sub>2</sub>	0.08601	mol/mol
H <sub>2</sub> O	0.04972	mol/mol
CH <sub>3</sub> OH	0.08239	mol/mol
$T_{dew}$	403.63	K

– Water and methanol are present in the recirculation stream that goes into the reactor bed. This means that the condenser has not removed them completely from the stream.

– Inlet CO mole fraction is within the range where the [Bussche and Froment GKM](#) is experimentally valid. Deviations occur in the CO range of 4-15% [19].

– The steady-state operation gas composition in the SMBR from Tab. 4.6, and their fluid properties **differs greatly from the feed gas** used in Sec. 4.2.

- ◇ Cooler outlet is a two-phase stream. Heat removed can be estimated from a combination of sensible and latent heat of the condensed products, as mentioned in Eq. 4.6-4.8.

$$Q_{sens(5)} = W_{(5)}c_p(T_{in} - T_{out}) \quad (4.6)$$

$$= 3.27E-5 \text{ kg/s} (3784.26 \text{ J/kgK}) (411.9 - 349.15) = 7.76W$$

$$Q_{latH_2O(7)} = W_{(7)}\omega_{H_2O}\Delta H_{latH_2O} \quad (4.7)$$

$$= 4.286E-6 \text{ kg/s} (0.356)(2.257E6 \text{ J/kg}) = 3.43W$$

$$Q_{latCH_3OH(7)} = W_{(7)}\omega_{CH_3OH}\Delta H_{latCH_3OH} \quad (4.8)$$

$$= 4.286E-6 \text{ kg/s} (0.631)(1.085E6 \text{ J/kg}) = 2.92W$$

- ◇ The heat of reaction from the steady-state operation of the SMBR can be obtained from the change of CO and CH<sub>3</sub>OH at inlet and outlet of the catalytic reactor. Using the heat of reaction from Eq. 2.1 and 2.2, the energy generated inside the SMBR is calculated as given in Eqs. 4.9 and 4.10.

$$Q_{r(MEOH)} = W_{(4)} \frac{(\omega_{inCH_3OH} - \omega_{outCH_3OH})}{MW_{CH_3OH}} (-49200 \text{ J/mol}) \quad (4.9)$$

$$= (3.27E-5 \text{ kg/s}) \frac{(0.0796 - 0.1625)}{0.032 \text{ kg/mol}} (-49200) = -4.16 \text{ W}$$

$$Q_{r(RWGS)} = W_{(4)} \frac{(\omega_{inCO} - \omega_{outCO})}{MW_{CO}} (41600 \text{ J/mol}) \quad (4.10)$$

$$= (3.27E-5 \text{ kg/s}) \frac{(0.0824 - 0.0826)}{0.028 \text{ kg/mol}} (41600) = 9.72E-3 \text{ W}$$

## 4.4 Simulation of SMBR with mixed gas composition

Using the same mesh from Sec. 4.2, a 3D CFD simulation is performed **using the mixed gas compositions** obtained from the steady-state chemical process model from COCO™, presented in Tab. 4.6. The goal is to determine if the uncertainty of the value of flow-rate reported in Tab. 4.5 is due to the difference in gas composition between the feed gas (presented in Sec. 4.2), and the mixed gas composition.

The **geometry and mesh** are equal to the model presented in Fig. 4.5.

### 4.4.1 Boundary conditions

Similarly to the model presented in Sec. 4.2, the boundary conditions are set with fixed temperatures on the hot and cold fluid walls from Fig. 4.13, with no heat losses between blocks or the legs of the circulation loop.

The gas compositions used are defined based on their multicomponent mixture, using the detailed FP model based on San Diego University's thermodynamic and transport database [39]. A limitation of using such model is that the porous zone representing the catalyst packed bed is **in thermal equilibrium**, meaning that the solid-gas heat exchange on the catalyst bed is not going to be determined in this simulation.

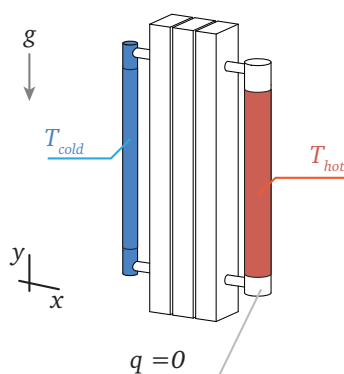


Fig. 4.13. Diagram of boundary conditions for reactor.

- ◇ Temperature boundary conditions:

$$T_{\text{hot}} = 501.15 \text{ K}$$

$$T_{\text{cold}} = 338.15 \text{ K}$$

- ◇ Fluid domain: **Mixed gas** at 50 bar

Detailed FP

Mole fractions:

	Reactor compositions	
	Inlet	Outlet
H <sub>2</sub>	0.83414	0.80457
CO	0.02416	0.02528
CO <sub>2</sub>	0.11585	0.09877
H <sub>2</sub> O	0.00544	0.02789
CH <sub>3</sub> OH	0.02041	0.04347

- ◇ Solid domain: Aluminum
- ◇ Porous media in thermal equilibrium
  - Particle diameter  $D_p = 0.005 \text{ m}$
  - Void fraction  $\varepsilon$  of 0.288<sup>vi</sup>
  - $D_{ii} = 1.273\text{E}8 \text{ m}^{-2}$ <sup>vii</sup>
  - $C_{ii} = 2.086\text{E}4 \text{ m}^{-1}$ <sup>viii</sup>

### 4.4.2 Results

In Tab. 4.9, the results obtained from this section are compared with the chemical process model and the experimental measurements. It is observed that the flow-rate determined for the mixed gas composition in the SMBR based on the calculation of buoyancy forces and momentum loss due to

<sup>vi</sup>From experimental conditions

<sup>vii</sup>See Tab. 4.3

<sup>viii</sup>See Tab. 4.3

the packed bed is in close agreement with the flow-rate that would be required from an energy and mass balance from the chemical process model which matches the experimental measurements.

**Tab. 4.9.** Comparison of values from corrected Fluent™ single-phase flow model with heat recovery and isothermal packed bed with COCO™ process model and experimental measurements from Basarkar.

Value	Fluent™ (3D single-phase)		COCO™ (1D two-phase)	Experiment	Unit
	Inlet composition	Outlet composition			
Fresh feed flow			4.34E-6	4.34E-06	kg/s
Heat recovered	8.73	8.91	11.1	11.1	W
Heater inlet temperature	425	422	427.7		K
Heater outlet temperature	501	501	501	501	K
Cooler outlet temperature	340	340	340	335 <sup>ix</sup>	K
Cooler inlet temperature	419	417	409		K
Heater input heat	9.18	9.80	8.79		W
Cooler heat released	9.18	9.80	14.66	14.57	W
Methanol production			9.74	9.74	g/hr
Flow-rate through loop	2.86E-5	3.06E-5	3.06E-5	4.61E-5 <sup>x</sup>	kg/s

The largest deviations between the models and the experimental measurements are the values which are not directly measured, but approximated (See Sec. 3.2.2), namely mass flow and gas temperature outlet from the condenser block.

Other smaller deviations between the CFD results and the chemical process model are attributed to unaccounted energies in the single-phase CFD model, namely the exothermic heat of reaction at the reactor block and the latent heat of condensation for water and methanol at the cooling block.

In Fig. 4.14, temperature contours for the SMBR with the mixed gas composition are presented; note that the porous zone representing the catalytic reactor is in thermal equilibrium with the gases, creating a sharp temperature jump, as it was mentioned in Fig. 2.25.

Comparing Fig. 4.14a from the current section to Fig. 4.8a from a previous section, minimal changes on the gas temperature contours are observed in the gas temperature of the legs or cooling portion of the loop. This means that the change of composition has a **small impact on the temperature profile of the gases, but it affects the mass flow and the energy required to drive it.**

Fig. 4.14b displays the volume of the condenser block that is at a temperature lower than 384 K. This is the dew point temperature for the reactor outlet composition reported in Tab. 4.6. Though no study has been done on the heat and mass transfer limitations of the SMBR, with 92% of the volume of the gases in the condenser block being at a temperature lower than the dew point temperature of the mixture, it suggests that internally, the condenser block should not be limited at separating the methanol and water from the mixed gas.

<sup>ix</sup>Indirect measurement

<sup>x</sup>Estimation based on indirect measurements



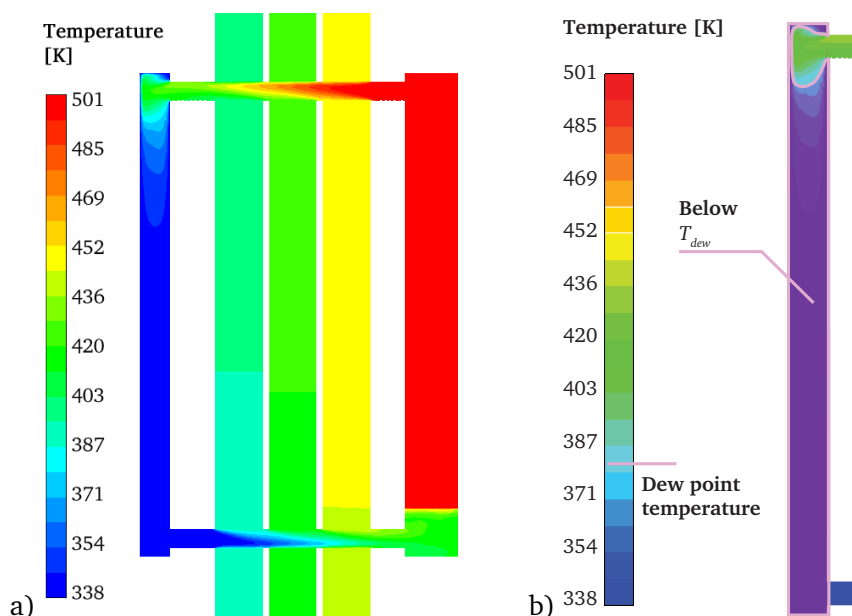


Fig. 4.14. Temperature contours of 3D CFD simulation. Isothermal packed bed.

## 4.5 Implementation of Bussche and Froment GKM into Fluent

The [Bussche and Froment](#) kinetic model was implemented as a means to account for the effects of the change in gas composition of the reactor and the energy of reaction released inside the loop.

The reaction rate model was included in the CFD simulations to describe the SMBR as a single-phase batch process natural circulation reactor. The case presented is an idealization with no experimental validation, but could be used as a **starting point for future modeling research** of the MBR.

This is a transient simulation, meaning that the gas composition inside of the reactor changes over time. The results reported are with sampling done every second for a duration of 116 seconds.

The code used and the cases used to validate its implementation are presented in [Appendix C](#)

The **geometry and mesh** are equal to the model presented in [Fig. 4.5](#).

### 4.5.1 Boundary conditions

Similarly to the model presented in [Sec. 4.2](#), the boundary conditions are set with fixed temperatures on the hot and cold fluid walls from [Fig. 4.13](#), with no heat losses between blocks or the legs of the circulation loop.

The detailed fluid properties model is used to account for the change in values due to the change of gas composition during the transient simulation. The usage of this model limits the catalyst zone to be in thermal equilibrium.

The reactor boundary conditions were based on values given during the process of experimental characterization of the SMBR. These are not representative of the optimal operation conditions reported by [Basarkar](#).

The packed bed catalyst density given in kg of catalyst per volume of reactor bed. It is taken from the model by [Bussche and Froment](#).

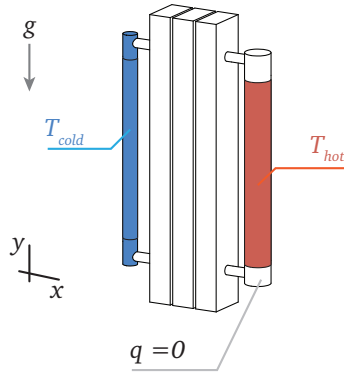


Fig. 4.15. Diagram of boundary conditions for reactor.

- ◇ Temperature boundary conditions:
  - $T_{\text{hot}} = 500 \text{ K}$
  - $T_{\text{cold}} = 320 \text{ K}$
- ◇ Initial fluid: Feed gas at 50 bar  
 $\text{H}_2/\text{CO}_2$  as 0.75/0.25 ratio  
 Detailed FP
- ◇ Solid domain: Aluminum
- ◇ Porous media in thermal equilibrium  
 Void fraction  $\varepsilon$  of 0.5.  
 $\text{D}_{ii} = 1.2\text{E}7 \text{ m}^{-2}$   
 $\text{C}_{ii} = 2.8\text{E}3 \text{ m}^{-1}$
- ◇ Packed bed catalyst density:  
 $\rho_{\text{cat}} = 887.5 \text{ kg/m}^3$

## 4.5.2 Results

Results of Fig. 4.16a, present the volume average mole fraction of reaction products inside the SMBR geometry over time. These are overlapped by the mole fraction profiles of a 1D plug flow reactor of similar dimensions and average flow-rate, with an equivalent length to the time of 116 seconds of simulation time.

The specific values for the equivalent length is determined in Eq. 4.11

$$\begin{aligned}
 m_{\text{gas}} &= 1.02 \text{ gr} \\
 L_{\text{packed bed}} &= 0.130 \text{ m} \\
 W_{\text{avg}} &= 1.178\text{E-}4 \text{ kg/s} \\
 t_{\text{loop}} &= \frac{m_{\text{gas}}}{W_{\text{avg}}} = 8.66 \text{ s} \\
 L_{\text{eq}} &= L_{\text{packed bed}} \frac{t_{\text{simulation}}}{t_{\text{loop}}} = 1.74 \text{ m}
 \end{aligned} \tag{4.11}$$

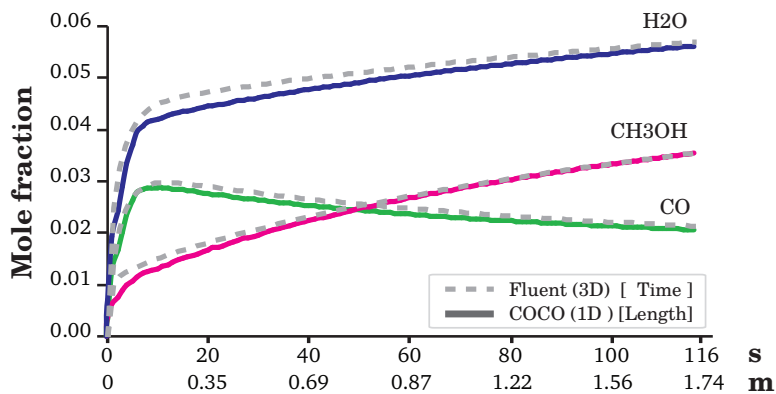


Fig. 4.16. Comparing profiles of species concentration between a transient CFD reaction simulation with 1D PFR model for average mass flow and equivalent length.

## 4.5.3 Observations

- ◇ The case reported in this section does not represent the operation of the MBR.
- ◇ From Fig. 4.16 it is visible that the rate of methanol production reduces over time. This makes **batch operation less effective the longer it runs**.
- ◇ At the 116 seconds, 0.086 grams of  $\text{CH}_3\text{OH}$  have been produced inside the reactor. At the reported rate, reaching equilibrium would take 48 minutes and only produce a total of 0.153 g of  $\text{CH}_3\text{OH}$ . See Fig. 4.17.

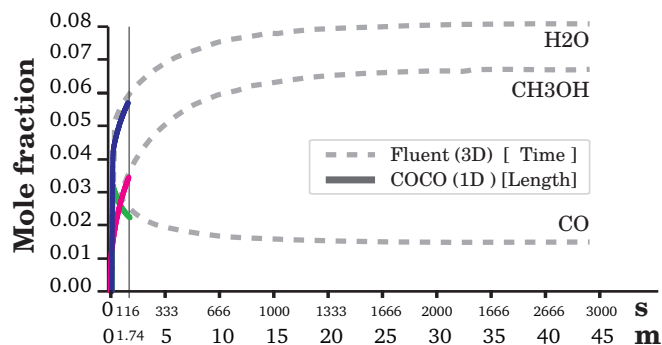


Fig. 4.17. Extending reactor length until equilibrium composition is achieved. Overlapping the reported values from Fluent™ with a plug flow reactor in COCO™.

- ◇ The implementation of the [Bussche and Froment GKM](#) been successful when comparing to cases from literature in [Appendix C.1.1.2](#) and [C.1.2](#).
- ◇ The solution of chemical composition is done explicitly, making the calculation sensitive to time-step size. To maintain a stable simulation, a maximum stable Courant number of 0.6 has been observed to be the limit of simulation stability.
- ◇ Mesh refining at the reactor inlet was necessary to account for the sharp species concentration and reaction rate gradients that occur in the catalytic reactors, as evidenced in [Figs. C.2, C.6, C.9](#). This increases computation demand.

## 4.6 Summary of results

Based on a combination of the experimental measurements presented in Tab. 4.5, and the models presented in Tab. 4.9, the behavior of the SMBR at steady-state is presented in Fig. 4.18. The composition of each stream is summarized in Tab. 4.10, with an uncertainty interval determined from standard deviation of each value reported from each model or experimental measurement. Details of each energy term is reported in Tab. 4.11 with their respective uncertainty interval from standard deviation.

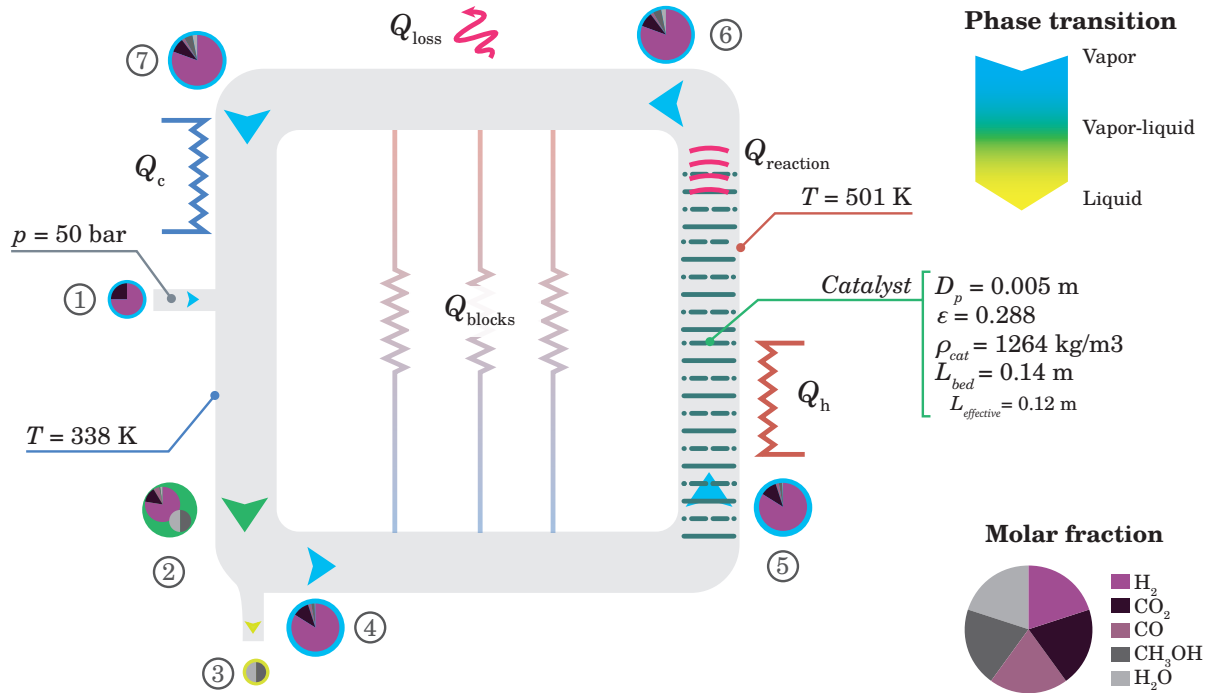


Fig. 4.18. Overall system overview

Tab. 4.10. Streams in SMBR at steady-state operation

	1	2	3	4	5	6	7	Unit
Mass flow	0.434	3.40 ± 0.81	0.429	3.40 ± 0.81	3.40 ± 0.81	3.40 ± 0.81	3.40 ± 0.81	1×10 <sup>-5</sup> kg/s
Temperature	303.15	338.75 ± 2.5	340.00	338.98 ± 1.7	424.90 ± 2.42	501.15	414.97 ± 5.25	K
H <sub>2</sub>	0.750	0.814	0.002	0.844	0.844	0.814	0.814	mol/mol
CO	0.000	0.026	0.000	0.025	0.025	0.026	0.026	mol/mol
CO <sub>2</sub>	0.250	0.095	0.007	0.113	0.113	0.095	0.095	mol/mol
H <sub>2</sub> O	0.000	0.027	0.496	0.004	0.004	0.027	0.027	mol/mol
CH <sub>3</sub> OH	0.000	0.038	0.495	0.015	0.015	0.038	0.038	mol/mol

Tab. 4.11. Energies in SMBR at steady-state operation. Units: W. Considering results from experimental characterization, and the reported cases (c) and (d) from Sec. 4.3 and 4.4

	Value	Uncertainty	Cases
$Q_{\text{loss}}$	50.27		Experimental
$Q_{\text{h}}$	9.26	± 0.51 W	Experimental, (c) and (d)
$Q_{\text{reaction}}$	4.16	± 0.01 W	Experimental and (c)
$Q_{\text{blocks}}$	9.96	± 1.32 W	Experimental and (d)
$Q_{\text{c}}$	14.62	± 0.06 W	Experimental and (c)
$Q_{\text{c,sens}}$	8.63	± 1.03 W	Experimental, (c) and (d)
$Q_{\text{c,lat}}$	6.34	± 0.02 W	Experimental and (c)

The sources of uncertainty are reported in the list below:

- ◇ Flow-rate in loop has an absolute uncertainty of 25% due to accounting of indirect experimental measurements. Using only the chemical process and CFD models, the value for the flow-rate becomes  $3.0 \pm 0.06 \times 10^{-5}$  kg/s. Its absolute uncertainty is 2%.
- ◇ Gas temperature at corners (2, 5, 6 and 7) have a maximum uncertainty of 5.25 K. The cooler inlet and outlet temperatures are the most uncertain due to the CFD models not accounting for effects of condensation.

The most uncertainty comes from the values which are not directly measured.

## 4.7 Improving reactor operation

Improving the SMBR means increasing the efficiency of its operation. As it was stated in Chapter 2, the two efficiencies to weigh the natural circulation reactor (according [Bos and Brillman](#)) are based on catalyst conversion efficiency (higher is better) and by specific energy consumption (lower is better). At the current stage of technological development of the chemical plant, ZEF BV prioritizes reducing on the former. Reducing the energy consumption of the reactor allows for the (limited) solar energy supply to be used into other subsystems, as presented in Fig. 1.1.

Reducing the specific energy consumption means that the energy used to operate the reactor should decrease in comparison to the methanol that is being generated. Based on the results gathered from the present research, improving the MBR operation should target reducing the energy losses and increasing the rate of methanol production.

### 4.7.1 Reducing energy losses

It is observed from Tab. 4.11 that **5 times the energy that goes into the flow at the heater is being dissipated into the environment**. Based on the information presented in Fig. 3.3, reducing the losses from the external insulation should be the priority.

An alternative approach could be to increase the heat recovery between the hot and cold legs of the reactor. In Tab. 4.11, the **energy recovered by the blocks is 1.07 times to the heat input** that enters the fluid. Increasing the heat recovery has a practical limitation: it was reported from the experimental characterization that the original MBR, which used 6 heat recovery blocks with multi-channel legs (See Fig. 2.4), had **premature condensation in the heat recovery blocks**, clogging the flow in the reactor [3].

### 4.7.2 Increasing methanol production rate

When the SMBR reaches steady-state operation, the gas composition entering the catalyst bed is in balance between how much methanol and water the reactor produces in one pass, and how much the condenser can separate it. The volume of the condensed liquid is replaced by fresh feed to maintain the operation pressure of 50 bar.

Consider an idealized methanol conversion profile presented in Fig. 4.19. There is a maximum amount of methanol concentration achievable when the composition reaches equilibrium. This composition is reached when residence time  $t$  is equal to the time it takes to reach equilibrium  $t_{eq}$ . For a straight pipe reactor, the residence time scales with the length of the reactor bed and the flow-rate, as Eq. 4.12.

$$t \sim \frac{L_{bed}}{W}; \quad t_{eq} \sim \frac{L_{bed}}{W_{eq}} \quad (4.12)$$

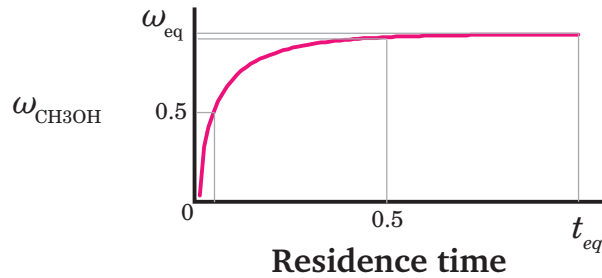


Fig. 4.19. Idealized methanol conversion profile in a plug flow reactor. Based on inlet reactor composition from Tab. 4.6

For a fixed reactor bed length, if the flow-rate in the reactor doubles, the residence time is reduced by half. The methanol composition of the stream does not reduce by the same factor, as the conversion is profile is not linear (See Fig. 4.17).

If the goal of a higher production rate of methanol is desired, it is theorized that for a fixed reactor bed length, a maximum point of production rate as a function of flow-rate (point A in Fig. 4.20) could be determined through an optimization process (beyond the scope of this research). However, because the **thermal energy input to the reactor scales with the flow-rate** (see Figs 4.4 and 4.7), the point of smallest specific energy consumption will differ from the point of highest production rate (point B in Fig. 4.20).

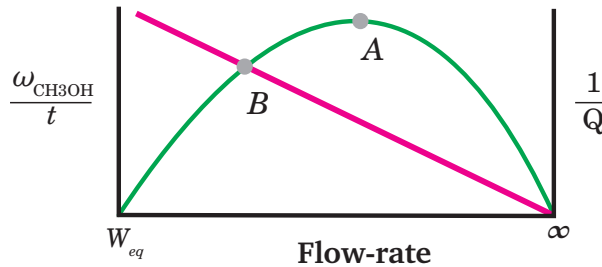


Fig. 4.20. Conceptual relation between methanol production rate and flow-rate (green) for a plug flow reactor against the inverse of thermal energy consumption which occurs on a natural circulation loop (pink). Point A provides highest production based on flow-rate. Point B represents a theoretical point of smallest specific energy consumption.

Additionally, a higher production rate of methanol requires a higher cooling duty for the cooling block to condense the methanol / water mixture from the SMBR. From Tab. 4.11, the **latent heat of condensation for the water/methanol product represents 40% of the heat released by the cooling block**. Attention should be given to study the limits of the passive cooling in the condenser block.

Based on the present research, two options are available to increase the flow-rate: Reduce the flow restriction from the catalyst bed and increase the buoyant driving forces in the reactor by tilting the reactor. Each approach has their own problems:

- ◇ In Eqs. 4.4 and 4.3, an observation of the scaling for flow-rate is presented. What this analysis overlooks is that by increasing the catalyst diameter or reducing the bed length **the catalyst surface will also reduce**, increasing the required residence time to achieve the same conversion to methanol. Reducing the catalyst surface also limits the heat transfer between the packed bed and the gases, further

decreasing the effective length of the bed with temperatures that can trigger the methanol synthesis reaction (see Fig. 4.9b).

- ◇ From Tab. 4.1 it is observed that tilting a natural circulation loop reduces the temperature difference between the hot and cold legs, **reducing the effectivity of the heat recovery blocks.**

## Chapter 5

# Conclusions and recommendations

In the current work, the steady-state modeling of a novel natural circulation catalytic reactor for methanol synthesis has been performed combining two models: A 1D chemical process model for describing the energy and mass balance of a multicomponent multiphase mixture, and a 3D CFD model for solving the energy and momentum balance for a single-phase multicomponent mixture.

Values obtained have been compared to the experimental characterization of the reactor performed by [Basarkar \(2018\)](#), with reasonable certainty.

### 5.1 Concluding remarks

- ◇ The flow-rate of a natural circulation loop is dependent on the positioning of the heating and cooling elements in respect to the vertical axis (gravity direction). A larger height difference between the heating and cooling elements leads to a larger buoyancy force to drive the flow. The SMBR with vertically placed heating and cooling elements can achieve this by tilting its position in the clock-wise direction.
- ◇ For a natural circulation loop, the vertical configuration of the heating and cooling elements is most optimal for heat recovery. This is attributed to a larger temperature difference between the channels that connect the hot and cold portions of the loop, in comparison to a horizontally placed heating and cooling elements. The energy recovered through the heat recovery blocks is approximately the same energy used as an input on the heating element.
- ◇ The catalyst packed bed limits the flow-rate in the natural circulation reactor by adding an additional restriction to the stream. Reducing the blockage will increase the mass flow, at a cost of a higher energy demand.
- ◇ A small temperature gradient is observed in the gas as it enters the catalytic zone. A temperature lower than required to trigger the methanol synthesis reactions is observed near the inlet. This represents a reduction to the effective length of the reactor bed.
- ◇ A 1D steady-state chemical process model can sufficiently describe the behavior of the continuous operation of the SMBR, based on the experimental measurements reported by [Basarkar](#).
- ◇ The [Bussche and Froment](#) GKM in CFD simulations has been implemented and validated for 3D plug flow reactors. The implementation is not sufficient to describe the SMBR, as it does not account for condensation. Without it, the simulation operation conditions diverge from the prototype.



## 5.2 Recommendations

- ◇ Data collected from the SMBR is limited to temperature of solid blocks, and mass flow in and out of the system. Installing more sensors in the prototype is required for a complete validation of the model. The most needed values are: temperature profile inside the reactor, gas flow-rate inside the loop and energy dissipated by the condenser.
- ◇ A reduction of the pressure drop in the packed bed or a tilt of the reactor in the clock-wise direction can be implemented in the prototype to obtain a higher methanol production rate at the cost of a higher energy demand.
- ◇ Although the COCO™ model accounts for most of the phenomena in the MBR, it does not calculate the flow-rate inside the loop. Suitable changes need to be implemented in the 1D model to account for these effects.
- ◇ The SMBR operates within the validity range of the [Bussche and Froment](#) GKM. If fractions of CO within 4-15 mole% are detected at the reactor inlet, the [Seidel et al.](#) GKM model should be used instead.

# Bibliography

- [1] United Nations. Adoption of the paris agreement. In *Conference of the parties. Twenty-first session*, 2015. URL <https://unfccc.int/resource/docs/2015/cop21/eng/l09r01.pdf>.
- [2] Daniel Franklin, Prof Frank Wilczek, Dr Rob Carlson, Alastair Reynolds, Prof Giannico Farrugia, Ann Winblad, Tom Standage, and Melinda Gates. *Megatech: Technology in 2050*. The economist, 2017.
- [3] Pratik Basarkar. Experimental characterization of a small scale methanol synthesis reactor. Master's thesis, TU Delft, 2018.
- [4] Shell. Shell scenarios: Sky, meeting the goals of the paris agreement. Technical report, Shell, 2017.
- [5] Hansen John Bøgdil and Højlund Nielsen Poul Erik. *Methanol Synthesis*. American Cancer Society, 2008. ISBN 9783527610044. doi: 10.1002/9783527610044.hetcat0148. URL <https://onlinelibrary.wiley.com/doi/abs/10.1002/9783527610044.hetcat0148>.
- [6] Giulia Bozzano and Flavio Manenti. Efficient methanol synthesis: Perspectives, technologies and optimization strategies. *Progress in Energy and Combustion Science*, 56:71 – 105, 2016. ISSN 0360-1285.
- [7] M.J. Bos and D.W.F. Brilman. A novel condensation reactor for efficient CO<sub>2</sub> to methanol conversion for storage of renewable electric energy. *Chemical Engineering Journal* 278, 2015.
- [8] Christopher Graves, Sune D. Ebbesen, Mogens Mogensen, and Klaus S. Lackner. Sustainable hydrocarbon fuels by recycling co<sub>2</sub> and h<sub>2</sub>o with renewable or nuclear energy. *Renewable and Sustainable Energy Reviews*, 15(1):1 – 23, 2011. ISSN 1364-0321.
- [9] L. Chen, Q. Jiang, Z. Song, and D. Posarac. Optimization of Methanol Yield from a Lurgi Reactor. *Chemical Engineering and Technology*, 34(5):817–822, 2011. ISSN 09307516. doi: 10.1002/ceat.201000282.
- [10] K.C. Waugh. Methanol synthesis. *Elsevier Science Publishers B.V.*, 15:51–75, 1992.
- [11] Ludolf Plass Friedrich Schmidt, Norbert Ringer. *Methanol: The Basic Chemical and Energy Feedstock of the Future*, chapter The Catalysis of Methanol Synthesis. Springer, 2014.
- [12] K.M. Vanden Bussche and G.F. Froment. A steady-state kinetic model for methanol synthesis and the water gas shift reaction on a commercial cu/zno/al<sub>2</sub>o<sub>3</sub> catalyst. *Journal of Catalysis*, 1996.
- [13] S. Ergun. Fluid flow through packed columns. *Chem. Eng.* 48, pages 89–94, 1952.

- [14] C. V. Ovesen, B. S. Clausen, J. Schiøtz, P. Stoltze, H. Topsøe, and J. K. Nørskov. Kinetic implications of dynamical changes in catalyst morphology during methanol synthesis over Cu/ZnO catalysts. *Journal of Catalysis*, 168(2):133–142, 1997. ISSN 00219517. doi: 10.1006/jcat.1997.1629.
- [15] Outi Mäyrä and Kauko Leiviskä. Modeling in methanol synthesis. *Methanol: Science and Engineering*, pages 475–492, 2017. doi: 10.1016/B978-0-444-63903-5.00017-0.
- [16] Geert Graaf, P.J.J.M. Sijtsema, E.J. Stamhuis, and G.E.H. Joosten. Chemical equilibria in methanol synthesis. 41:2883–2890, 1986.
- [17] G.C. Chinchen, K.C. Waugh, and D.A. Whan. The activity and state of the copper surface in methanol synthesis catalysts. *Applied Catalysis*, 25(1):101 – 107, 1986. ISSN 0166-9834. doi: [https://doi.org/10.1016/S0166-9834\(00\)81226-9](https://doi.org/10.1016/S0166-9834(00)81226-9). URL <http://www.sciencedirect.com/science/article/pii/S0166983400812269>.
- [18] Leonie E. Lücking. Methanol production from syngas: Process modelling and design utilising biomass gasification and integrating hydrogen supply. Master's thesis, TU Delft, 2017.
- [19] K. Klier, V. Chatikavanij, R.G. Herman, and G.W. Simmon. Catalytic synthesis of methanol from CO<sub>2</sub>: Iv. the effects of carbon dioxide. *Journal of Catalysis*, 74(2):343 – 360, 1982. ISSN 0021-9517. doi: [https://doi.org/10.1016/0021-9517\(82\)90040-9](https://doi.org/10.1016/0021-9517(82)90040-9). URL <http://www.sciencedirect.com/science/article/pii/0021951782900409>.
- [20] C. Seidel, A. Jörke, B. Vollbrecht, A. Seidel-Morgenstern, and A. Kienle. Kinetic modeling of methanol synthesis from renewable resources. *Chemical Engineering Science*, 175:130–138, 2018. doi: 10.1016/j.ces.2017.09.043. URL <https://doi.org/10.1016/j.ces.2017.09.043>.
- [21] Geert H. Graaf and Jozef G.M. Winkelman. Chemical Equilibria in Methanol Synthesis Including the Water-Gas Shift Reaction: A Critical Reassessment. *Industrial and Engineering Chemistry Research*, 55(20):5854–5864, 2016. doi: 10.1021/acs.iecr.6b00815.
- [22] Joost G. van Bennekom, Jozef G.M. Winkelman, Robertus H. Venderbosch, Sebastiaan D.G.B. Nieland, and Hero J. Heeres. Modeling and Experimental Studies on Phase and Chemical Equilibria in High-Pressure Methanol Synthesis. *Industrial & Engineering Chemistry Research*, 51(38):12233–12243, 2012. ISSN 0888-5885. doi: 10.1021/ie3017362. URL <http://pubs.acs.org/doi/abs/10.1021/ie3017362>.
- [23] Vipul S. Parekh and Paul M. Mathias. Efficient flash calculations for chemical process design - Extension of the Boston-Britt "Inside-out" flash algorithm to extreme conditions and new flash types. *Computers and Chemical Engineering*, 22(10):1371–1380, 1998. doi: 10.1016/S0098-1354(98)00222-1.
- [24] J. F. Boston and H. I. Britt. A radically different formulation and solution of the single-stage flash problem. *Computers and Chemical Engineering*, 2(2-3):109–122, 1978. doi: 10.1016/0098-1354(78)80015-5.
- [25] Richard Baur, Jasper van Baten, Harry Kooijman, and Werner Drewitz. Cross platform modeling of chemical processes. *NPT*, 2006.
- [26] J. Boussinesq. Theorie de l'intumescence liquide, appelée onde solitaire ou de translation, se propageant dans un canal rectangulaire. *Comptes Rendus de l'Académie des Sciences*, 72: 755–759, 1871.

- 
- [27] P. K. Vijayan. Experimental observations on the general trends of the steady state and stability behaviour of single-phase natural circulation loops. *Nuclear Engineering and Design*, pages 139–152, 2002.
- [28] B. T. Swapnalee and P. K. Vijayan. A generalized flow equation for single phase natural circulation loops obeying multiple friction laws. *International Journal of Heat and Mass Transfer*, 54(11-12):2618–2629, 2011. URL <http://dx.doi.org/10.1016/j.ijheatmasstransfer.2011.01.023>.
- [29] P. K. Vijayan, M. Sharma, and D. Saha. Steady state and stability characteristics of single-phase natural circulation in a rectangular loop with different heater and cooler orientations. *Experimental Thermal and Fluid Science*, 31:925–945, 2007.
- [30] Mayur Krishnani and Dipankar N. Basu. On the validity of boussinesq approximation in transient simulation of single-phase natural circulation loops. *International Journal of Thermal Sciences*, 105:224–232, 2016. ISSN 12900729.
- [31] Mayur Krishnani and Dipankar N. Basu. Computational stability appraisal of rectangular natural circulation loop: Effect of loop inclination. 107, 2017. ISSN 18732100. URL <http://dx.doi.org/10.1016/j.anucene.2017.04.012>.
- [32] Dipankar N. Basu, Souvik Bhattacharyya, and P. K. Das. Influence of geometry and operating parameters on the stability response of single-phase natural circulation loop. *International Journal of Heat and Mass Transfer*, pages 322–334, 2013. ISSN 00179310.
- [33] L.F. Moody. Friction factors for pipe flow. *Transactions of the ASME*, 66:671–684, 1944.
- [34] J. Y. Wang, T. J. Chuang, and Y. M. Ferng. Cfd investigating flow and heat transfer characteristics in a natural circulation loop. *Annals of Nuclear Energy*, 58, 2013. ISSN 03064549.
- [35] Naveen Kumar, J. B. Doshi, and P. K. Vijayan. Investigations on the role of mixed convection and wall friction factor in single-phase natural circulation loop dynamics. *Annals of Nuclear Energy*, 38:2247–2270, 2011. doi: 10.1016/j.anucene.2011.06.004.
- [36] William F. Louisos, Darren L. Hitt, and Christopher M. Danforth. Chaotic flow in a 2d natural convection loop with heat flux boundaries. *International Journal of Heat and Mass Transfer*, 61:565–576, 2013.
- [37] D. S. Pikhwal, W. Ambrosini, N. Forgiione, P. K. Vijayan, D. Saha, and J. C. Ferreri. Analysis of the unstable behaviour of a single-phase natural circulation loop with one-dimensional and computational fluid-dynamic models. *Annals of Nuclear Energy*, 34(5):339–355, 2007. doi: 10.1016/j.anucene.2007.01.012.
- [38] Ansys. FLUENT Theory Guide. 2009. ISSN 01403664. doi: 10.1016/0140-3664(87)90311-2.
- [39] Mechanical and UC San Diego Aerospace Engineering. Chemical-kinetic mechanisms for combustion applications. <https://web.eng.ucsd.edu/mae/groups/combustion/mechanism.html>, 2016.
- [40] Edward N. Fuller, Paul D. Schettler, and J. Calvin Giddings. A new method for prediction of binary gas-phase diffusion coefficients. *Industrial and Engineering Chemistry*, 58(5):18–27, 1966. ISSN 00197866. doi: 10.1021/ie50677a007.
- [41] B. J. Lommerts, G. H. Graaf, and A. A C M Beenackers. Mathematical modeling of internal mass transport limitations in methanol synthesis. *Chemical Engineering Science*, 55(23):5589–5598, 2000. doi: 10.1016/S0009-2509(00)00194-9.
-

- [42] Chi-Hsiung Li and B. A. Finlayson. Heat transfer in packed beds. a reevaluation. *Chemical Engineering Science*, 32:1055–1066, 1977.
- [43] Ray Sinnott and Gavin Towler. Chemical Engineering design: Principles, Practice and Economics of Plant and process Design. *Chemical Engineering Design*, pages 1–1271, 2013.
- [44] Laurel Murphy, Patrick J Roache, Kirti N Ghia, and Frank M White. Editorial policy statement on the control of numerical accuracy. *Journal of Fluids Engineering*, 108, 2003. doi: 10.1115/1.3242537.
- [45] Gesellschaft VDI. *VDI Heat Atlas*. VDI-Buch. Springer Berlin Heidelberg, 2010. ISBN 9783540778769.
- [46] R. C. Reid, J. M. Prausnitz, and B. E. Poling. *The properties of gases and liquids*. McGraw-Hill, 4th edition, 1987.

# Appendices



# Appendix A

## Fluid properties

### A.1 Basic model

*Temperature fitting feed gas mixture at 50 bar*

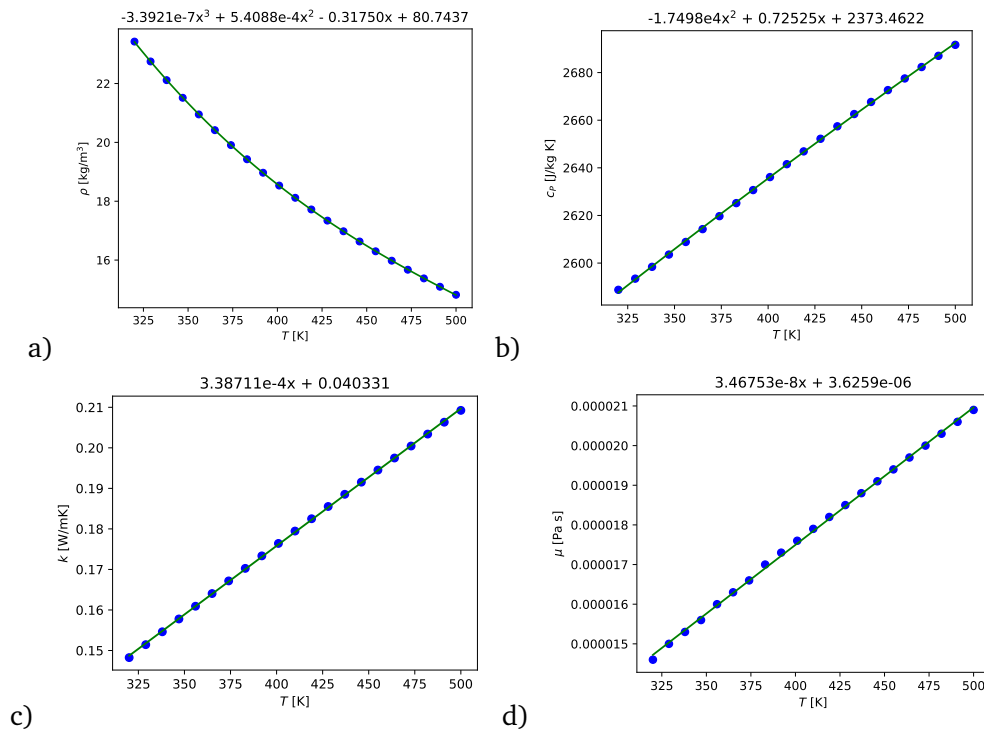


Fig. A.1. Polyfit properties for mixture of H<sub>2</sub>, CO<sub>2</sub> (0.75,0.25) at 50 bar, for working temperature range in the MBR

$$\rho(T) = -3.3921E-7x^3 + 5.4088E-4x^2 - 0.31750x + 80.7437 \text{ kg/m}^3$$

$$c_p(T) = -1.7498E-4x^2 + 0.72525x + 2373.4622 \text{ J/kgK}$$

$$\lambda(T) = 3.38711E-4x + 0.040331 \text{ kg/m}^3$$

$$\mu(T) = 3.46753E-8x + 3.6259E-6 \text{ Pa}\cdot\text{s}$$



### Temperature fitting nitrogen at 50 bar

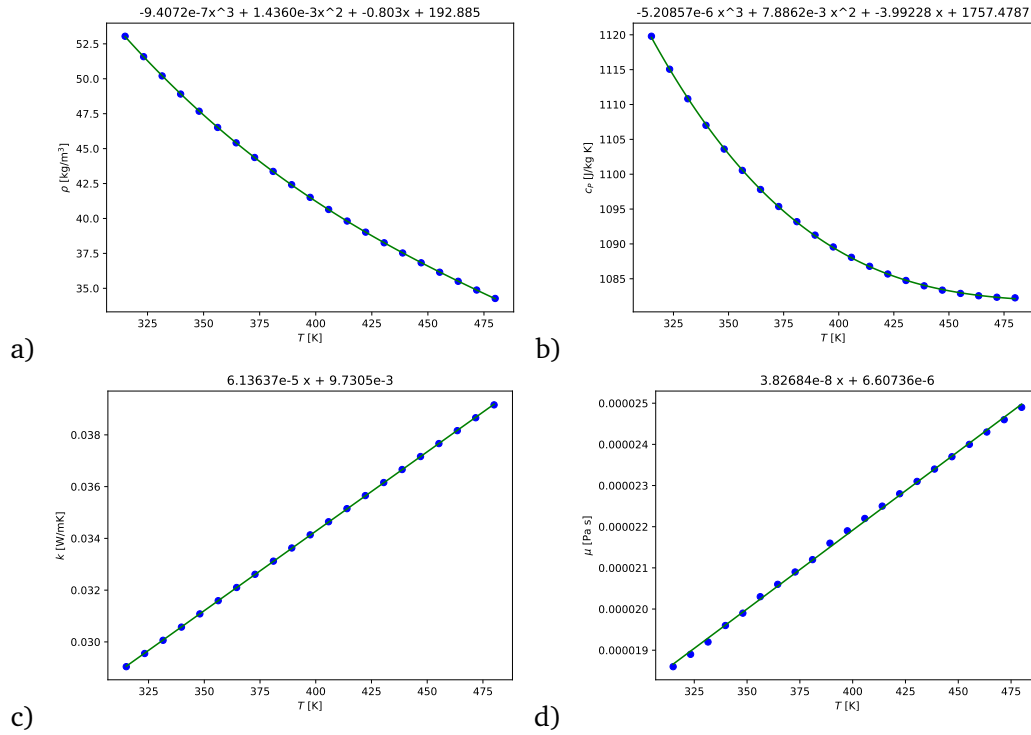


Fig. A.2. Polyfit properties for nitrogen at 50 bar, for working temperature range in the MBR

$$\begin{aligned}\rho(T) &= -9.40725E-7x^3 + 0.00143602x^2 - 0.803021x + 192.885 \text{ kg/m}^3 \\ c_p(T) &= -5.20857E-6x^3 + 7.8862E-3x^2 + -3.99228x + 1757.4787 \text{ J/kgK} \\ \lambda(T) &= 6.13637E-5x + 0.0097305 \text{ W/mK} \\ \mu(T) &= 3.8268E-8x + 6.60735E-6 \text{ Pa}\cdot\text{s}\end{aligned}$$

## A.2 Detailed model

### Density

Using Soave-Redlich-Kwong EOS, Fluent™ determines the specific molar volume  $v$ , as is the simplest of the cubic equations of state. Critical pressure and temperature are provided by San Diego University's Thermodynamic database [39].

$$P = \frac{RT}{v-b} - \frac{a}{v^2 + bv}$$

$$\alpha(T) = \frac{0.42747R^2T_c^2}{P_c\sqrt{T/T_c}}; \quad b = \frac{0.08664RT_c}{P_c}$$

Where:

- $v$  is specific molar volume
- $P_c$  is critical pressure
- $T_c$  is critical volume

### Specific heat

Using the San Diego University compendium of thermodynamic and transport properties [39], which provide a large set of temperature dependent approximations for the following values:

$$\begin{aligned}\frac{c_p}{R} &= a_1 + a_2 T + a_3 T^2 + a_4 T^3 + a_5 T^4 \\ \frac{\Delta H}{RT} &= a_1 + \frac{a_2 T}{2} + \frac{a_3 T^2}{3} + \frac{a_4 T^3}{4} + \frac{a_5 T^4}{5} + \frac{a_6}{T} \\ \frac{\Delta S}{R} &= a_1 \ln(T) + a_2 T + \frac{a_3 T^2}{2} + \frac{a_4 T^3}{3} + \frac{a_5 T^4}{4} + a_7\end{aligned}$$

The values for  $\frac{\Delta H}{RT}$  and  $\frac{\Delta S}{R}$  are be used for **determining heat of formation** from the reactions.

For multicomponent mixtures, enthalpy of mixture is determined by a mass fraction mixing.

$$h(T) = \sum_{i=1}^N \omega_i \int_{T_{\text{ref}}}^T c_{p_i} dT$$

### Species transport diffusion

The key parameter is the diffusion coefficients  $D_{ij}$ . These have to be calculated for each binary interaction between the species. For a full multi-component diffusion in gases, the model (currently) uses the Chapman-Enskog formula. This is formula is **only true for ideal gases**.

$$D_{ij} = 0.00188 \frac{T^3 (\text{MW}_i^{-1} + \text{MW}_j^{-1})^{0.5}}{p \sigma_{ij}^2 \Omega_d}$$

Where:

$\sigma_{ij}$  is the average collision rate.

$\Omega_d$  is obtained through temperature fitting, though the **approach used is undisclosed** by Chemkin.

The values of the diffusion coefficients determined at runtime **are not stored or visible to the user**. This scientific uncertainty could be overcome by using an alternative model where all the values are set by the user. The recommended approach would be to use UDFs to determine the binary diffusion coefficients following the work of Fuller et al. (1966). It has been reported by Lommerts et al. (2000) that for the modeling of methanol synthesis under the working pressures of the MBR, would provide only slight improvements in the accuracy compared to the Chapman-Enskog formula.

$$D_{ij} = \frac{10^{-4} T^{1.75}}{p \sqrt{M_i} (\sum v_i^{1/3} + \sum v_j^{1/3})^2}$$

Where:

$\sum v_i$  is the summation of atomic diffusion volumes. Values for all species reported by Fuller et al. (1966), except for methanol; this value is obtained from Reid et al. (1987) as  $29.9 \text{ cm}^3 \text{ mol}^{-1}$ .



# Appendix B

## Data

### B.1 Tilting UDL

#### B.1.1 Simulation settings

*Reporting values*

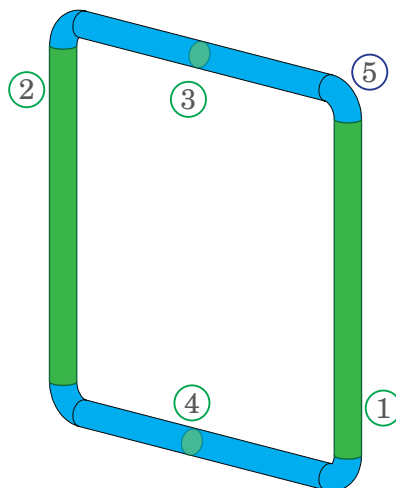


Fig. B.1. Location of surface and volume reports. Blue: Volume zone. Green: Surface zone

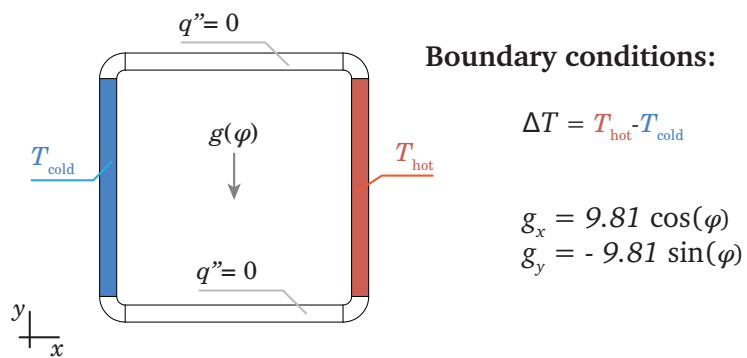


Fig. B.2. Boundary conditions used for the simulations

Tab. B.1. Reporting values and respective zones

Name	Value	Report type	Zone from Fig. B.1	Units
a_flow	Area	Area	3	m <sup>2</sup>
beta	Eq. B.1	Calculation	3,4	-
cp_o	Specific heat	Volume average	5	J/kg/K
delta-t_r	Eq. B.2	Calculation		-
gr_m	Eq. B.3	Calculation		-
mu_o	Viscosity	Volume average	5	Pa s
q_hot	Heat flux	Integral	1	W
q_cold	Heat flux	Integral	2	W
rho_bottom	Density	Area weighted avg.	4	kg/m <sup>3</sup>
rho_o	Density	Volume average	5	kg/m <sup>3</sup>
rho_top	Density	Area weighted avg.	3	kg/m <sup>3</sup>
t_bottom	Temperature	Area weighted avg.	4	K
t_top	Temperature	Area weighted avg.	3	K
w_ss	Mass flow	Mass flow	3,4	kg/s
gr_m-n_g	Eq. B.4	Calculation		-
re_ss	Eq. B.5	Calculation		-

Where:

$$\beta = -\frac{1}{\rho} \left( \frac{\partial \rho}{\partial T} \right)_p \approx \frac{1}{\rho_{o}} \left( \frac{\rho_{\text{bottom}} - \rho_{\text{top}}}{t_{\text{top}} - t_{\text{bottom}}} \right) \quad (\text{B.1})$$

$$re_{ss} = \frac{w_{ss} \cdot D_o}{a_{\text{flow}} \cdot \mu_o} \quad (\text{B.2})$$

$$\Delta t_r = \frac{q_{\text{hot}} \cdot H}{a_{\text{flow}} \cdot cp_o \cdot \mu_o} \quad (\text{B.3})$$

$$gr_m = \frac{D_o^3 \cdot \rho_o^2 \cdot \beta \cdot g \cdot \Delta t_r}{\mu_o^2} \quad (\text{B.4})$$

$$gr_{m-n_g} = \frac{gr_m}{L_t/D_o} \quad (\text{B.5})$$

For the UDL, these values are:

$$D_o = 0.010 \text{ m}$$

$$H = 0.15 \text{ m}$$

$$L_t = 0.6 \text{ m}$$

### Meshing

- ◇ 230k nodes
- ◇ CFD
- ◇ Assembly method: Manual structured cell
- ◇ Inflation:
  - Layers: 5
  - Growth rate: 1.2

### Fluent™ setup

- ◇ Steady, pressure based solver, gravity
- ◇ Models:

- Energy: On
- Viscosity: k- $\epsilon$ 
  - RNG
  - Standard wall functions
  - Full buoyancy
- ◇ Materials:
  - Solid: Aluminium
  - Fluid: Nitrogen using basic FP model.
    - Density: Temperature polynomial fit
    - Cp: Temperature polynomial fit
    - $\lambda$ : Temperature polynomial fit
    - $\mu$ : Temperature polynomial fit
- ◇ Boundary Conditions:
  - adiabatic: no heat flux, no slip
  - hot: fixed temperature
  - cold: fixed temperature
- ◇ Initialization: Manual
  - From hot boundary condition.
- ◇ Residuals:
  - Continuity: 1e-5
  - Energy: 1e-10
  - k: 1e-5
  - $\epsilon$ : 1e-5
- ◇ Methods:
  - Pressure: PRESTO
  - Density: Second order upwind
  - Momentum: Second order upwind
  - Turbulent kinetic: Second order upwind
  - Turbulent dissipation: Second order upwind
  - Energy: QUICK
- ◇ URF: Default

## B.1.2 Results

### B.1.2.1 $\varphi = 90$

Report name	$\Delta T$						Unit
	5	10	20	50	100	200	
a-flow	7.73E-05	7.73E-05	7.73E-05	7.73E-05	7.73E-05	7.73E-05	m2
beta	0.002491128	0.002467867	0.002465028	0.002398427	0.002466445	0.0024776	
cp-o	1088.514	1088.1595	1088.1688	1086.9524	1088.5576	1089.9877	j/kg-k
delta-t-r	7662.8281	18376.994	50800.867	193780.91	565478.25	1580940.9	
gr-m	1.08E+09	2.54E+09	7.01E+09	2.48E+10	7.87E+10	2.27E+11	
mu-o	1.66E-05	1.66E-05	1.66E-05	1.66E-05	1.66E-05	1.66E-05	kg/m-s
q	0.071479836	0.17136712	0.47372668	1.8050197	5.2750647	14.767184	w
rho-bottom	40.014518	39.831303	40.004684	39.561291	41.559763	43.953902	kg/m3
rho-o	39.963524	39.718038	39.721769	38.795886	39.874336	40.432718	kg/m3
rho-top	39.912448	39.604443	39.437432	38.021086	38.14376	36.701618	kg/m3
t-bottom	411.98177	413.83432	412.08075	416.59763	397.04586	376.10845	k
t-top	413.00706	416.14878	417.87407	433.15021	431.77974	448.50172	k
w-ss	6.40E-05	6.80E-05	7.51E-05	0.000100301	0.000139464	0.000187118	kg/s
gr-m-n-g	18023784	42296572	1.17E+08	4.14E+08	1.31E+09	3.79E+09	
re-ss	498.25687	529.32831	584.55017	780.28894	1084.9569	1455.6749	

**B.1.2.2  $\varphi = 1$**

Values for the horizontal and vertical components of the gravity vector as  $g_x = 9.8085059$ ;  $g_y = -0.1712081$

Report Name	$\Delta T$						Unit
	2	5	10	20	50	100	
a_flow	7.73E-05	7.73E-05	7.73E-05	7.73E-05	7.73E-05	7.73E-05	m2
beta	0.002490086	0.002479895	0.002462962	0.002463193	0.002398743	0.002470594	
cp_o	1088.7335	1088.5134	1088.1592	1088.1663	1086.9258	1088.4201	j/kg-k
delta-t_r	4670.2896	16779.52	44920.844	123123.77	448920.63	1264768	
gr_m	6.64E+08	2.36E+09	6.19E+09	1.70E+10	5.75E+10	1.76E+11	
mu_o	1.66E-05	1.66E-05	1.66E-05	1.66E-05	1.66E-05	1.66E-05	kg/m-s
q	0.043573841	0.15652141	0.41889074	1.1481472	4.1814783	11.796899	w
rho_bottom	40.133344	40.011254	39.80865	39.897214	39.191369	40.657577	kg/m3
rho_o	40.111986	39.96305	39.717898	39.72175	38.794628	39.862223	kg/m3
rho_top	40.09061	39.914782	39.626931	39.545437	38.392496	39.04023	kg/m3
t_bottom	4.11E+02	412.01019	414.06022	413.16159	420.44616	405.62666	k
t_top	411.21326	4.13E+02	4.16E+02	416.75693	429.03083	422.04918	k
w_ss	9.36E-05	0.000147945	0.000207516	0.000292906	0.000443411	0.000646739	kg/s
gr_m-n_g	1.11E+07	3.93E+07	1.03E+08	2.83E+08	9.58E+08	2.94E+09	
re_ss	728.08655	1150.9312	1614.3613	2278.6428	3449.4885	5031.2676	

**B.1.2.3  $\varphi=45^\circ$**

Values for the horizontal and vertical components of the gravity vector as  $g_x = -g_y = 6.936718$

Report Name	$\Delta T$						Unit
	2	5	10	20	50	100	
a_flow	7.73E-05	7.73E-05	7.73E-05	7.73E-05	7.73E-05	7.73E-05	m2
beta	0.002509026	0.002488405	0.002467369	0.002465489	0.002400001	0.002472193	
cp_o	1088.7336	1088.5135	1088.1593	1088.1665	1086.9298	1088.4365	j/kg-k
delta-t_r	4143.5391	14608.253	38430.879	104289.64	368815.78	1038700.1	
gr_m	5.93E+08	2.06E+09	5.31E+09	1.44E+10	4.73E+10	1.45E+11	
mu_o	1.66E-05	1.66E-05	1.66E-05	1.66E-05	1.66E-05	1.66E-05	kg/m-s
q	0.038659257	0.13626758	0.35837132	0.97251647	3.4353539	9.688436	w
rho_bottom	40.133267	40.010207	39.805955	39.891687	39.181708	40.665268	kg/m3
rho_o	40.112052	39.963122	39.718	39.722058	38.799048	39.87735	kg/m3
rho_top	40.09082	39.915979	39.629856	39.551717	38.411867	39.069119	kg/m3
t_bottom	410.78842	412.02295	414.08985	413.21962	420.54863	405.54721	k
t_top	4.11E+02	4.13E+02	415.88678	416.69103	428.81605	421.7379	k
w_ss	8.42E-05	0.000132203	0.000183446	0.000257434	0.000379847	0.000544579	kg/s
gr_m-n_g	9.89E+06	3.43E+07	8.84E+07	2.40E+08	7.88E+08	2.41E+09	
re_ss	655.07825	1028.4684	1427.1033	2002.6888	2954.9944	4236.5151	

**B.1.2.4  $\varphi=75^\circ$**

Values for the horizontal and vertical components of the gravity vector as  $g_x = 2.5390148$ ;  $g_y = -9.4757324$

Report Name	$\Delta T$					Unit
	5	10	20	50	100	
a_flow	7.73E-05	7.73E-05	7.73E-05	7.73E-05	7.73E-05	m2
beta	0.002491196	0.002469002	0.002466281	0.002399712	0.002470313	
cp_o	1.09E+03	1.09E+03	1.09E+03	1.09E+03	1.09E+03	j/kg-k
delta-t_r	10817.008	27739.318	72534.305	256689.41	733030.13	
gr_m	1.53E+09	3.83E+09	1.00E+10	3.29E+10	1.02E+11	
mu_o	1.66E-05	1.66E-05	1.66E-05	1.66E-05	1.66E-05	kg/m-s
q	1.01E-01	2.59E-01	6.76E-01	2.39E+00	6.84E+00	w
rho_bottom	40.01183	39.806923	39.894089	39.219354	40.7819	kg/m3
rho_o	39.963383	39.718271	39.721916	38.792367	39.852333	kg/m3
rho_top	39.914866	39.629417	39.549029	38.361471	38.90508	kg/m3
t_bottom	4.12E+02	414.08156	413.1968	420.1543	404.41391	k
t_top	412.98212	4.16E+02	4.17E+02	429.36984	423.47803	k
w_ss	9.52E-05	1.31E-04	0.000176508	0.000238646	0.00032949	kg/s
gr_m-n_g	25443262	63875036	1.67E+08	5.48E+08	1.70E+09	
re_ss	740.4563	1021.7712	1373.1343	1856.532	2563.2449	

### B.1.2.5 $\varphi=85^\circ$

Values for the horizontal and vertical components of the gravity vector as  $g_x = 0.8549998$ ;  $g_y = -9.77267$

Report Name	$\Delta T$					Unit
	5	10	20	50	100	
a_flow	7.73E-05	7.73E-05	7.73E-05	7.73E-05	7.73E-05	m2
beta	0.00249119	0.002468966	0.002465817	0.002399073	0.002468097	
cp_o	1088.514	1088.1597	1088.1657	1086.9265	1088.4356	j/kg-k
delta-t_r	8895.4023	22331.469	57741.574	214107.25	618507.25	
gr_m	1.26E+09	3.09E+09	7.97E+09	2.74E+10	8.60E+10	
mu_o	1.66E-05	1.66E-05	1.66E-05	1.66E-05	1.66E-05	kg/m-s
q	0.082977443	0.20824298	0.53844848	1.9943067	5.7690994	w
rho_bottom	40.013372	39.810568	39.923295	39.332442	41.072965	kg/m3
rho_o	39.963472	39.718305	39.721246	38.790466	39.846958	kg/m3
rho_top	39.913497	39.62581	39.518252	38.242827	38.59346	kg/m3
t_bottom	411.99311	414.04492	412.90171	418.97094	401.62208	k
t_top	412.99628	415.92899	417.03706	430.67954	426.83408	k
w_ss	7.60E-05	0.000101565	0.00011965	0.000156693	0.000210242	kg/s
gr_m-n_g	20923396	51421784	1.33E+08	4.57E+08	1.43E+09	
re_ss	591.15369	790.12085	930.81152	1218.9866	1635.5676	

### B.1.3 Heat transfer coefficients

Comparison of heat transfer coefficients determined through CFD calculations with Nusselt number correlations for heat transfer in straight pipe.

Case	$Re_{ss}$ [-]	$W_{ss}$ [g/s]	$Q_{hot}$ [W]	$T_{wall}$ [K]	$T_{in}$ [K]	$T_{out}$ [K]	$U_{CFD}$ [W/m <sup>2</sup> K]	$U_{lam}$ [W/m <sup>2</sup> K]	$U_{trans}$ [W/m <sup>2</sup> K]	$U_{turb}$ [W/m <sup>2</sup> K]
N2 1°	5031	0.646	11.79	465	405.6	422	56.05	24.03	35.13	57.3
N2 45°	4236	0.544	9.68	465	405.5	421.7	45.84	22.67	30.32	51.2
N2 75°	2563	0.329	6.84	465	404.4	423.4	32.48	32.67	35.01	57.6
N2 85°	1635	0.210	5.76	465	401.6	426.8	27.97	16.59		28.2
N2 90°	1084	0.139	14.76	465	397.0	431.7	26.19	14.73		22.7





## Appendix C

# Fluent™ implementation of reactions

This chapter presents the code used to implement the [Bussche and Froment](#) GKM for methanol synthesis as a volumetric reaction. The procedure to implement it, is as follows:

1. In Models, enable Species transport.
2. Enable Volumetric reactions with no chemistry solver, i.e. Explicit source.
3. Select Import chemkin mechanism to add the gas species and reactions.  
For Kinetic input file use the file presented as **chem\_reactions.inp** below.  
For Thermodynamic and Transport data use the databases from San Diego University's chemical kinetic models [39].
4. In Cell zone conditions, select the volume that will be representative of the reactions.  
Enable porous zone and fill the equivalent inertial and viscous loss matrices  
Enable reaction and ensure that the reaction mechanism is selected. By default is named mechanism-1.
5. Now go to User defined functions and compile and hook the UDF presented as **bussche\_froment\_udf.c** to the volumetric reaction rate.  
Compiling and hooking UDFs in Windows is more problematic than in Linux. For a tutorial on how to compile UDFs in Windows, follow this link: [https://www.youtube.com/watch?v=xt2hnE9\\_LdM](https://www.youtube.com/watch?v=xt2hnE9_LdM)

### *chem\_reactions.inp*

```
! -----  
! Mechanism based on Brussche and Froment for Methanol synthesis from a CuZnAl  
! catalyst.  
! Values from Chen2011  
! Creates ARBITRARY Arrhenius reactions, to be overwritten by UDFs in Fluent  
! -----  
ELEMENTS  
  H O C N  
END  
! -----  
SPECIES  
  H2 CO2 CO CH3OH H2O N2  
END  
! -----  
REACTIONS  KJOULES/MOLE  
CO2+3H2<=>CH3OH+H2O      1.07e+9      0.0      36.696      ! MeOH  
CO2+H2<=>CO+H2O          1.22e+16      0.0      -94.765      ! RWGS  
END  
! -----
```



```
    }
    else if (!strcmp(r->name, "reaction-2")){
        /* REACTION 2: REVERSE WATER GAS SHIFT [kmol/m3/s]*/
        *rr = (k_2 * p_[CO2]) * (1 - (1/K_e2) * (p_[H2O] * p_[CO] / (p_[H2] * p_[CO2])));
        *rr = *rr * 2 * theta * rho_catalyst * 1e-3; /* 1e-3 for mol -> kmol */
    }
    else{
        printf("Unknown Reaction\n");
    }
    *rr_t = *rr; /* turbulent reaction rate = laminar reaction rate */
}
```

## C.1 Methanol synthesis reactor

The goal is to create a 3D CFD implementation of the **Bussche and Froment** GKM for methanol synthesis into Fluent. A 1D plug flow reactor was developed in COCO™ simulator to use as reference for debugging the 3D CFD reactor model.

### General configurations

The COCO™ simulator model for the **Bussche and Froment** GKM is implemented to a plug flow reactor. The reaction rate equations from Eq. 2.1 and 2.2 are defined with its respective grouped parameters  $\gamma$  and the equilibrium constants  $K_e$  from **Graaf et al.**. These reactions are written explicitly into a single equation in the COCO™ simulator interface, as shown in Fig. C.1

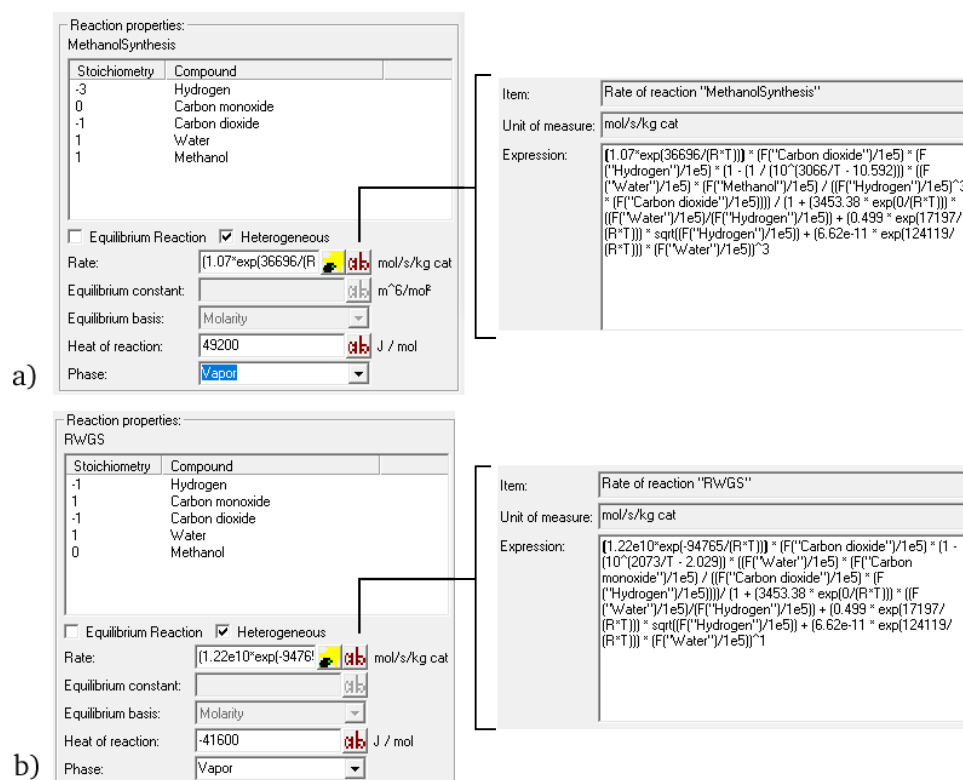


Fig. C.1. Implementation method for **Bussche and Froment** GKM for methanol synthesis in the COCO™ simulator interface.

The 3D CFD reaction model has to be solved as a transient simulation. Because of the chemistry is solved explicitly, the timestep for the simulation has to be selected to achieve a stable solution. For the calculation of the first 5 seconds of the simulation, a timestep of 0.0001 seconds was determined to be suitable. Afterwards, the timestep was slowly increased until reaching 0.01 seconds.

The catalytic packed bed is set to be in thermal equilibrium with the gases. Temperature boundary conditions and heat of reaction are the only energy sources that increase the temperature for gases along the reactor.

### Special considerations

This section compares transient simulations with reports for steady-state chemical reactor models from literature. To ensure that a steady-state has been achieved on a transient simulation, the criteria chosen was to compare the gas composition at the outlet. It must remain equal to 4 significant digits for a period of simulation time of 1 reactor lengthscale.

### Expected results

The ultimate goal is to debug the GKM into Fluent, comparing the results with other known models from literature. Once this is achieved, the GKM can be added to CFD models for the natural circulation reactor. This would allow the simulation to account for:

- ◇ Reaction energy. The reactions are for the most part exothermic, which adds additional energy to the flow.
- ◇ Changes in gas composition over time. The composition becomes more dense, which impacts the buoyant forces over time.

## C.1.1 Replicating Bussche and Froment model

### C.1.1.1 1D plug flow reactor

The first goal was to create a plug flow reactor model that can quickly calculate different conditions for the methanol synthesis reaction inside a straight pipe. The COCO™ simulator software [25] was used to create a PFR with the Bussche and Froment GKM. In Fig. C.2 a comparison between the conversion and temperature profiles for an adiabatic reactor is presented.

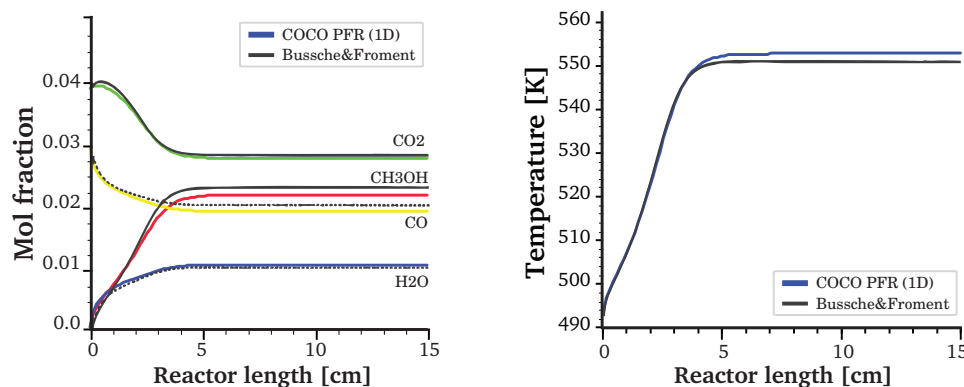


Fig. C.2. Comparing a 1D PFR developed in COCO™ simulator with the GKM from Bussche and Froment.

The operating conditions for the PFR simulation are set with values equal to those reported by Bussche and Froment, as follows:

- |                                                      |                                       |
|------------------------------------------------------|---------------------------------------|
| ◇ Length: 0.15 m                                     | Feed Composition in mole fraction     |
| ◇ Diameter: 0.016 m                                  | ◇ H <sub>2</sub> : 0.82               |
| ◇ $\rho_{\text{cat}}^i$ : 1153.87 kg m <sup>-3</sup> | ◇ H <sub>2</sub> O: 0.00              |
| ◇ Particle diameter: 5E-4 m                          | ◇ CH <sub>3</sub> OH: 0.00            |
| ◇ Mass flow: 2.8E-5 kg s <sup>-1</sup>               | ◇ CO: 0.04                            |
| ◇ Pressure: 50 bar                                   | ◇ CO <sub>2</sub> : 0.03              |
| ◇ Temperature inlet: 493.2 K                         | ◇ Inert: 0.11 (Using N <sub>2</sub> ) |



Fig. C.3. Visual representation of PFR component in process flowsheet environment of COCO™ simulator v3.2.0. Single phase PFR

<sup>i</sup>Calculated from reported mass of catalyst in the volume of reactor pipe [12].

## C.1.1.2 3D CFD reactor

As it was mentioned in Sec. 2.4.3, the GKM was implemented in a way that the composition is solved explicitly. This limits Fluent™ to only using a transient solver with small timesteps to obtain a stable result until it reaches steady-state.

## Geometry and mesh

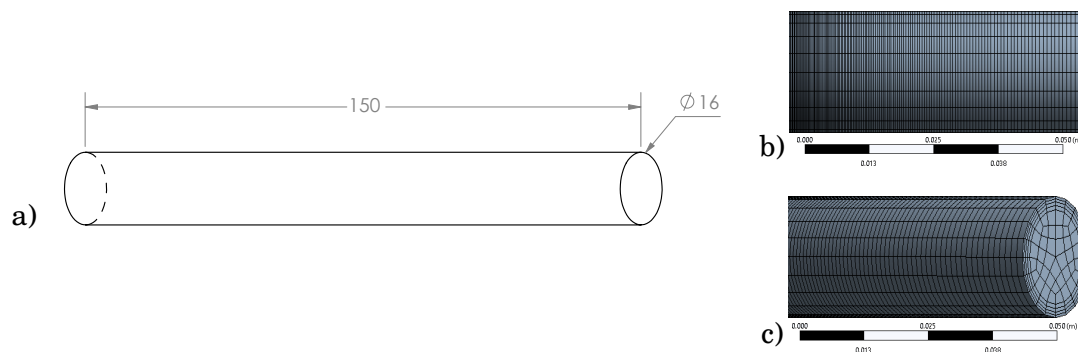


Fig. C.4. Reactor section of S/MBR geometry. a) 3D CAD diagram. Units:mm b) Excerpt of 32k cell mesh. Structured mesh with refinement at inlet. c) Excerpt of 32k cell mesh. Crosssection. Average mesh skewness: 0.1657. Average mesh orthogonality: 0.9831

## Boundary conditions

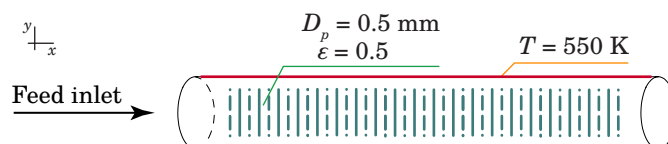


Fig. C.5. Boundary conditions diagram for replication of Bussche and Froment model.

## Results

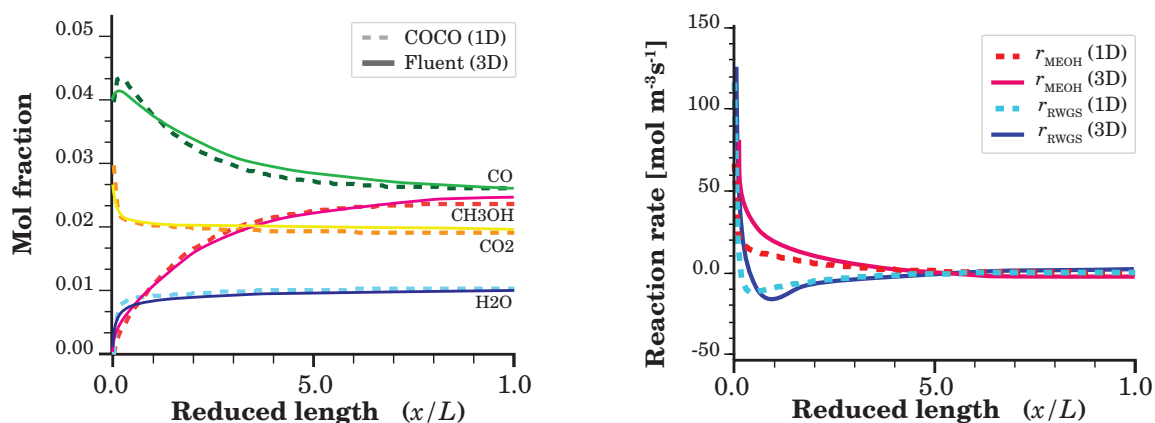


Fig. C.6. Plots over reduced length of reactor. a) Molar fraction, b) Reaction rates.

**Tab. C.1.** Comparing outlets of 1D PFR model (CapeOpen) with a 3D CFD transient simulation reaching steady-state (Fluent).  $p = 50\text{bar}$ ,  $W = 2.8\text{E-}4\text{kg s}^{-1}$ 

	Inlet	COCO™outlet	Fluent™outlet	Unit
Hydrogen	0.81	0.7998	0.7998	mol/mol
Carbon monoxide	0.04	0.0278	0.0270	mol/mol
Carbon dioxide	0.03	0.0204	0.0207	mol/mol
Methanol	0.005	0.0253	0.0259	mol/mol
Water	0.005	0.0111	0.0109	mol/mol
Nitrogen	0.11	0.1156	0.1157	mol/mol

### Observations

- ◇ The concentration profiles for the desired species are in close accordance to the 1D plug flow model.
- ◇ The rates of reaction calculated are higher for the 3D CFD reaction model than for the 1D plug flow model. This is attributed to an overshoot in the explicit calculation of the reaction rates.
- ◇ The end result confirms the accuracy of the implementation of the GKM from [Bussche and Froment](#) into Fluent™ for 3D CFD for **an isothermal reactor**.



### C.1.2 Replicating industrial reactor

Chen et al. used ASPEN to replicate the behavior of an industrial (boiling) water cooled methanol synthesis reactor. Assuming that the behavior is uniform across all pipes of the 1620 bundle, all inlet conditions can be determined from the aforementioned publication. This model uses a temperature and heat transfer boundary condition for the external wall of the reactor. A comparison is made between the results reported by Chen et al. with the models developed in the present work for both 3D CFD (Fluent) and 1D PFR (COCO).

#### Geometry and mesh

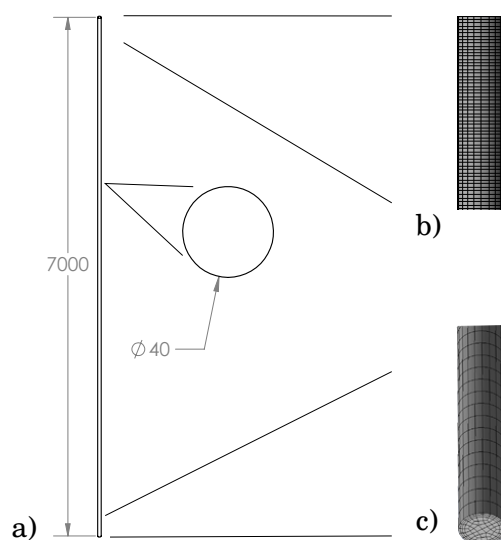


Fig. C.7. Reactor section of a single Lurgi reactor pipe. a) 3D CAD diagram. Units:mm b) Excerpt of 424k cell mesh. Structured mesh with refinement at inlet. c) Excerpt of mesh at outlet. Average mesh skewness: 0.1769. Average mesh orthogonality: 0.9798

#### Boundary conditions

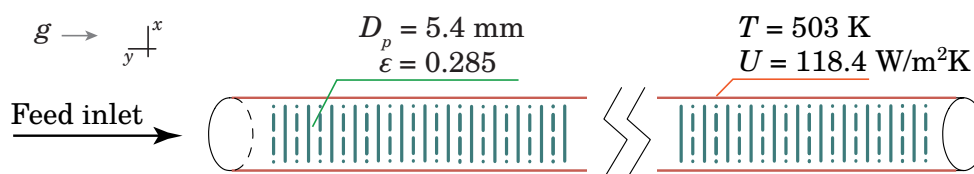


Fig. C.8. Boundary conditions for simulation of single pipe of isothermal Lurgi reactor for methanol synthesis [9]

- ◇ Inlet:
  - $p = 69.7 \text{ bar}$
  - $T = 500 \text{ K}$
  - $W = 1.5\text{E-}4 \text{ kg/s}$
- ◇ Feed composition (mol/mol):
  - $\text{H}_2 = 0.7732992$
  - $\text{CO} = 0.0622807$
  - $\text{CO}_2 = 0.0875113$
- ◇ Reactor packing:
  - $\text{H}_2\text{O} = 0.0009820$
  - $\text{CH}_3\text{OH} = 0.0038402$
  - $\text{Inert (N}_2) = 0.0720863$
  - $\rho_{\text{cat}} = 887.5 \text{ kg/m}^3$
  - $\epsilon = 0.285$
  - $D_p = 5.4 \text{ mm}$

## Results

In Fig. C.2, a comparison over the length of the reactor for mass flow (obtained from mass fraction), temperature and rate of reaction to reported values from [Chen et al.](#) and the 1D PFR model. Outlet values are reported in Tab. C.2.

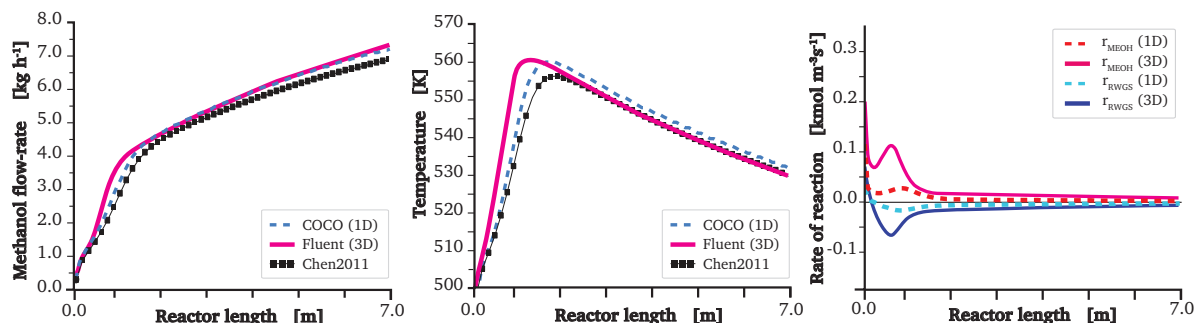


Fig. C.9. Over the length of the reactor, comparing mass flow, temperature and rates to values from literature and a 1D PFR model.

Tab. C.2. Comparison between literature, 1D PFR reaction model and 3D CFD transient model approaching steady-state.

	Experimental [9]	1D PFR (CapeOpen)	3D CFD (Fluent)	Unit
Pressure	66.7	66.78	66.64	bar
Temperature	528.15	531.78	529.34	K
Hydrogen	0.13989	0.13800	0.13851	kg/kg
Carbon monoxide	0.08590	0.08220	0.07967	kg/kg
Carbon dioxide	0.31975	0.30992	0.31631	kg/kg
Water	0.04031	0.04428	0.04166	kg/kg
Methanol	0.19697	0.20878	0.20703	kg/kg
Non-reactive (N <sub>2</sub> )	0.21671	0.21679	0.21679	kg/kg

## Observations

- ◇ When comparing the 1D model to the 3D model, an overestimation of the reaction rates is observed near the inlet. This is attributed to the explicit calculation of reaction rates that was also observed in the previous case study.
- ◇ The overestimation of the rates is much larger, which leads the gas temperature profile to peak at a length closer to the inlet than the reported profile from [Chen et al.](#).
- ◇ It can be said that the CFD implementation of the GKM is not equally reliable for a non-isothermal methanol synthesis reactor.

## C.2 Natural circulation methanol synthesis reactor

### C.2.1 Simulation of SMBR as a batch process reactor

#### Geometry and Mesh

Using the same mesh presented in Fig. 4.5

#### Boundary conditions

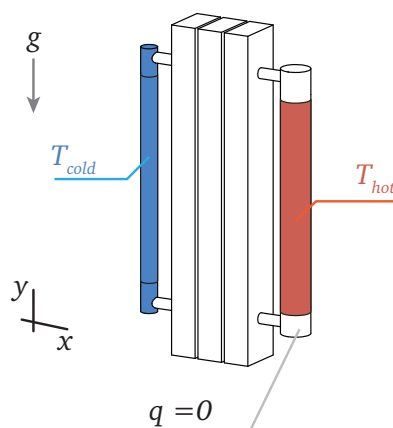


Fig. C.10. Diagram of boundary conditions applied to SMBR CFD simulations with the Bussche and Froment GKM.

- ◇ Fluid starting with a composition equal to feed mixture at 50 bar.
- ◇ Transient simulation ran for 116 seconds ( $t_{\text{simulation}} = 116$ )  
Timestep of 0.01 seconds.
- ◇ Temperatures boundary conditions.  
 $T_{\text{hot}} = 503$   
 $T_{\text{cold}} = 323$  K
- ◇ Influence of catalyst on momentum equation (Eq. 2.43) through viscous and inertial resistance matrices following Eqs. 2.49, 2.50.  
Particle diameter  $D_p = 0.005$  m  
Void fraction  $\varepsilon$  of 0.5.
- ◇ Packed bed in thermal equilibrium.

Tab. C.3. Values set for different void fraction values for a particle diameter of 5 mm. Using Eqs. 2.49 and 2.50.

$\varepsilon$	$D_{ii}$ [m <sup>-2</sup> ]	$C_{ii}$ [m <sup>-1</sup> ]
0.5	1.2E7	2.8E3

#### Results

The specific values for the equivalent length are determined from the information reported in Fig. C.11 are calculated in the following equations:

$$\begin{aligned}
 m_{\text{gas}} &= 1.02 \text{ gr} \\
 L_{\text{packed bed}} &= 0.130 \text{ m} \\
 L_{\text{loop}} &= 0.130 \text{ m} \\
 W_{\text{avg}} &= 1.178\text{E-}4 \text{ kg/s} \\
 \tau_{\text{loop}} &= \frac{m_{\text{gas}}}{W_{\text{avg}}} = 8.66 \text{ s}
 \end{aligned}$$

The equivalent length of the plug flow reactor is obtained from Eq. C.1

$$L_{\text{eq}} = L_{\text{packed bed}} \frac{t_{\text{simulation}}}{L_{\text{loop}}} = 1.74 \text{ m} \quad (\text{C.1})$$

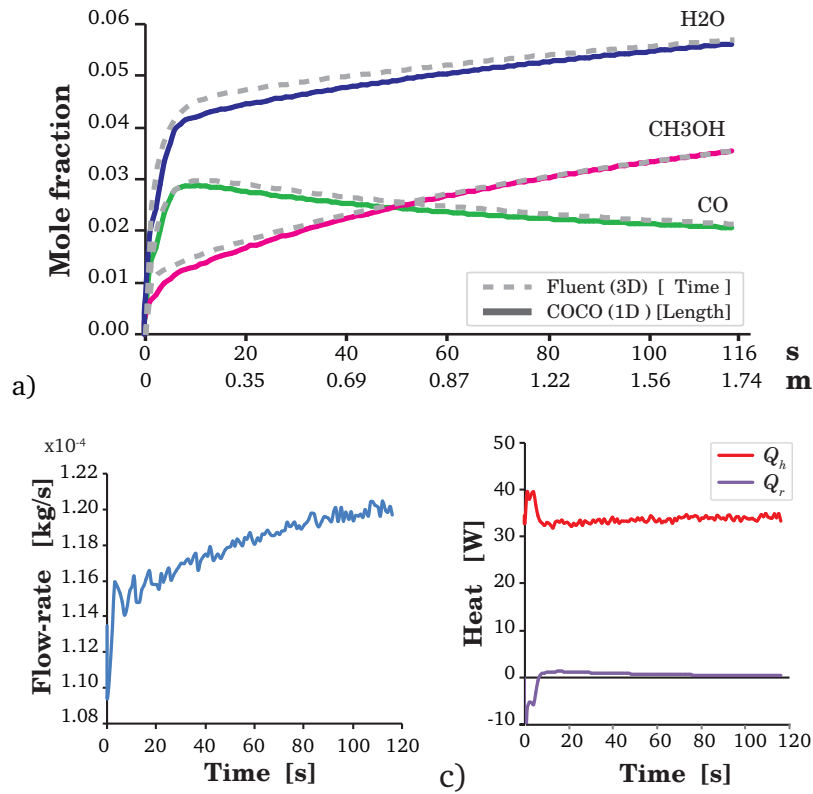


**Fig. C.11.** Comparing transient SMBR CFD reaction simulation with 1D PFR model for average mass flow and equivalent length. a) Profiles of species concentration. b) Flow-rate over time. a) Heat sources in the reactor: Input heat  $Q_h$  and heat of reaction  $Q_r$ .

**Tab. C.4.** Comparing methanol synthesis reactor. 1D plug flow reactor vs 3D NCL reactor.

	COCO™ (1D) at 1.74 m	Fluent™ (3D) at 116 s	Unit
H <sub>2</sub> O	0.0588	0.0562	mol/mol
CH <sub>3</sub> OH	0.0385	0.0355	mol/mol
CO	0.0202	0.0207	mol/mol

To find the time the natural circulation reactor would take to reach equilibrium, the length of the 1D PFR model was increased until reaching equilibrium (composition presented in Tab. C.5).

Considering the average flow-rate, an equilibrium composition would be reached at a length of 44 m. For the SMBR it would be equivalent to 48.7 minutes. For the current simulation settings, that's a 12 day calculation.

Tab. C.5. Equilibrium composition from a feed gas composition of H<sub>2</sub>/CO<sub>2</sub> at a

	Value	Unit
T	503	K
P	50	bar
H <sub>2</sub>	0.63615	mol/mol
CO <sub>2</sub>	0.20272	mol/mol
CO	0.01398	mol/mol
H <sub>2</sub> O	0.08056	mol/mol
CH <sub>3</sub> OH	0.06657	mol/mol

Considering the change of methanol concentration in the SMBR over time, the specific energy demand will increase, as it is reported in Fig. C.12.

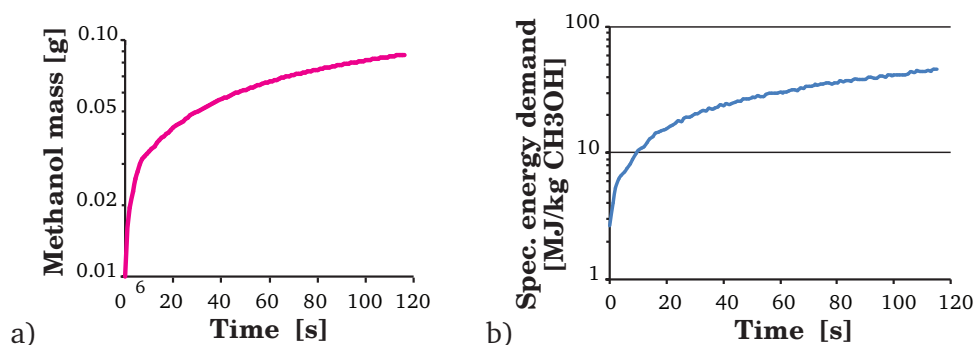


Fig. C.12. Semi-log plots of methanol production in reactor. a) Mass of methanol inside the SMBR fluid volume over time. b) Specific energy required to produce methanol over time.

Specific energy demand is calculated from the reported data of energy input  $Q_h$  and the mass fraction of methanol  $\omega_{\text{CH}_3\text{OH}}$  following Eq. C.2 in units of MJ/kg of methanol.

$$\text{Specific energy} = \frac{1\text{E-}6(Q_h t)}{m_{\text{gas}} \omega_{\text{CH}_3\text{OH}}} \quad (\text{C.2})$$

Where:

$Q_h$  is the thermal energy input at the hot side in unit of W.

$t$  is the timestep in unit of s.

$m_{\text{gas}}$  is the mass of gas inside of the SMBR in unit of g.

$\omega_{\text{CH}_3\text{OH}}$  is the mass fraction of methanol in the SMBR.

### Observations

- ◇ From Fig. C.11a and the values of Tab. C.4, it can be seen that approach taken to compare composition over time is in close accordance between the 3D CFD reaction model and the 1D isothermal plug flow reactor model with average flow-rate. Deviations near the inlet can be attributed to a rapidly changing mass flow that occurs in the transient simulation.
- ◇ From Fig. C.11b, flow-rate is observed to increase over time. This is attributed to the increase in density of the fluid.

- ◇ From Fig. C.11c, a negative spike can be observed in the energy of reaction  $Q_r$  during the initial 2 seconds of the simulation time. This is attributed to the reverse water gas-shift (Eq. 2.2) which is endothermic ( $Q_r$  is negative). This reaction rapidly creates CO. As CO concentration peaks, the exothermic CO<sub>2</sub> hydrogenation reaction (Eq. 2.1) takes over and releases energy into the flow ( $Q_r$  is positive).
- ◇ The rate of methanol production over time observable in Fig. C.12 shows that the natural circulation reactor as **a batch process it becomes less energy efficient** the longer it runs. This is because the gas composition is not being separated or refreshed. The maximum concentration of methanol achievable would be the equilibrium composition presented in Tab. C.5.



## Appendix D

# Steady state nitrogen flow-rate for MBR with heat recovery

This was a flow experiment performed on the MBR with Nitrogen at 50 bar [3].

### Geometry and Mesh

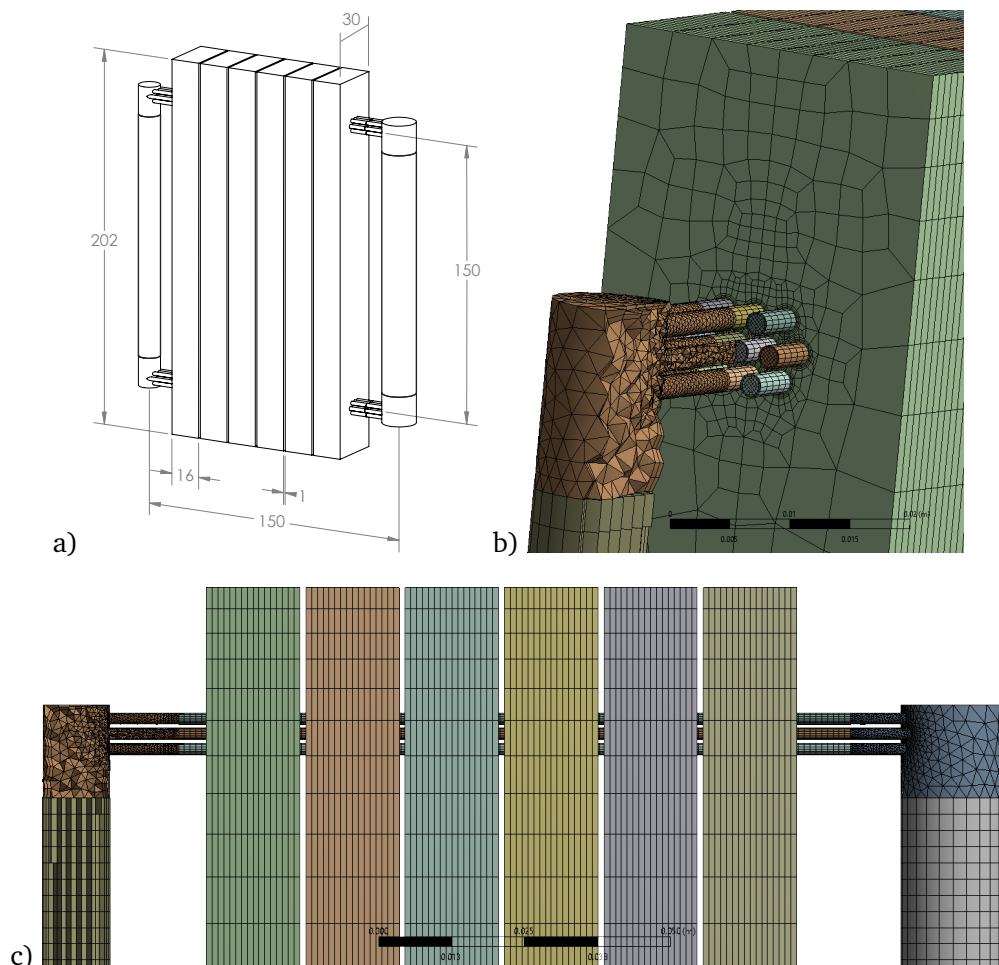
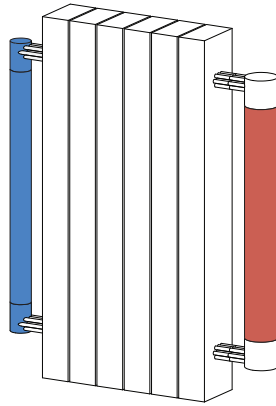


**Fig. D.1.** Geometry of the fluid and mesh. 503k cell mesh. Average cell orthogonality: 0.9324, Average cell skewness: 0.17069.



---

## Boundary conditions



- ◇ Temperature boundary conditions:
  - $T_{cold}$ : 315 K
  - $T_{cold}$ : 480 K
- ◇ Solid domain: Aluminium.
- ◇ Fluid domain: Nitrogen at 50 bar.  
Basic FP, see Sec. A.1.

Fig. D.2. Boundary conditions for simulation

## Results

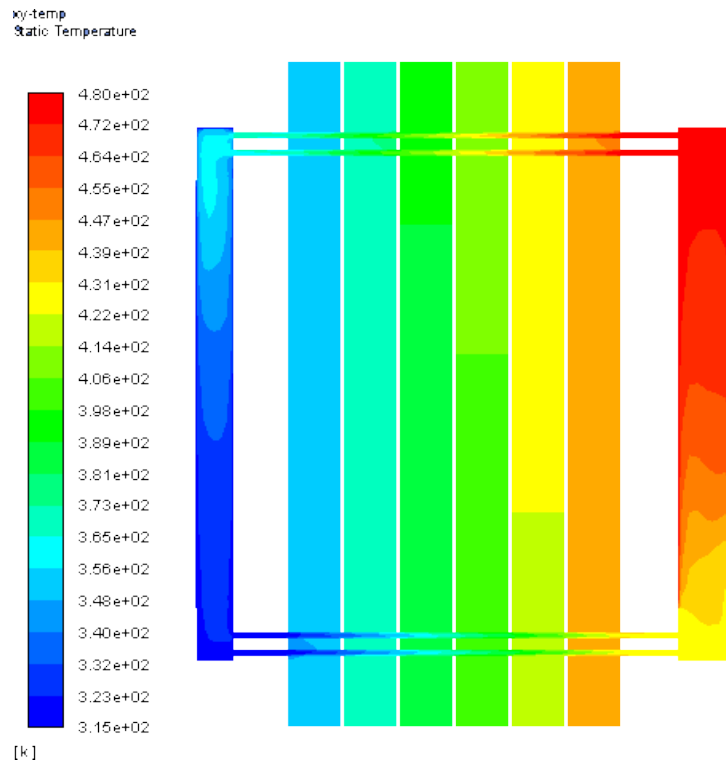


Fig. D.3. Temperature contours of simulation

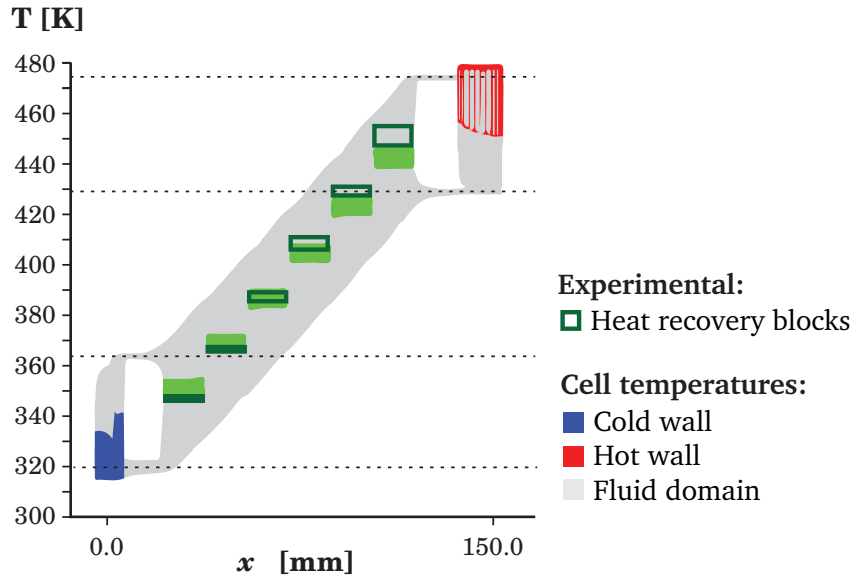


Fig. D.4. T-x plot for simulation with nitrogen at 50 bar. Experimental measurements of temperatures overlaped

Tab. D.1. Comparing results

Report	3D CFD	Experimental	Unit
$Q_h$	10.66	51.78	W
$Q_{blocks}$	26.07	45.96	W
$W_{ss}$	2.090E-4	4.12E-4	kg/s

**Observations**

- ◇ Heat losses have been rated to 40 - 35 W based on the insulation.
- ◇ Flowrate is smaller than what's estimated from experimental measurements. But still same order of magnitude.
- ◇ An error in calculating the recovered heat  $Q_{blocks}$  will influence the estimation of flowrate.
- ◇ The slope of the temperature on the blocks is higher than with simulations. This can be attributed to axial heat transfer between each block. It has been stated in Fig. 4.10